2019

Electron Collisions with Atoms and Molecules

Jeffery Michael Dech
University of Windsor

Electron Collisions with Atoms and Molecules

By

Jeffery Michael Dech

A Dissertation
Submitted to the Faculty of Graduate Studies
through the Department of Physics
in Partial Fulfillment of the Requirements for
the Degree of Doctor of Philosophy at the
University of Windsor

Windsor, Ontario, Canada

Electron Collisions with Atoms and Molecules

by

Jeffery Michael Dech

APPROVED BY:

W. van Wijngaarden, External Examiner
York University

R. Schurko
Department of Chemistry and Biochemistry

S. J. Rehse
Department of Physics

W. Kedzierski
Department of Physics

J. W. McConkey, Advisor
Department of Physics

April 22, 2019

Declaration of Previous Publication

Co-Authorship

I hereby declare that this thesis incorporates material that is the result of joint research, as follows: Chapter 7 of the thesis was co-authored with W. Kedzierski and J. W. McConkey. In all cases, the key ideas, primary contributions, experimental designs, data analysis, interpretation, and writing were performed by the author. The contribution of the co-authors was primarily through W. Kedzierski contributing to the graphing of results.

I am aware of the University of Windsor Senate Policy on Authorship and I certify that I have properly acknowledged the contribution of other researchers to my thesis, and have obtained written permission from the co-author to include the above material in my thesis.

Previous Publication

This thesis includes an original paper that has been previously published/submitted for publication in a peer reviewed journal, as follows:

Thesis Chapter	Publication title/full citation	Publication status
Chapter 7	W Kedzierski, J Dech, and JW McConkey. "N(^{2}P) production in electron-N_2 collisions". *Journal of Physics B: Atomic, Molecular and Optical Physics* 50.21 (2017)	Published

I certify that I have obtained a written permission from the copyright owner(s) to include the above published material(s) in my thesis. I certify that the above material describes work completed during my registration as a graduate student at the University of Windsor.

I declare that, to the best of my knowledge, my thesis does not infringe upon anyone's copyright nor violate any proprietary rights and that any ideas, techniques, quotations, or any other material from the work of other people included in my thesis, published or otherwise, are fully acknowledged in accordance with the standard referencing practices. Furthermore, to the extent that I have included copyrighted material that surpasses the

bounds of fair dealing within the meaning of the Canada Copyright Act, I certify that I have obtained a written permission from the copyright owner(s) to include such material(s) in my thesis.

I declare that this is a true copy of my thesis, including any final revisions, as approved by my thesis committee and the Graduate Studies office, and that this thesis has not been submitted for a higher degree to any other University or Institution.

Abstract

Measurements of the production of atomic and molecular metastable states are performed using a novel frozen solid layer detector. This includes examination of solid CO_2 and N_2O layers in metastable detection, measurements of $N(^2P)$ production from dissociation of N_2, investigations into the suitability of solid neon layers for detection of $S(^1D)$ based on electron-impact dissociation studies of OCS and production of $O(^1S)$ and $CO(a^3\Pi)$ in electron-impact dissociation of methanol.

Novel solid layers for detection of metastable states were examined to determine which products they were sensitive to. First, CO_2 layers were deposited and were found to be sensitive to both $O(^1S)$ and $N_2(a^1\Pi_g)$ metastable states. The relative efficiency of these layers as a function of temperature and lifetime of the state formed from the impinging $O(^1S)$ atoms are reported. Mechanisms which may be responsible for the radiation through formation of CO_3 or its ion are also suggested. The detection of metastable $N_2(a^1\Pi_g)$ states from solid N_2O layers is also reported.

A study of $N(^2P)$ production after electron-impact dissociation of N_2 was also performed. It was determined that two excitation channels contribute to production of this state. Time-of-flight and fragment kinetic energy spectra are presented for 100 eV impact energy. Excitation function data is also provided over the 0 eV to 200 eV range for one of these channels. Dissociation processes are proposed for both production channels which appear to be due to both a direct dissociation and pre-dissociation mechanism. Intermediary states are proposed for both channels.

Investigations into the suitability of solid neon layers for the detection of $S(^1D)$ are performed through studies of electron-impact dissociation of OCS. It was found that while production of $S(^1D)$ is likely occurring, interactions with solid neon layers do not result in emission within the optical spectral range of our photo-multiplier tube. However, an ultraviolet emission from these layers was detected in these experiments. While the nature of this feature was not definitively identified, some possible processes which may be responsible are discussed. Future investigations to determine the source of the emission are proposed. In addition, likely production channels of $S(^1D)$ are suggested.

Electron-impact dissociation of methanol was also performed. It was observed that both $CO(a^3\Pi)$ and $O(^1S)$ metastable states are produced and detected with solid xenon layers. While production of $CO(a^3\Pi)$ has been reported previously, this appears to be the

first observation of $O(^1S)$ production from electron-impact of methanol. Time-of-flight and released kinetic energy spectra are presented for both features at 100 eV impact energy. Excitation functions are also presented for 10 eV to 90 eV impact energy for both states. The production of $CO(a^3\Pi)$ coincides with the observations of previous studies and the measurement of the excitation cross section is extended from an energy of 21 eV to 90 eV. No new dissociation channels for this state were found. Meanwhile, production of $O(^1S)$ appears to occur through a direct dissociation mechanism causing breakage of the CO bond and formation of $OH(B^2\Sigma^-)$ which subsequently dissociates into $O(^1S)$ and $H(^2S)$.

To my parents for their support throughout my career,
to the Kagans for pushing me to achieve my best,
and to Neda Mashhadi for giving me strength to run the race to the end.

Acknowledgments

I would like to thank Dr. J. W. McConkey for the joy and privilege of working under him for this graduate dissertation. He has been foremost a friend and an adopted grandfather for me during my time as a graduate student. The many long talks about physics and life in general have been times that I will cherish for the rest of my life. The sage wisdom and advice that he has provided will follow me long after I am done this brief time in the lab and I am lucky to be able to account his as both a mentor and a friend.

I am also grateful for the sage advice of Dr. W. Kedzierski. His experience and ingenuity has been woefully unrecognised as without him, very little experimentation would have been conducted. I will always keep in mind his out of the box problem solving skills which have been invaluable throughout my time in this lab. I can truly say that he is a character among physicists who's expertise has been underappreciated. I am truly grateful for the excellent and candid discussion we have had.

I would like to thank the many undergraduate students who have worked in our lab during this work. First and foremost, Joshua Trocchi who has always served with humility and a willingness to learn and do his best. His work and effort should be lauded. I would also like to thank Micheal Kouvalis, who rose to the bar and did all that was asked of him and more. Justine Cunningham also deserves recognition for serving as an exemplary study and exceeded expectations throughout her time in the lab.

Finally, I would like to thank our funding agencies for the privilege of working under their sponsorship. This includes the Natural Sciences and Engineering Research Council (NSERC) and the Canadian Foundation for Innovation (CFI). This work would not have been possible without their help.

Contents

List of Tables

List of Figures

List of Abbreviations

Abbreviation	Definition
CASSCF	Complete active space self-consistent field
CE	Collimation electrode
CF	Cold finger
CT	Capillary tube
CODATA	Committee on Data for Science and Technology
CRC	Chemical Rubber Company
DAQ	Data acquisition
DEA	Dissociative electron attachment
EE	Extraction electrode
EELS	Electron energy-loss spectroscopy
EG	Electron gun
FC	Faraday cup
FWHM	Full width at half maximum
HREELS	High resolution electron energy-loss spectroscopy
IC	Inner Farady cup
MCS	Multi-channel scaler
MR	Magnetic rod
NV	Needle valve
OC	Outer Faraday cup
PMT	Photo-multiplier tube
RG	Rare gas
SR	Support rod
TOF	Time-of-flight
TP	Turbo-molecular pump
TTL	Transistor-transistor logic

Chapter 1

Introduction

Metastable atoms, those which decay through magnetic dipole and electric quadrupole rather than electric dipole radiation, play an important role in numerous electron scattering phenomena. While they are critical in understanding our planet's atmospheric chemistry[1–3] and various terrestrial[4, 5] and extra-terrestrial[6–8] phenomena, they also appear in such diverse fields as plasma processing[9] and biological systems[10, 11]. Due to the varied and ever increasing number of ways they appear, it is important to continue to improve our understanding of the processes causing metastable production and to increase our knowledge of the number of places in which they appear.

Metastable atomic oxygen is one of the most widely studied metastable species. They play an important role in Earth's atmosphere where they can be seen in the Aurora Borealis as green O(^{1}S$\rightarrow^1$D) and red O(^{1}D$\rightarrow^3$P) features, are involved in the chemistry of the ozone layer[4, 5], and are an important part of other atmospheric processes[2, 3]. These two emission lines can also be seen in airglows occurring in extra-terrestrial atmospheres such as Venus and Mars[6, 8], and have also been found[7] to play an important part in our understanding of cometary systems.

Metastable oxygen also has an important role in a variety of biological systems. It has been shown[10] to modulate biochemical processes and may accelerate nerve tissue regeneration. Studies have also found[12–14] it could be of interest in developing plasma based medical treatment and has also been shown to have applications to the treatment of organic wastes[15].

Other metastable species are also important to our understanding of chemical and biological processes. For example the production CO($a^3\Pi$) has been shown to occur during electron collisions with prototypical biomolecules[11] and radiation from the Cameron bands ($a^3\Pi \rightarrow X^1\Sigma^+$) has been observed[16, 17] in the airglow of the Martian atmosphere.

The laboratory detection of metastable states is a rather difficult problem given their extremely long lifetimes. For example, the lifetime of O(^{1}S) is approximately 0.8 s[18]. In a standard photon detection experiment, atoms in these metastable states would need to travel hundreds of meters before decaying and are therefore almost impossible to reliably

detect in standard collision chambers before the atoms are quenched by collisional losses with background gases or the walls of the chamber. As such, special techniques are required for in depth investigations of metastable state production.

1.1 Detection of Metastable States

Several methods for single particle detection of metastable states have been investigated for $O(^1S)$. For example, Auger emission from low work function surfaces[19–21] or gas phase chemi-ionization surfaces[22] have been employed to directly observe these states. Indirect studies have also been performed using electron energy-loss spectroscopy (EELS)[11]. However, these methods were unable to clearly separate signals from $O(^1S)$ and other metastable species such as $O(^5S)$ or suffered from poor signal-to-noise ratios.

Optical techniques have also been implemented to measure photoemission of these species following quenching of the metastable state. One of the earliest studies of this type was by McLennan and Shrum[23], who used a helium buffer gas to prevent collisional losses to the walls of their discharge tube. Other spectroscopic methods included the formation of kryton and xenon excimers, excited bound molecules with dissociative ground states, in high pressure chambers to induce collisional quenching of $O(^1S)$[24–29]. The issue with such methods is that information is lost regarding the cross sections for formation or their released kinetic energy imparted during dissociation from their parent molecules. As such, their utility is limited to observing the existence of these metastable states.

A viable route to a more informative detection method came with the advent of Matrix Isolation Spectroscopy. While now commonly used as a method to study free radicals and other unstable or transient chemical species[30], the origins of this technique actually begin with observations of $O(^1S)$ oxygen. In 1948, Veygard and Kvifte[31] made the realization that green emissions from layers of solid molecular nitrogen/argon mixtures were due to the presence of a small oxygen impurity which was radiating at the $O(^1S \rightarrow {}^1D)$ transition wavelength. Similar radiation lines were later observed by Schoen and Broida[32] in experiments freezing rare gas-oxygen mixtures on a surface at 4 K and then bombarding them with 5 keV electrons. These early developments led to several other groups investigating this transition in solid rare gases theoretically[33] and experimentally using either electronic[34, 35] or photonic[36–44] excitation mechanisms.

The lifetime of $O(^1S)$ after forming a rare gas excimer has also been measured directly. Goodman *et al.*[36] were able to determine the lifetime of $XeO(2^1\Sigma^+)$ embedded in argon and neon matrices held at 22 K to be 114 ns. When compared to the free $O(^1S)$ state lifetime of approximately 0.8 s, this corresponds to a change of almost seven orders of magnitude. Lifetimes of other rare gas $O(^1S)$ excimers have also been measured[45] to be 0.2 µs for NeO^*, 4.2 µs for KrO^* and 23.4 µs for ArO^*.

Kiefl *et al.*[46] were the first to build on these studies to develop a single particle detection

system for selective measurement of $O(^1S)$ using the radiation from an XeO^* excimer. First producing $O(^1S)$ from dissociation of O_2 in a crossed-beam study using a pulsed electron source, they were able to resolve the metastable atoms in their dissociated beam using a time-of-flight method. Their detector was a solid xenon layer condensed on a surface at 70 K. While they reported extinction ratios of $O(^1S)$ by various gases, they did not obtain direct excitation cross sections in their investigations.

Another issue with this study was that the photon detection system was optimized for measurements of radiation in the green region between 500 and 600 nm. As will be explained shortly, this is not the ideal spectral range in which to measure the radiation from XeO^* and so their system suffered from less than ideal signal to noise ratios. However, their kinetic energy data for $O(^1S)$ dissociated from O_2 was able to be verified by LeClair and McConkey[47] in later experiments.

All of these developments led to the construction of the detection system used in this work. An initial prototype was constructed by Corr and outlined in his thesis[48] which used a layer of xenon frozen on a cold-finger held near 74 K in order to try to detect $O(^1S)$ through an excimer formation process. However, this apparatus suffered from two experimental deficiencies which prevented their objective from being achieved. First, a tungsten cathode was used in the electron gun which only lasted a few hours when exposed to the O_2 target beam. Additionally, the photo-multiplier tubes and filters used to detect the radiating excimers formed on the surface were again optimized to observe green light. However, these experiments were able to effectively detect metastable $O^+(^2D, ^2P)$ following dissociative ionization of O_2[49], demonstrating that the overall method could be modified for the measurement of $O(^1S)$.

While the studies of Kiefl *et al.* and Corr *et al.* measured excimer emissions in the green, the dominant XeO^* excimer emission is actually in the near infrared. This was first noticed by Lawrence and Apkarian[44] in their experiments with UV photolysis of $Xe:N_2O$ mixtures. When observing the spectrum of XeO^* emissions, they were able to observe two main features at 375 nm and 725 nm, with the dominant emission being in the near infrared.

Their explanation for these spectral features is based on consideration of the XeO system's potential energy diagram, shown in Figure 1.1. It was suggested that in their experiment, the $O(^1S)$ dissociating from N_2O would embed itself at interstitial sites of octahedral symmetry within the xenon matrix. Once embedded, the atoms were excited to the ionic $Xe^-O^+(3^1\Sigma^+)$ state about 5 eV above the Xe + $O(^3P)$ ground state. Once the state relaxed to the potential minimum around 4 eV, it would then radiate. As this ionic state lies below the potential energy curve of the covalent $XeO(2^1\Sigma^+)$ state, an avoided crossing occurs which permits a bound state in the solid phase[44] which would otherwise be dissociative in the gas phase. If a transition occurred to the inner repulsive wall of the $XeO(^1\Pi)$ curve, the observed infrared emission would occur while a transition to the minimum of the $XeO(1^1\Sigma^+)$ state resulted in the ultraviolet emission at 375 nm. An analagous situation

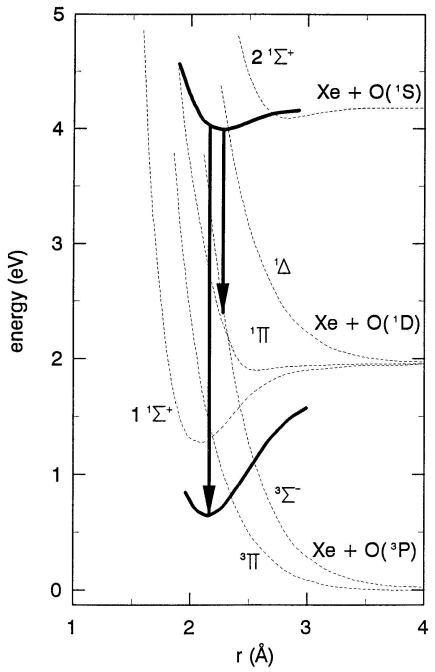

Figure 1.1: Molecular potential curves for the XeO system. The dashed lines represent curves taken from Dunning and Hey[50] and Simmons *et al.*[29] while the solid lines are from Lawrence and Apkarian[44]. The diagram is reproduced from McConkey and Kedzierski[51].

likely occurred in the experiments of Kiefl *et al.* and Corr *et al.* when free $O(^1S)$ atoms impinged on the solid xenon surface, suggesting that the greater signal strengths would have been observed if they had looked in the infrared rather than the green.

Based on the findings of Lawrence and Apkarian and some of the lessons learned in the early experiments by Corr *et al.*, the system was redesigned into the form used by LeClair *et al.*[47] and in the present work. First, the tungsten cathode was replaced with thoriated iridium, which greatly extended the life of the electron gun. Second, photon detection was optimized for the infrared rather than the green. LeClair *et al.*[47, 52] were then able to use this improved detection system to measure the excitation cross section for $O(^1S)$ from N_2O and O_2, paving the way for a series of experiments measuring $O(^1S)$ production.

During these initial experiments, LeClair *et al.* confirmed the presence of the ultraviolet and infrared features from the xenon layer. A small green feature was also observed, coinciding with the observations of Kiefl *et al.* and Corr *et al.*. The feature was reported to be weaker than the infrared emission by about a factor of twenty and was attributed to gas phase collisional quenching of $O(^1S)$ by xenon near their detector surface. This explains the difficulties encountered in previous experiments.

Since then, the system has been used to perform measurements of $O(^1S)$ production in O_2[47], N_2O[47, 53], H_2O and D_2O[54, 55], CO_2[56], CO[57], NO[58] and SO_2[59]. Solid xenon layers have also been shown to be sensitive to other metastable atoms such as $S(^1S)$,

measuring its production in OCS[60]. Metastable molecular states have also been studied with measurements of CO($a^3\Pi$) production from CO_2[56] and CO[57] also being reported.

Investigations into the suitability of other solid rare gas layers have also been performed[45] showing that solid neon, argon, and krypton are also sensitive to O(^{1}S) and presumably S(^{1}S), which is isoelectronic with O(^{1}S), as well. Furthermore, it was discovered that Neon layers also form excimer states with O(^{1}D) which radiate in the red, permitting measurements of its production from N_2O[61] and CO_2[61, 62]. Solid N_2 layers have also been shown[63, 64] to be sensitive to metastable singlet gerade states of N_2 as well.

1.2 Present Work

The present work continues this campaign of determining methods of detecting metastables and reporting their excitation cross sections from different targets. This is extended on multiple fronts. First, investigating the suitability of various solid layers for the detection of metastable atoms and molecules. Second, measuring O(^{1}S) production in new systems where cross section data may be lacking. Finally, investigating the possibility of measuring new metastable species using the available techniques in order to extend the method to new targets. The scientific motivations for these various studies are outlined in detail at the beginning of each chapter.

The opening part of this dissertation lays the ground work for the experimental studies reported in the later chapters. Chapters 2 through 4 describe the theoretical basis for these studies. This includes atomic structure and spectra in Chapter 2. As metastable atoms radiate through magnetic dipole and electric quadrupole radiation, a description of both electric dipole radiation and its associated selection rules as well as that of these higher order terms is given. Chapter 3 covers molecular structure and outlines some of the classification conventions which are important for assigning molecular term symbols. This is important for understanding the molecular states involved in dissociative collisions. In addition, selection rules are present for electric dipole, magnetic dipole, and electric quadrupole transitions; the latter two being important when considering metastable molecular states. In Chapter 4, as electron-impact collisions are the main focus of this work, electron-atom and electron-molecule scattering is considered first with a discussion of the various types of electron scattering phenomenon and then an outline of the Bethe-Born theory for fast electron collisions, describing the functional forms for different kinds of inelastic scattering.

A description of the experimental apparatus is given in Chapter 5. This includes all of the experimental equipment used for both the production and detection of metastable species. In addition, this chapter describes the detector's operation in more detail and explains the excimer formation process which is the basis for the present method of observing metastable species.

An investigation into novel detection layers is undertaken in Chapter 6 in order to attempt to broaden the method for use with new metastable species. Results from new solid layers, in particular CO_2 and N_2O, are presented, which have been found to be sensitive to several metastable species. The chapter closes with a summary of all of the work undertaken with various solid layers so far, indicating which layers are of practical use in detecting specific metastable species and providing references to the relevant literature.

The detection of new metastable species is reported in Chapters 7 and 8. Measurements of $N(^2P)$ production from N_2 is discussed in Chapter 7 where a solid xenon layer was used to detect the $N(^2P)$ state for the first time using a single particle detection system. Investigations into the possibility of observing $S(^1D)$ from OCS using frozen Neon layers are also reported in Chapter 8.

Studies of metastable production in electron-impact dissociation of methanol are then reported in Chapter 9. Here, $O(^1S)$ and $CO(a^3\Pi)$ production were both observed in this molecule using solid xenon surfaces. Cross sectional data and possible excitation routes are presented.

Chapter 2

Atomic Structure

Atomic structure is determined by the configuration and motion of electrons about a nucleus. The quantized energy levels within the atom, found from this structure, dictate the allowed channels for absorption and emission of electromagnetic radiation. The spherical symmetry of the atomic nucleus' Coulomb potential implies that this structure can be determined by independently examining the radial positions and angular momentum of the individual electrons to develop a cohesive calculation of the overall atomic structure. These calculations can then be used to determine the optical absorption and emission characteristics of individual atomic systems. This information can then be used to determine the spectroscopic properties of atomic systems which is of critical utility in this work.

States of an N electron atom are found[65] by solving the time-independent Schrödinger equation

$$H\left|\psi\right\rangle = E\left|\psi\right\rangle \tag{2.1}$$

which determines the energy E of the state subject to[66] the atomic Hamiltonian

$$H = -\sum_{i=1}^{N}\frac{\hbar^2}{2m_e}\nabla_i^2 - \sum_{i=1}^{N}\frac{Ze^2}{|\mathbf{r}_i|} + \sum_{i=1}^{N}\sum_{j>i}^{N}\frac{e^2}{|\mathbf{r}_j - \mathbf{r}_i|} \tag{2.2}$$

in terms of the radial positions $\mathbf{r}_i$ and $\mathbf{r}_j$ of the electrons and the nuclear charge Z. This Hamiltonian includes three terms relating to the kinetic energy, nuclear Coulomb field and electron-electron interactions. More accurate structure calculations can be conducted[66], if necessary, by including additional effects such as spin-orbit interactions or other finer structural considerations.

While the total wave function is the relevant descriptive object for determining atomic structure, it is typically built from wave functions for each of the individual electrons orbiting the nucleus, forming the total wave function as a product of these individual terms. One could naively attempt to form the total state as a product of N single electron wave functions; however, the fact that electrons are Fermions introduces an additional constraint, namely the probability density of the total wave function Ψ which is given by the quan-

tity $|\langle\Psi|\Psi\rangle|^2$ must be invariant under permutation symmetry to satisfy the Pauli exclusion principle[65]. In other words, it must be invariant under the exchange of positions of any two electrons. To form such a fully anti-symmetric wave function, one must form the total wave function from the *Slater determinant*[66] of the N individual electronic functions

$$\Psi(\mathbf{r}_1,\ldots,\mathbf{r}_N) = \frac{1}{\sqrt{N!}}\begin{vmatrix} \psi_1(\mathbf{r}_1) & \psi_1(\mathbf{r}_2) & \psi_1(\mathbf{r}_3) & \ldots \\ \psi_2(\mathbf{r}_1) & \psi_2(\mathbf{r}_2) & \psi_2(\mathbf{r}_3) & \ldots \\ \psi_3(\mathbf{r}_1) & \psi_3(\mathbf{r}_2) & \psi_3(\mathbf{r}_3) & \ldots \\ . & . & . & \\ . & . & . & \end{vmatrix} \tag{2.3}$$

To determine the single electron wave functions, one typically considers the problem in spherical symmetry with separable wave functions of the form

$$\psi_i(\mathbf{r}) = \frac{1}{r}P_{n_i\ell_i}(r)Y_{\ell_i}^{m_i}(\theta,\phi)\cdot\sigma_{m_{s_i}}(s_z) \tag{2.4}$$

which account for the radial, $P_{n\ell}(r)$, angular, $Y_\ell^m(\theta,\phi)$ and spin, $\sigma(s_z)$, components of the wave function.

While the angular component can easily be solved analytically (Section 2.1), solving the radial component of the wave function $P_{n\ell}(r)$ for multi-electron atoms usually involves computational methods. Procedures such as the Hartree-Fock method[66] are typically used to determine self-consistent fields which account for the many-body interactions which are present in these N electron systems. While interesting in their own right, this work does not calculate any wave functions, but relies of the numerous calculations which are available for the atoms in molecules of interest. As such, the topic of determining the radial wave functions will not be discussed further as it is beyond the scope of this work.

2.1 Angular Momentum

In addition to the radial motion, atomic angular momentum is also quantized. There are multiple sources for this including the orbital angular momentum of the electrons moving about the nucleus, the intrinsic electron spin, and nuclear spin. Together, these will couple to form an overall angular momentum which must be considered when examining atomic structure. Understanding the properties of angular momentum and the ways in which the various sources can couple is important when classifying the various atomic states which can appear in experimental work.

Measurements of the individual components of the angular momentum do not commute[65]. If one considers some arbitrary angular momentum $\mathbf{J}$, one will determine states which are simultaneous eigenvalues of the observables $\mathbf{J}^2$ and a single momentum component, often J_z by convention. These states $|J,m\rangle$ take on values $J = 0,1,2,\ldots$ and

$m = -J, -J+1, \ldots, J-1, J$ with eigenvalues

$$\mathbf{J}^2 \left|J, m\right\rangle = \hbar^2 J(J+1) \left|J, m\right\rangle \tag{2.5}$$

$$J_z \left|J, m\right\rangle = \hbar m \left|J, m\right\rangle \tag{2.6}$$

In the case of orbital angular momentum, denoted $\mathbf{L}$, the operators[66] have the form

$$\mathbf{L}^2 = -\hbar^2 \left[\frac{1}{\sin\theta}\frac{\partial}{\partial\theta}\left(\sin\theta\frac{\partial}{\partial\theta}\right) + \frac{1}{\sin^2\theta}\frac{\partial^2}{\partial\phi^2}\right] \tag{2.7}$$

$$L_z = -i\hbar\frac{\partial}{\partial\phi} \tag{2.8}$$

The wave functions which are simultaneous eigenfunctions of these two operators are the well known[65–67] spherical harmonics

$$Y_{\ell i}^m(\theta_i, \phi_i) = (-1)^{(m+|m|)/2}\left[\frac{(2\ell+1)(\ell-|m|)!}{4\pi(\ell+|m|)!}\right]^{1/2} P_\ell^{|m|}(\cos\theta_i)e^{im\phi_i} \tag{2.9}$$

which are in terms of the associated Legendre polynomials $P_\ell^{|m|}(\cos\theta_i)$. In the case of multi-electron atoms, the angular momenta of the individual electrons is often denoted $\boldsymbol{\ell}_i$ for the i^{th} electron. The second relevant source of momentum is the intrinsic spin of the electrons for which $S = 1/2$ and $m = -1/2, 1/2$. By a similar convention, for multi-electron atoms the individual spins can be denoted $\mathbf{s}_i$.

While the nuclear spin is also a source of angular momentum in atomic systems, this does not usually contribute to the gross structure of an atom due to the extremely low energy scale of these interactions. As the energy resolution of this work in insufficient to distinguish these hyperfine features, we will restrict the discussion to the aforementioned sources of angular momentum.

2.2 Angular Momentum Coupling

Coupling between the different angular momenta will also introduce additional terms to the atomic Hamiltonian, shifting the energy levels of the system. One example that can be significant is the spin-orbit interaction

$$H_{SO} = \sum_{i=1}^{N} \zeta(r_i)(\boldsymbol{\ell}_i \cdot \mathbf{s}_i) \tag{2.10}$$

where $\zeta(r_i)$ is a function which depends on the electron's radial position. Typically, the spin-orbit coupling is modelled[66] by the equation

$$\zeta(r) = \frac{\alpha^2}{2}\frac{1}{r}\frac{dV}{dr} \tag{2.11}$$

in terms of the electron's potential energy $V(r)$ but other forms of the coupling are possible in some atomic systems. Other angular momentum coupling terms may also add higher order corrections[67] to the Hamiltonian, but typically spin-orbit coupling is the dominant term.

The strength of the spin-orbit coupling can determine the ordering of atomic states and their classification schemes. Typically, in the lighter nuclei[66], the mutual repulsion between the electrons originating from the term

$$H_{rep} = \sum_{i=1}^{N} \sum_{j>i}^{N} \frac{2e^2}{|\mathbf{r}_j - \mathbf{r}_i|} \tag{2.12}$$

are stronger than the spin-orbit coupling energy. For these atoms, the interactions between the orbital angular momenta of the different electrons dominates the spin-orbit term. When this is true, one can consider the coupling of the individual orbital and spin angular momenta using the vectors

$$\mathbf{L} = \sum_{i=1}^{N} \boldsymbol{\ell}_i \qquad \mathbf{S} = \sum_{i=1}^{N} \mathbf{s}_i \tag{2.13}$$

and then form the total angular momentum vector as

$$\mathbf{J} = \mathbf{L} + \mathbf{S} \tag{2.14}$$

This coupling scheme is known as LS-coupling or Russell-Saunders coupling. In this regime, atomic states are denoted using Russell-Saunders notation where the term symbols have the form

$$^{2S+1}L_J \tag{2.15}$$

This is the main coupling scheme considered in this work. While other schemes such as JJ-coupling are possible[66], these are not important for this work and will not be discussed further.

2.3 Radiative Transitions

In this section, we discuss the types of optical transitions which may occur within an atom. Often, one limits the discussion of radiative transitions to optical dipole radiation, which is the predominant source of photonic transitions within atomic systems. However, when discussing metastable states, where the electric dipole transition moments are zero, there becomes a need to discuss higher order terms such as magnetic dipole and electric quadrupole radiation. All three types of emission are outlined below.

The radiative transition rate between two arbitrary states can be found from Fermi's

golden rule[65, 68] which, using first order perturbation theory, is found from the expression

$$w_{i\to f} = \frac{2\pi}{\hbar} |\langle f|V|i\rangle|^2 \tag{2.16}$$

and is dependent on the form of the transition elements $\langle f|V|i\rangle$ for the atomic potential in question. The most general form for an optical transition from an initial state $|i\rangle$ to a final state $|f\rangle$ is proportional[65, 66] to the matrix elements of the EM-field operator

$$\langle f|e^{i(\omega/c)(\hat{\mathbf{n}}\cdot\mathbf{x})}\hat{\boldsymbol{\varepsilon}}\cdot\mathbf{p}|i\rangle \tag{2.17}$$

The momentum operator term can be shown[65] to be equal to

$$\langle f|\hat{\boldsymbol{\varepsilon}}\cdot\mathbf{p}|i\rangle = im\omega\ \hat{\boldsymbol{\varepsilon}}\cdot\langle f|\mathbf{x}|i\rangle \tag{2.18}$$

Thus, for spontaneous emission, the transition rate can be found[68] to be

$$w = \frac{4}{3}\frac{e^2\nu^4}{c^3}|\ \langle f|e^{i(\omega/c)(\hat{\mathbf{n}}\cdot\mathbf{x})}\hat{\boldsymbol{\varepsilon}}\cdot\mathbf{x}|i\rangle\ |^2 \tag{2.19}$$

While this expression in theory describes radiative transitions completely, in practice, the EM-field operator's matrix elements are calculated by taking the Taylor series of the radiation field operator

$$e^{i(\omega/c)(\hat{\mathbf{n}}\cdot\mathbf{x})} = 1 + i\frac{\omega}{c}\hat{\mathbf{n}}\cdot\mathbf{x} + \ldots \tag{2.20}$$

The leading, zeroth-order term accounts for the electric dipole contribution to the radiation. While it is the dominant source of radiative decay, there are certain situations for which the dipole matrix elements are zero, termed "forbidden transitions", where higher order terms must be also be included. For such situations, it is usually sufficient to include the first-order term, which accounts for magnetic dipole and electric quadrupole radiation. The line strengths for all these types of radiative decay are discussed below.

2.3.1 Electric Dipole Transitions

The electric dipole transition strength can be found from the zeroth-order term of the Taylor expansion. This yields[66] a decay rate

$$w_{E1} = \frac{4e^2\omega^4}{3c^3h\nu} |\langle f|\mathbf{r}|i\rangle|^2 \tag{2.21}$$

If the the i^{th} position vector is written in units of Bohr radii, it can be expressed as the rank one tensor

$$|r_i|^2 = a_o^2 \sum_q |r_q^{(1)}(i)|^2 \tag{2.22}$$

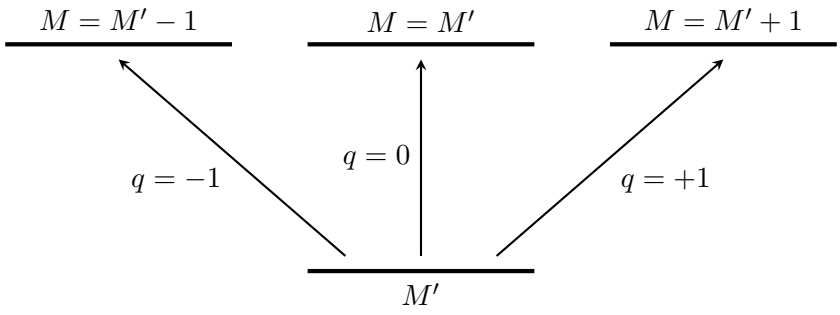

Figure 2.1: Mapping of electric dipole tensor components to the polarization of the absorbed photon. $q = \pm 1$ correspond to circularly polarized $\sigma_\pm$ changing the angular momentum M sub-level by a single quantum. $q = 0$ corresponds to linearly polarized π photons which keep the sub-level quantum number constant.

and in terms of the classical dipole strength

$$P_q^{(1)} = \sum_{i=1}^{N} r_q^{(1)}(i) = \sum_{i=1}^{N} r_i C_q^{(1)}(i) \tag{2.23}$$

making use of the normalized spherical harmonic basis

$$C_q^{(k)} = \sqrt{\frac{4\pi}{2k+1}}\, Y_q^k(\theta, \phi) \tag{2.24}$$

One can apply the Wigner-Eckart theorem (Equation C.1) to states with angular momentum J denoted $|\gamma JM\rangle$ to determine the transition strengths in terms[66] of $3j$-symbols and reduced matrix elements.

$$\langle \gamma JM | P_q^{(1)} | \gamma' J' M' \rangle = (-1)^{J-M} \begin{pmatrix} J & 1 & J' \\ -M & q & M' \end{pmatrix} \langle \gamma J \| P^{(1)} \| \gamma' J \rangle \tag{2.25}$$

The dipole line strength can then be written in terms of the reduced matrix elements as

$$w_{E1} = \frac{4\omega^3}{3\hbar c^3} \left| \langle \gamma J \| P^{(1)} \| \gamma' J \rangle \right|^2 \sum_q \begin{pmatrix} J & 1 & J' \\ -M & q & M' \end{pmatrix}^2 \tag{2.26}$$

In the spherical tensor basis there exists a correspondence between the polarization of the radiation and the tensor index q. Circularly polarized light is observed for the $q = \pm 1$ transitions while linearly polarized light is emitted for $q = 0$. This polarization mapping is summarized in Figure 2.1.

The $3j$-symbols are non-zero only when certain conditions are satisfied, and therefore, optical transitions between given initial and final states may only occur when these criteria are fulfilled. As such, they furnish a set of *selection rules* on optical transitions. Specifically,

the total angular momentum may not change by more than a single quantum

$$\Delta J = J - J' = 0, \pm 1 \tag{2.27}$$

which is further restricted by the condition

$$J = J' = 0 \quad \text{is forbidden} \tag{2.28}$$

Further selection rules are imposed in the LS-coupling regime. As the electric dipole operator is independent of spin co-ordinates in this regime, the matrix elements have the form

$$\langle \gamma JLS \| \mathbf{P}^{(1)} \| \gamma J'L'S' \rangle = \delta_{SS'} (-1)^{L+S+J'+1} [J, J']^{1/2} \begin{Bmatrix} L & S & J \\ J' & 1 & L' \end{Bmatrix} \langle \gamma LS \| \mathbf{P}^{(1)} \| \gamma' L'S' \rangle \tag{2.29}$$

which is in terms of a Wigner $6j$-symbol (Equation C.5). The properties of this symbol lead to the following constraints. First, the initial spin must be preserved so that

$$\Delta S = S - S' = 0 \tag{2.30}$$

Second, the angular momenta may only change by a single quantum

$$\Delta L = L - L' = 0, \pm 1 \tag{2.31}$$

except that

$$L = L' = 0 \quad \text{is forbidden} \tag{2.32}$$

2.3.2 Higher Order Transitions and Metastable States

It is also possible for atoms to absorb or radiate photons through higher order processes such as electric quadrupole or magnetic dipole transitions. However, their considerably lower strengths imply that states that decay through these channels have much longer lifetimes. Another notable difference between these types of transitions and electric dipole radiation is that the former preserve parity of the initial state.

Magnetic dipole transitions have the same form as those for electric dipole radiation[66] given in Equation 2.26, except that the electric dipole operator is replaced with the magnetic dipole moment

$$\mu^{(1)} = -\mu_o \left[\mathbf{J}^{(1)} + (g_s - 1)\mathbf{S}^{(1)} \right] \tag{2.33}$$

in terms of the Bohr magneton

$$\mu_o = \frac{e\hbar}{2mc} = \frac{ea_o\alpha}{2} \tag{2.34}$$

and the anomalous gyromagnetic ratio for the electron $g_s \approx 2.0023192$.

If the gyromagnetic ratio is approximated to $g_s \approx 2$ and neglecting relativistic effects, the transition rate is given by

$$w_{M1} = \frac{4\omega^3 e^2 a_o^2 (\alpha/2)^2}{3\hbar c^3} \left| \langle \gamma J \| \mathbf{J}^{(1)} + \mathbf{S}^{(1)} \| \gamma' J \rangle \right|^2 \sum_q \begin{pmatrix} J & 1 & J' \\ -M & q & M' \end{pmatrix}^2 \tag{2.35}$$

which differs from Equation 2.26 by a factor of $(\alpha/2)^2$. It can be noted that magnetic dipole radiation follows the same selection rules as electric dipole transitions (Equations 2.27 and 2.28) due to the presence of identical Wigner $3j$-symbols. Thus, when viewed from the $\hat{\mathbf{z}}$ axis, only circularly polarized light is observed, as $\Delta M = 0$ transitions are still forbidden.

The difference between electric and magnetic dipole radiation instead occurs when viewed in a direction perpendicular to the $\hat{\mathbf{z}}$ axis. As the magnetic field vector takes the place of the electric field vector, the alignment of the field is perpendicular to the electric dipole case. Therefore, the polarizations are opposite and so when viewed from this direction $\Delta M = \pm 1$ transitions are now forbidden and only linearly polarized light will be observed.

One can also consider the selection rules imposed by LS-coupling. In this decoupled basis, the elements have the form

$$\begin{aligned} \langle \alpha LSJ \| \mathbf{J}^{(1)} + \mathbf{S}^{(1)} \| \alpha' L' S' J' \rangle &= \delta_{bb'} \sqrt{J(J+1)(2J+1)} \\ &+ \delta_{\alpha LS, \alpha' L' S'} (-1)^{L+S+J+1} [J, J']^{1/2} \begin{Bmatrix} L & S & J \\ 1 & J' & S \end{Bmatrix} [S(S+1)(2S+1)]^{1/2} \end{aligned} \tag{2.36}$$

Here, α represents all quantum numbers aside from LSJ and $b = \alpha LSJ$ (*ie.,* all quantum numbers). From the form of the matrix element, it can be seen that magnetic dipole transitions only occur between states with the same LS term which only differ by their J quantum number. The lack of radial dependence in this expression is the reason this type of radiation lacks a change of parity. In practice, transitions between $\Delta J = 0$ states may still occur. As real atoms depart from pure LS-coupling to some extent, all that is required is that the states contain some amount of a common basis state.

Electric quadrupole transitions can also be considered. The electric quadrupole operator is given by the rank two tensor

$$P_q^{(2)} = \sum_i r_i^2 C_q^{(2)}(i) \tag{2.37}$$

and the transition rate is of the same form as that for the dipole case (Equation 2.26) being

$$w_{E2} = \frac{e^2 a_o^2 \omega^5}{15\pi^2 \hbar c^5} \left| \langle \gamma J \| P^{(2)} \| \gamma' J \rangle \right|^2 \sum_q \begin{pmatrix} J & 2 & J' \\ -M & q & M' \end{pmatrix}^2 \tag{2.38}$$

Table 2.1: Selection rules and polarization for electric quadrupole radiation. Polarizations are given for observation along the $\hat{\mathbf{z}}$ axis ($\theta = 0°$), perpendicular to this axis ($\theta = 90°$) and for observation at other angles ($0° < \theta < 90°$).

	Polarization		
ΔM	$\theta = 0°$	$0° < \theta < 90°$	$\theta = 90°$
0	zero intensity	parallel to $\hat{\mathbf{z}}$	zero intensity
1	circular	elliptical	parallel to $\hat{\mathbf{z}}$
2	zero intensity	elliptical	perpendicular to $\hat{\mathbf{z}}$

but differing in the leading coefficient and a slight modification to the Wigner $3j$-symbol. The fact that this operator is even implies that the initial state's parity is preserved.

The selection rules for electric quadrupole transitions can be determined by considering the Wigner $3j$-symbol of Equation 2.38. From this, there are selection rules imposed on the J quantum number of

$$\Delta J = 0, \pm 1, \pm 2 \qquad J + J' \geq 2 \tag{2.39}$$

Selection rules are also imposed on ΔM which also determine the polarization of light observed along various directions. The selection rules and transition polarizations are summarized in Table 2.1.

In the LS-coupling regime, additional selection rules are further imposed. The first governs the orbital angular momentum with

$$\Delta L = 0, \pm 1, \pm 2 \tag{2.40}$$

while spin must be conserved so that

$$\Delta S = 0 \tag{2.41}$$

2.4 Conclusion

In this chapter, various elements of atomic structure have been discussed. It has been shown that the various sources of angular momenta such as orbital and spin vectors can couple together forming richer structure. The angular momentum properties of atomic states are also important when determining the types of optical transitions which may occur. While electric dipole radiation is often the dominant source of absorption and decay, higher order terms such as magnetic dipole and electric quadrupole radiation may also be important.

When dealing with atomic collisions, particularly with light atoms, a firm understanding of Russell-Saunders notation and angular momentum are important. As this work focuses on metastable atomic states which are optically forbidden, high order radiation terms are another important aspect to consider. For example, O(^{1}S) is a metastable state of oxygen

which will be widely studied but is optically forbidden and cannot decay through electric dipole radiation. Instead, it decays to the $O(^1D)$ state through electric quadrupole radiation or to the ground $O(^3P)$ state through either a magnetic dipole or an electric quadrupole transition.

Chapter 3

Molecular Structure

The structure of molecules can be determined much in the same way as atoms, by solving the Schrödinger equation for the nuclear and electronic constituents. There is however, additional complexity due to the fact that there are now multiple nuclei, breaking the spherical symmetry of the Coulomb field that occurs in atoms. In addition, there can now be movement of the nuclei about the centre of mass, producing rotational excitations. Oscillatory motion can also occur between different nuclei, inducing vibrational excitations. Electronic structure also becomes very complicated in comparison to atomic systems due the multiple charge centres and increased degrees of freedom. These factors combine to create a richer structure than what is present in atoms and is the focus of this chapter.

The chapter begins by describing the Born-Oppenheimer approximation, in which molecular structure is determined without considering nuclear motion, greatly simplifying calculations. This is followed by description of the angular momentum and symmetry properties of molecules. In later sections, rovibronic and electronic excitations are described in detail, which provides the mathematical language necessary to describe optical excitations of molecules and their associated selection rules. The chapter ends with a brief description of the Franck-Condon principle, which governs the branching ratios of electronic excitations in the rovibronic manifold of a given electronic state.

As molecular structure is a rich field, only a brief description of the results relevant to this work is provided. Both diatomic and polyatomic molecular systems are discussed with relevant differences being covered. As diatomic molecules possess certain symmetries and properties that can sometimes allow for more detailed structural descriptions than for polyatomic molecules, the diatomic case will be treated separately or in more detail where relevant.

3.1 The Born-Oppenheimer Approximation

Determining the exact solutions of the Schrödinger equation for many molecules is impossible[69, 70] to perform directly. Typically, one instead makes a series of approximations,

which allow the variables of interest to be separated in such a manner that the Schrödinger equation can then be solved independently for the individual parts. To achieve higher accuracy, one can then apply corrections for these approximations using[70] perturbative or variational methods.

The first, and most significant approximation which can be made is the *Born-Oppenheimer approximation*, operating under the assumption[71] that electronic transitions occur on much faster time scales than the motion of nuclei. Thus, one can treat the nuclei as being essentially static for determination of the electronic wave functions and these two sets of motion can be considered independent and separable.

In the case of diatomic molecules[69], the Hamiltonian under this approximation is

$$\mathbf{H} = \mathbf{T}^N(R,\theta,\phi) + \mathbf{T}^e(r) + V(r,R) \tag{3.1}$$

This expression considers the motion of the nuclei to be a two-body problem and expresses the energies as functions of the centre of mass position (R,θ,ϕ) and the relative distances of the electrons r from this centre. The Hamiltonian is expressed in terms of the kinetic energies of the nucleus $\mathbf{T}^N$ and electrons $\mathbf{T}^e$ and the electrostatic potential energy V. The nuclear kinetic energy term is referenced to the center of mass of the molecule with

$$\mathbf{T}^N(R,\theta,\phi) = -\frac{\hbar^2}{2\mu}\nabla^2 \tag{3.2}$$

where the nuclear reduced mass is

$$\mu = \frac{M_\mathrm{A} M_\mathrm{B}}{M_\mathrm{A} + M_\mathrm{B}} \tag{3.3}$$

as a function of M_A and M_Bs, the masses of atoms A and B. The electronic kinetic energy meanwhile is

$$\mathbf{T}^e(r) = -\frac{\hbar^2}{2m_e}\left[\sum_{i=1}^{n}\nabla_i^2 + \frac{m_e}{M_\mathrm{A}+M_\mathrm{B}}\sum_{i=1,j>i}^{n}\nabla_i\nabla_j\right] \tag{3.4}$$

which is summed over all n electrons.

For polyatomic molecules, an equations that is analogous to the diatomic case is given by Bunker and Jensen[70]

$$H = -\frac{\hbar^2}{2M}\left[\nabla_{CM}^2 + \sum_{r=2}^{N}\frac{M}{m_r}\nabla_r^2 + \sum_{r,s=2}^{N} M\nabla_r\cdot\nabla_s\right] \tag{3.5}$$

which is summed over all N electrons and nuclei, and is in terms of their total mass M and each particle's individual mass m_r. Equation 3.5, like Equation (3.1), is separated into the kinetic energy of the centre of mass and that of the constituents about this point. However, the polyatomic case cannot make use of the two body reduced mass technique used in the

diatomic case. Instead, a set of $3N-3$ co-ordinates are derived which separate the motion of the centre of mass from the particles about it. There are multiple methods for achieving this transformation[70] but their implementation is a discussion which is beyond the scope of this research and will not be expounded upon here.

It is useful to express the energy levels of the approximate Hamiltonians (3.1) and (3.5) as a sum of separate quantities

$$E = E^{el} + G(\nu) + F(J) \tag{3.6}$$

which gives the electronic E^{el}, vibrational $G(\nu)$ and rotational $F(J)$ energies as separate terms. It should be noted that these terms are also ordered in terms their total energy contribution to the system, with the electronic component being the biggest contributor. In the Born-Oppenheimer approximation, one can write the total molecular state as a direct product

$$|\psi^{BO}\rangle = |\psi^{el}\rangle \otimes |\chi_{\nu,J}\rangle \tag{3.7}$$

of the electronic $|\psi^{el}\rangle$ and roto-vibrational $|\chi_{\nu,J}\rangle$ states, known[69] as a Born-Oppenheimer product state. These states can be solved for independently and their solutions will be presented in the following sections.

3.2 Angular Momentum

Just as in atomic systems, the total angular momentum has contributions from the nuclear and electron spins as well as the orbital angular momenta of the electrons. For molecules however, there is also an additional momentum from the rotation of the molecular frame. One can form the total electronic orbital angular momentum and spins as in multi-electron atoms, adding the individual electrons' momenta vectorally with

$$\mathbf{L} = \sum_i \mathbf{l}_i \qquad \mathbf{S} = \sum_i \mathbf{s}_i \tag{3.8}$$

Another useful vector is the rovibronic angular momentum

$$\mathbf{N} = \mathbf{L} + \mathbf{R} \tag{3.9}$$

which includes the orbital angular momentum and that generated by rotation of the molecule $\mathbf{R}$ and a total momentum vector including electronic spin with

$$\mathbf{J} = \mathbf{L} + \mathbf{S} + \mathbf{R} \tag{3.10}$$

The angular momenta operators in molecules are evaluated in the same manner as in atoms using Equations 2.5 and 2.6. The eigenstates of $\mathbf{J}$ can also be decoupled[70] into rovibronic

and spin contributions using Wigner $3j$-symbols (Appendix C) as

$$|J, m_J\rangle = \sum_{m_N, m_S} (-1)^{N-S+m_J} \sqrt{2J+1} \begin{pmatrix} N & S & J \\ m_N & m_S & -m_J \end{pmatrix} |N, m_N\rangle |S, m_S\rangle \tag{3.11}$$

The total angular momentum, including the nuclear spin, is

$$\mathbf{F} = \mathbf{J} + \mathbf{I} = \mathbf{N} + \mathbf{S} + \sum_i \mathbf{I}_i \tag{3.12}$$

which sums over the spin of all nuclei in addition to the electronic spin and rovibronic terms. This can be written in a de-coupled basis as

$$|I, J, F, m_F\rangle = \sum_T (-1)^{I+S+N+F} \sqrt{(2T+1)(2J+1)} \begin{Bmatrix} I & S & T \\ N & F & J \end{Bmatrix} |T, N, F, m_F\rangle \tag{3.13}$$

where $\mathbf{T} = \mathbf{S} + \mathbf{I}$ is the total spin vector.

3.2.1 Diatomic Molecules

In atomic systems, the spherically symmetric Coulomb field implies that $\mathbf{L}$ is a constant of motion[65, 71]. For diatomic[69, 71] and linear polyatomic molecules[70] however, the axial symmetry of the system permits a more detailed description of the angular momentum properties than non-linear systems. The component of the angular momentum projected along this axis $\mathbf{L}_z$ is a well defined constant of motion, taking on quantized values while $\mathbf{L}$ precesses about the internuclear axis. This is analagous to the Stark effect in atomic systems[65] where an external electric field breaks the spherical symmetry of the atomic Coulomb field. One difference in diatomic molecules, however, is that the nuclear centres are both positively charges and so precession occurs in the same direction[71] when moving either way along the axis. This implies that the orbital angular momentum is *doubly degenerate*. For diatomic molecules, the orbital angular momentum is denoted by the symbol Λ which takes on values

$$\Lambda = |\mathbf{L}_z| \tag{3.14}$$

which can be denoted with the quantum number

$$\Lambda = 0, 1, 2, \ldots \quad (\Sigma, \Pi, \Delta, \ldots) \tag{3.15}$$

with Greek letters denoting the value in the same way that the angular momentum quantum number is denoted by the Latin letters S, P, D,... for atoms.

Diatomic molecules also introduce unique considerations for the electron spin. As in atoms, the orbital motion of the electrons for $\Lambda \neq 0$ induces a magnetic field which interacts with the electron spin. This results in a precession of the spin vector $\mathbf{S}$ about

Symbol	Description
C_n	one n-fold rotation axis
C_{nv}	one n-fold rotation axis and n reflection planes containing the axis
C_s	mirror plane symmetry
D_n	one n-fold rotation axis and n twofold rotation axes perpendicular to n
D_{nh}	belong to D_n with a reflection plane perpendicular to the n-fold rotation axis

Table 3.1: Some of the symmetry point groups relevant to this research. A more comprehensive list can be found in Bunker and Jensen[70].

the internuclear axis while the component $\mathbf{S}_z$ projected along the same axis remains constant[71]. This component $\mathbf{\Sigma}$ is described by the quantum number Σ and can take on values $S, S-1, \ldots, -S+1, -S$. It should be noted that the degeneracy in Λ does not apply for the electron spin and Σ can take on positive and negative values.

The total electronic angular momentum is also well defined along a specific internuclear axis as both $\mathbf{\Omega}$ and $\mathbf{\Sigma}$ point along this axis. The two vectors can be added algebraically and we can assign a total angular momentum quantum number

$$\Omega = |\Lambda + \Sigma| \tag{3.16}$$

which (for $\Lambda \neq 0$) takes on $2S+1$ possible values. In the case $\Lambda = 0$, degeneracy between the spin states still remains and Ω is a singlet state for a non-rotating molecule[71]. Regardless of the value of Λ, the multiplicity of the state is still denoted by $2S+1$.

3.3 Symmetries

The geometric structure of molecules have rotational and reflection symmetries in much the same way as macroscopic bodies. This symmetry is often specified using point groups which contain a definite set of rotations and reflections and is described using the language of group theory. The point group symmetries of molecules is a very broad topic[70] and an in depth discussion is beyond the scope of this work. However, a few results will be briefly discussed here.

The point group to which a molecule belongs is determined by the number of planes through which a molecule may be reflected, the angles by which it may be rotated that produce an identical configuration, and whether an inversion centre exists. Some of the point groups which are relevant to this work are provided in Table 3.1 and examples of molecules which are classified by these groups are given in Table 3.2.

In the case of diatomics, a term symbol may be assigned which classified the symmetries and angular momentum properties of the molecule (Section 3.3.1). However, for larger molecules the state cannot be as well specified and instead the states are typically denoted by it's multiplicity $(2S+1)$ and a character from its point group.

Symbol	Examples
C_n	CH_2O
C_{2v}	H_2O, D_2O
$C_{\infty v}$	HCN, OCS
C_s	CH_3OH
$D_{\infty h}$	CO_2, N_2

Table 3.2: Examples of molecules which are classified by the given molecular point groups.

3.3.1 Diatomic Molecules

In diatomic molecules, the unique description of a doubly degenerate orbital angular momentum furnishes a symmetry in the wave function due to the inability of these momentum states to uniquely describe the energy levels with wave functions which are properly symmetrized. A further symmetry is defined for linear molecules where the Coulomb field is such that the Coulomb field possesses a reflection symmetry about a certain point.

In these molecules, the double degeneracy of Λ for non-rotating systems implies that the wave functions are not properly symmetrized for the total Hamiltonian of the system[69]. It is necessary to use linear combinations of the two degenerate states to achieve the proper symmetry which is known as the *parity* of the system. This can be either positive or negative, depending on the linear combination, leading to even or odd parity states which are denoted by the symbols + and − respectively.

A second type of symmetry, known as *inversion symmetry*, applies to diatomic molecules where the nuclei have equal charge and some linear polyatomic molecules[70] where the nuclei are symmetric about some point on the internuclear axis. In these cases, there exists a *center of symmetry* in the molecule and the Coulomb field remains unaltered by reflection of the nuclei about this point. This implies that the wave function remains unchanged or differs by a sign upon reflection. That is, under the transformation

$$(x_i, y_i, z_i) \rightarrow (-x_i, -y_i, -z_i) \tag{3.17}$$

states which remain unchanged under this reflection are termed "gerade" while those which change sign are called "ungerade" and are given the symbols g and u respectively.

3.4 Rovibrational States

Molecules contain multiple nuclei that may change position relative to the molecular centre of mass. Adding energy to the molecule may induce rotation about some axis or the nuclei may exhibit oscillatory motions. Like other properties, these excitations are quantized into discrete states.

For diatomic molecules, rotations and vibrations occur about the centre of mass along

the internuclear axis[71] and the roto-vibrational energy can be determined by considering the kinetic energy of the centre of mass in Equation 3.1 where[69] the term

$$\mathbf{T}^N(R,\theta,\phi) = \mathbf{T}^N(R) + \mathbf{H}_{rot}(R,\theta,\phi) \tag{3.18}$$

can be separated into a vibrational and rotational component. The term responsible for vibrations can be approximated as a simple harmonic oscillator (Section 3.4.2) and the rotational part has the form

$$\mathbf{H}_{rot} = \frac{1}{2\mu R^2}\mathbf{R}^2 \tag{3.19}$$

For polyatomic nuclei, a more complex treatment is needed to develop a set of co-ordinates which describe the positions of all nuclei during rotation and vibration. While covering these transforms in detail is beyond the scope of this work, a full treatment of the method can be found in Bunker and Jensen[70]. In brief, one can represent the effects of rotation and vibration on the N nuclear co-ordinates in an irreducible and clearer way by separating the motion into translational, rotational and vibrational components. For general polyatomics, this representation consists of 3 translational, 3 rotational and $3N-6$ vibrational components. In the case of linear molecules, the representation consists of 3 translational, 2 rotational and $3N-5$ vibrational components. In this basis, one can find a molecule fixed axis with which to reference vibrations and apply rotation operators to this co-ordinate system to describe rotational motion of the molecule. In this fixed frame, one can use this set of *normal co-ordinates* Q_r and the corresponding conjugate momenta $\hat{\mathbf{P}}_r$, splitting vibrations into $3N-6$ or $3N-5$ modes which can be modelled as simple harmonic oscillators.

With these normal co-ordinates, one can describe the roto-vibrational structure using the Hamiltonian

$$\hat{\mathbf{T}}_N = \frac{1}{2}\sum_{\alpha,\beta}\mu_{\alpha\beta}(\hat{J}_\alpha - \hat{\rho}_\alpha - \hat{L}_\alpha)(\hat{J}_\beta - \hat{\rho}_\beta - \hat{L}_\beta) + \frac{1}{2}\sum_r \hat{P}_r^2 - \frac{\hbar^2}{8}\sum_\alpha \mu_{\alpha\alpha} \tag{3.20}$$

which accounts for rotational and vibrational motion along each co-ordinate. Assuming rotation occurs along the z axis is the fixed frame, this equation is summed over the co-ordinate indices $\alpha,\beta = x,y$ and $z, r = 1,2,\ldots,3N-6$. Here, $\hat{\mathbf{J}}_{\alpha\beta}$ are the rovibronic angular momentum components along the molecule fixed axis, $\hat{\rho}_{\alpha\beta}$ are proportional to the angular momenta of vibration[70] and $\mu_{\alpha\beta}$ are tensor components related to the molecule's moment of inertia. The first term accounts for the angular momentum of the molecular constituents about the centre of mass while the second is due to the contributions from vibration along the oscillating modes of the molecule. The final term

$$U = -\frac{\hbar^2}{8}\sum_\alpha \mu_{\alpha\alpha} \tag{3.21}$$

can be considered as a mass dependent contribution to the molecular potential energy which is related[72] to the molecule's moment of inertia in its equilibrium configuration.

Rather than fully solve the roto-vibrational term in Equation (3.20), one can approximate the energy of this system by considering it to be a rigid rotor. This is valid in the Born-Oppenheimer approximation, neglecting the electronic angular momentum $\hat{L}_{\alpha,\beta}$ along with the vibrational angular momenta components $\hat{\rho}_{\alpha,\beta}$. Under these conditions, the roto-vibrational motion is determined by the approximate Hamiltonian

$$\hat{H}_{rv} = \frac{1}{2}\sum_{\alpha} \mu^{e}_{\alpha\alpha}\hat{J}^{2}_{\alpha} + \frac{1}{2}\sum_{r}(\hat{P}^{2}_{r} + \lambda_{r}Q^{2}_{r}) \tag{3.22}$$

which separates the energy into a rigid-rotor term to account for rotation and a vibrational term which separates the energy into a sum over the $3N-6$ normal harmonic oscillator modes. With this separation of terms, one can then express the total wave function as a product of rotational and vibrational components with

$$\Phi_{rv} = \Phi_{rot}(\theta,\phi,\chi)\ \Phi_{vib}(Q_1, Q_2, \ldots) \tag{3.23}$$

which will be solved separately in the following subsections.

3.4.1 Rotations

In Equation 3.22, one approximates the rotational motion of the system to be that of a rigid rotor

$$H_{rot} = \frac{1}{2}\sum_{\alpha} \mu^{e}_{\alpha\alpha}\hat{J}^{2}_{\alpha} \tag{3.24}$$

This can be rewritten in terms of the principle axes of the system as

$$H_{rot} = \hbar^{-2}\left(A_e\hat{J}^{2}_{a} + B_e\hat{J}^{2}_{b} + C_e\hat{J}^{2}_{c}\right) \tag{3.25}$$

with rotational constants of the form

$$A_e = \frac{\hbar^2\mu^{e}_{aa}}{hc} \tag{3.26}$$

where B_e and C_e are in terms of μ^{e}_{bb} and μ^{e}_{cc} respectively and with the constants ordered as $A_e \geq B_e \geq C_e$.

The eigenvalues and corresponding wave functions of the rigid rotor will vary depending on the values of these rotational constants and fall into three cases:

1. The symmetric top for two equal constants
2. The spherical top for all constants equal
3. The asymmetric top where all constants are unequal

The most relevant case to this work is that of the symmetric top which is discussed below. However, all three systems have well known solutions[70].

The symmetric top may either be prolate or oblate, depending on if the leading or trailing rotational constants are equal. In the prolate case[70] where $A_e > B_e = C_e$, the energy eigenvalues are

$$E_{rot} = B_e J(J+1) + (A_e - B_e)k^2 \tag{3.27}$$

where the quantum numbers can take values $J = 0, 1, 2, \ldots$ and $k = 0, \pm 1, \ldots, \pm J$. Since the rotation has symmetry about the axis of the top, the entire system has $2J + 1$ fold degeneracy[73] over each eigenvalue and the rotational states can be designated by

$$|\Phi_{rot}\rangle = |J, k, m\rangle \tag{3.28}$$

which have[70] the associated wave functions

$$\Phi_{rot}(\theta, \phi, \chi) = \frac{1}{\sqrt{2\pi}} Y_m^J(\theta, \phi) e^{ik\chi} \tag{3.29}$$

On the other hand, the oblate case has $A_e = B_e > C_e$ with rotational energies

$$E_{rot} = B_e J(J+1) - (B_e - C_e)k^2 \tag{3.30}$$

and states also given by Equations 3.28 and 3.29.

3.4.2 Vibrations

The second term of Equation 3.22 represents vibrations of the molecule with

$$\hat{H}_{vib} = \frac{1}{2} \sum_r (\hat{P}_r^2 + \lambda_r O_r^2) \tag{3.31}$$

in terms of the normal co-ordinates of the molecule Q_r, the conjugate momenta $\hat{P}_r$ and λ_r which is proportional to the mode's vibrational frequency. The solution to the Schrödinger equation for this system is well known[65], having energy eigenvalues of the form

$$E(\nu) = \hbar \lambda^{1/2} \left(\nu + \frac{1}{2} \right) \tag{3.32}$$

which is in terms of the oscillation frequency ν and its related constants

$$\lambda^{1/2} = \omega = \hbar \gamma = 2\pi\nu \tag{3.33}$$

The wavefunction solutions are in terms of the Hermite polynomials

$$\Phi_\nu(Q_r) = N_\nu H_\nu(\gamma^{1/2} Q_r) \exp\left[-\frac{\gamma Q_r^2}{2}\right] \tag{3.34}$$

and normalized by the constant

$$N_\nu = \sqrt{\frac{\gamma^{1/2}}{\pi^{1/2} 2^\nu \nu!}} \tag{3.35}$$

When considering the vibrational energy of a molecule, which is approximated as a series of oscillators along each molecule bond, one can determine the total vibrational energy by summing over all modes with

$$E_{vib} = \sum_r \hbar\omega_r \left(\frac{1}{2} + \nu_r\right) \tag{3.36}$$

where $\nu_r = 0, 1, \ldots$. The corresponding vibrational wavefunctions are simply the products of those for the individual harmonic oscillators over each mode of vibration with

$$\Phi_{vib} = \exp\left[-\frac{1}{2}\sum_r \gamma_r Q_r^2\right] \prod_r N_{\nu_r} H_{\nu_r}\left(\sqrt{\gamma_r} Q_r\right) \tag{3.37}$$

3.5 Electronic States

To determine the electronic wave functions, one must solve the Schrödinger equation for the Hamiltonian

$$H_{elec} = -\frac{\hbar^2}{2m_e}\sum_i^n \nabla_i^2 + \sum_{i<j}^n \frac{e^2}{4\pi\epsilon_o R_{ij}} - \sum_\alpha^N \sum_i^n \frac{Z_\alpha e^2}{4\pi\epsilon_o R_{i\alpha}} \tag{3.38}$$

summed over all n electrons and N nuclei, depending on the inter-particle distances R_{ij}. This Hamiltonian can be approximated by neglecting the electronic interactions of the second term in which reduces the expression to a series of n one-electron Hamiltonians

$$H_{elec}^0 = \sum_i^n \left\{-\frac{\hbar^2}{2m_e}\nabla_i^2 - \sum_\alpha^N \frac{Z_\alpha e^2}{4\pi\epsilon_o R_{i\alpha}}\right\} \tag{3.39}$$

Formally[70], the electron wave function is given as a product of the one-electron wave functions

$$\Phi_{elec} = \phi_a(\mathbf{r}_1)\phi_b(\mathbf{r}_2)\ldots\phi_\lambda(\mathbf{r}_n) \tag{3.40}$$

In principle, one now has the electronic wave functions which, combined with the roto-vibrational wave functions, provides the necessary components to determine the structure of the molecule within the Born-Oppenheimer approximation as per Equation 3.7. In practice, however, the calculation of these electronic functions is quite difficult[66, 70] and there are

many methods and approximations which may be employed, depending on the use case at hand. These techniques are beyond the scope of this work and will not be discussed further.

3.6 Molecular State Designation

In atomic systems, one can fully describe all excited states in terms of their radial and angular momentum quantum numbers resulting in well specified state designations. For molecules, the situation is more complex and can even become ambiguous for larger systems.

For diatomic molecules, where the orbital and spin angular momenta are well specified, it is possible to give a detailed description of the angular momentum and symmetry properties of a molecule using molecular term symbols. These symbols are very similar to the Russell-Saunders notation used to specify atomic states, written as

$$^{2S+1}\Omega^{\pm}_{g,u} \tag{3.41}$$

specifying the multiplicity of the state $2S+1$, the total electron angular momentum Ω and the parity of the state $\pm$. Furthermore, for homonuclear systems, the type of reflection about the centre of symmetry g or u is also given (Section 3.3.1). To differentiate the multiple electronic excited states with the same term symbols, it is necessary to introduce another designation. Starting from the ground state, one can order exciting states ascending in energy. Using the letter X to designate the ground state, one can proceed alphabetically for excited states using the letters A, B, C, etc. This leads to states such as $X^1\Pi^-$ or $B^3\Delta_g^+$.

In the case of polyatomic molecules, descriptions of excited states are further complicated. The inability to specify molecular term symbols in the same manner as diatomic systems, with the exception of some linear molecules, prevents an exact description of the angular momentum of the system in any given excited state. Furthermore, the possible symmetries present in these molecules imply that multiple excited states exhibit the same spectra. As such, the language of group theory are used to specify excited states of these molecules. The descriptions of the excited states are dependent on the point group symmetry to which the molecule belongs[70] giving different specification for the various groups.

3.7 Electric Dipole Transitions

In molecules, just as in atoms, there are various selection rules which determine the allowed optical transitions based on considerations of angular momentum and symmetry. Molecules however, impose further restrictions on transition probabilities due to the added complication that transitions can also occur between roto-vibrational levels. In this section, the various optical transition rules are outlined and the Franck-Condon principle is described with its applications to absorption and emission spectra.

3.7.1 General Selection Rules

Molecular systems have selection rules that determine the allowed electric dipole transitions. The additional symmetries and classifications of molecular states also mean that these rules are different from the atomic case but both sets have similarities as well. For molecules, there are rigorous selection rules governing the allowable parities and change in angular momenta between the initial and final states. Other rules can be seen to apply for transitions between differing roto-vibrational states in addition to absorption and emission which result in electronic transitions within the molecule.

The first rigorous rule dictates[71] the parities of initial and final electronic states. All optical transitions must occur between differing parities and are forbidden for like parities. That is

$$+ \leftrightarrow - \qquad + \nleftrightarrow + \qquad - \nleftrightarrow - \tag{3.42}$$

implying that transitions such as $2^1\Sigma^+ \rightarrow 1^1\Sigma^-$ are permitted but $2^1\Sigma^+ \rightarrow 1^1\Sigma^+$ are not. A second rule is that the total angular momentum of the final state cannot change by more than one quanta so that

$$\Delta F = 0, \pm 1 \quad (\text{for } F', F'' \geq 1) \tag{3.43}$$

which is required to conserve the total spin of the photon and molecule.

Further selection rules are imposed under the Born-Oppenheimer approximation (Section 3.1) where the transition line strength is found from[70] the matrix elements of the dipole operator

$$S(f \leftarrow i) = \sum_{\Phi'_{int}, \Phi''_{int}} \sum_{\sigma=-1}^{1} \left| \langle \Phi'_{int} | \mu_s^{(1,\sigma)} | \Phi''_{int} \rangle \right|^2 \tag{3.44}$$

summed over the three radiation polarizations $\sigma = 0, \pm 1$ and the set of internal degrees of freedom of the initial and final states Φ'_{int} and Φ''_{int} respectively. Assuming that the wavefunctions are separable into nuclear, spin, rotational, vibrational and electronic components as

$$|\Phi'_{int}\rangle = |\Phi'_{nspin}\rangle \, |\Phi'_{rot}\rangle \, |\Phi'_{vib} \Phi_{elec}^{(e',S',m'_S)}\rangle \tag{3.45}$$

the matrix elements over each of these components can then be evaluated separately, taking the product can then be used to find the total line strength.

One can consider the rotational factor by first expressing[70] the rotational state as a linear combinations of symmetric top states (Equation 3.28) with

$$|\Phi_{rot}\rangle = \sum_{k=-N}^{N} c_k^{(N)} \, |N, k, m\rangle \tag{3.46}$$

The rotational component is then evaluated by considering the matrix elements of a rotation

about an arbitrary fixed axis

$$\langle \Phi'_{rot}|U_s^{(1,\sigma)}|\Phi''_{rot}\rangle = \sum_{k'=-N'}^{N'} \sum_{k''=-N''}^{N''} c_{k'}^{(N')} c_{k''}^{(N'')} \langle N', k', m'|U_s^{(1,\sigma)}|N'', k'', m''\rangle \tag{3.47}$$

This equation can be further simplified through the use of Wigner 3-j symbols as

$$\begin{aligned}\langle N', k', m'|U_s^{(1,\sigma)}|N'', k'', m''\rangle \\ = (-1)^{k'+m'}\sqrt{(2N''+1)(2N'+1)} \begin{pmatrix} N'' & 1 & N' \\ k'' & \sigma' & -k' \end{pmatrix} \begin{pmatrix} N'' & 1 & N' \\ m'' & \sigma' & -m' \end{pmatrix}\end{aligned} \tag{3.48}$$

One can also consider the electro-vibrational component of the line strength as

$$\langle \Phi'_{vib}\Phi_{elec}^{(e',S',m'_S)}|\mu_m^{(1,\sigma')}|\Phi''_{vib}\Phi_{elec}^{(e'',S'',m''_S)}\rangle = \langle \Phi'_{vib}|\mu_m(e',e'')|\Phi''_{vib}\rangle \tag{3.49}$$

where the electronic integrals have been written in terms of the *electronic transition moment function*

$$\mu_m(e',e'') = \langle \Phi_{elec}^{(e',S',m'_S)}|\mu_m^{(1,\sigma')}|\Phi_{elec}^{(e'',S'',m''_S)}\rangle \tag{3.50}$$

Collecting all of these results, one obtains a general expression for the line strength

$$\begin{aligned}\langle \Phi'_{int}|\mu_S^{(1,\sigma)}|\Phi''_{int}\rangle = \langle \Phi'_{nspin}|\Phi''_{nspin}\rangle\,(-1)^{m'}\sqrt{(2N''+1)(2N'+1)} \\ \times \begin{pmatrix} N'' & 1 & N' \\ m'' & \sigma & -m' \end{pmatrix} \sum_{k'=-N'}^{N'} \sum_{k''=-N''}^{N''} (-1)^{k'} c_{k'}^{(N')*} c_{k''}^{(N'')*} \\ \times \sum_{\sigma'=-1}^{1} \langle \Phi'_{vib}|\mu_m^{(1,\sigma')}(e',e'')|\Phi''_{vib}\rangle \begin{pmatrix} N'' & 1 & N' \\ k'' & \sigma' & k' \end{pmatrix}\end{aligned} \tag{3.51}$$

Equation 3.51 can be reduced to a much simpler expression by considering the degeneracies which are typically present in a molecular system. In the Born-Oppenheimer approximation, one neglects the effects of nuclear transitions on the final line strength so that $\Phi'_{nspin} = \Phi''_{nspin}$, introducing a g_{ns}-fold degeneracy to account for the number of possible nuclear spin states. A second degeneracy exists as optical dipole transitions preserve the electron spin and so $m'_S = m''_S$, meaning that there will be $(2S+1)$ spin states in each dipole transition element. Finally, there is an additional m-degeneracy as the total momentum sublevel remains unchanged with $m' = m''$ and summation over the $3j$-symbols of Equation (3.51), which depend on m' and m'', are related[73] by

$$\sum_{\sigma=-\omega}^{\omega} \sum_{m''=-N''}^{N''} \sum_{m'=-N'}^{N'} \begin{pmatrix} N'' & 1 & N' \\ m'' & \sigma & -m' \end{pmatrix} = 1 \tag{3.52}$$

Summing over all of the degeneracies, one can obtain a final expression for the line

strength

$$\begin{aligned} S(f \leftarrow i) = g_{ns}(2S+1)(2N''+1)(2N'+1) \\ \times \left| \sum_{k'=-N'}^{N'} \sum_{k''=-N''}^{N''} c_{k'}^{(N')} c_{k''}^{(N'')} \right. \\ \left. \times (-1)^{k'} \sum_{\sigma'=-1}^{1} \langle \Phi'_{vib} | \mu_m^{(1,\sigma')} | \Phi''_{vib} \rangle \begin{pmatrix} N'' & 1 & N' \\ k'' & \sigma' & -k' \end{pmatrix} \right|^2 \end{aligned} \tag{3.53}$$

The Wigner 3-j symbol present in this expression then imposes a further selection rule

$$\Delta N = 0, \pm 1 \qquad (N' = 0 \nleftrightarrow N'' = 0) \tag{3.54}$$

3.7.2 Electronic Transitions

For transitions between electronic states in a molecular system, the vibrational and electronic components of the transition strength can be considered separately. Taking the Taylor expansion of the transition moment

$$\mu_\alpha(e', e'') = \mu_\alpha^{(0)}(e', e'') + \sum_r \mu_\alpha^{(r)}(e', e'') Q_r + \frac{1}{2} \sum_{r,s} \mu_\alpha^{(r,s)} Q_r Q_s + \dots \tag{3.55}$$

One can approximate the transition strength in terms of the zeroth order term of the moment[70] yielding

$$| \langle \Phi'_{vib} | \mu_\alpha(e', e'') | \Phi''_{vib} \rangle |^2 \approxeq \left| \mu_\alpha^{(0)}(e', e'') \right|^2 \left| \langle \Phi'_{vib} | \Phi''_{vib} \rangle \right|^2 \tag{3.56}$$

From this expression, one sees that the line strength depends on the dipole moment between the two electronic states and a separate term which considers the overlap of the vibrational levels. While these levels within a single electronic state are orthogonal, this is not always the case between those in different electronic levels, and so one can calculate a non-zero overlap integral.

The zeroth order electronic integral $\mu_\alpha^{(0)}(e', e'')$ follows the same angular momentum selection rules applying to atomic systems (Section 2.3.1) and the matrix element can be determined in a similar manner as atoms. The key difference here is that the transitions obey the Franck-Condon principle which is encoded in the second term $|\langle \Phi'_{vib} | \Phi''_{vib} \rangle|^2$, known as the Franck-Condon factor.

Classically, the Franck-Condon principle[74] is based on the idea that electronic transitions occur on much shorter time scales[75] than the nuclear motion of vibration and rotation. The time scale then implies that the kinetic energy of the electron should be the same immediately before and after an electronic transition. As the electrons tend to spend the majority of their time at the outer edges of the potential well during vibration, the ma-

jority of transitions can be expected to occur at these classical turning points rather than in the middle of the well. This implies that transitions should mostly occur between vibrational levels whose potential energy curves have inner or outer edges which align, allowing one to predict the relative strength of transitions within a vibrational band.

The Franck-Condon principle is illustrated in Figure 3.1. Here the molecular potential curves for the ground and a single electronic excited state, E_0 and E_1 respectively, are shown along with the wave functions for their associated vibrational bands. Consider absorption from the ground state $E_0(\nu'' = 0)$. As there is significant overlap between this wave function and that of the $E_1(\nu' = 2)$ excite state, the strength of this transition should be much higher than that of the neighbouring vibrational levels where the Franck-Condon factor $|\langle\Psi'_{vib}|\Psi''_{vib}\rangle|^2$ is lower. Similarly, decay along the $E_1(\nu' = 0) \rightarrow E_0(\nu'' = 2)$ transition should be stronger than into other vibrational states due to the larger overlap of the wavefunctions.

3.8 Magnetic Dipole and Electric Quadrupole Transitions

Higher order transitions can also occur in molecular systems. If excited states are unconnected to the ground state by electric dipole transitions, this can lead to metastable molecular states in analogy to their atomic counterparts (Section 2.3.2). The transition amplitudes for magnetic dipole and electric quadrupole transitions are[70] about 10^{-5} and 10^{-8} times those of electric dipole transitions, respectively. Here, the transition amplitudes and selection rules for magnetic dipole and electric quadrupole transitions for molecular states are described as well as their selection rules which determine the molecular states that will be metastable. Below, we outline the results of Bunker and Jensen[70] for these transitions.

Magnetic dipole line strengths are determined by the transition amplitude $\langle\Phi'_{int}|d_A|\Phi''_{int}\rangle$ in terms of the magnetic dipole moment d_A where A represents the space fixed magnetic dipole components. The line strengths have the same form as those of electric dipole transitions but differ by an extra factor of c^2 and the replacement of the electric dipole operator μ_A with d_A. However, the line strength cannot be calculated within the Born-Oppenheimer approximation as they are dependent on both the electronic and nuclear spins. However, some selection rules for these transitions can be presented. First, parity must be preserved in the transition so that the initial and final states must follow

$$+ \leftrightarrow + \qquad - \leftrightarrow - \qquad + \nleftrightarrow - \tag{3.57}$$

An additional selection rule is placed on the angular momentum as

$$\Delta F = 0, \pm 1 \qquad (F' = 0 \nleftrightarrow F'' = 0) \tag{3.58}$$

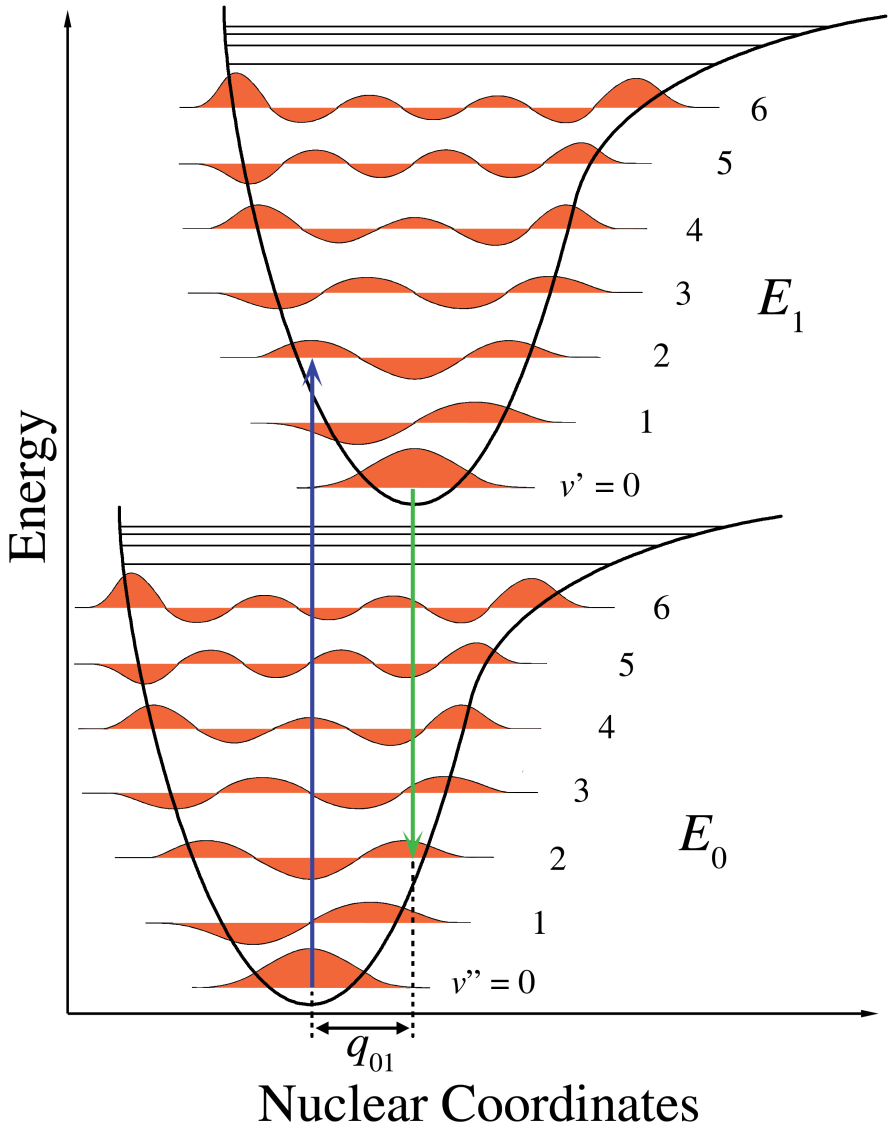

Figure 3.1: Illustration of the Franck-Condon principle used with permission from Somoza[76]. Absorption of photons along the $E_0(\nu'' = 0) \rightarrow E_1(\nu' = 2)$ transition is preferential due to the significant overlap of the vibrational wavefunctions for these two states. Decay along the $E_1(\nu' = 0) \rightarrow E_0(\nu'' = 2)$ transition is likewise more probable as these states also exhibit a strong overlap.

In the case of electric quadrupole transitions, the line strength is calculated in much the same manner as electric dipole transitions (Equation 3.44) but in terms of the components of the electric quadrupole momentum

$$P(f \leftarrow i) = \sum_{\Phi'_{int},\Phi''_{int}} \sum_{\sigma=-2}^{2} \| \langle \Phi'_{int} | Q_s^{(2,\sigma)} | \Phi''_{int} \rangle \|^2 \tag{3.59}$$

The matrix elements can be derived using the same method as for electric dipole transitions leading to the expression

$$\begin{aligned} P(f \leftarrow i) = {} & g_{ns}(2S+1)(2N''+1)(2N'+1) \\ & \times \left| \sum_{k'=-N'}^{N'} \sum_{k''=-N''}^{N''} c_{k'}^{(N')*} c_{k''}^{(N'')} \right. \\ & \left. \times (-1)^{k'} \sum_{\sigma'=-2}^{2} \langle \Phi'_{vib} | \mu_m^{(2,\sigma')} | \Phi''_{vib} \rangle \begin{pmatrix} N'' & 2 & N' \\ k'' & \sigma' & -k' \end{pmatrix} \right|^2 \end{aligned} \tag{3.60}$$

The differences between Equations (3.53) and (3.60) can be seen in the indices of the summation, the use of the electric quadrupole rather than the dipole operator and a change from a 1 to a 2 in the Wigner $3j$-symbol. Based on the properties of the latter symbol, the only permitted transitions are those for which

$$\Delta N = 0, \pm 1, \pm 2 \tag{3.61}$$

3.9 Conclusion

In this chapter, an outline of molecular structure is presented. Both rovibrational and electronic transitions have been described as well as the types of radiative absorptions and decays which are possible in molecular systems. In this work, an understanding of excited state designations for both diatomic and polyatomic systems are important as collision experiments are performed with a range of systems including simpler molecules like N_2 and larger targets like methanol. While studies of diatomic and linear molecules often employ molecular term symbols, large polyatomic molecules are described in terms of group theory and so an understanding of both are important. Finally, as metastable molecular states are discussed in the experimental work, and understanding of molecular radiation beyond electric dipole transitions is necessary and so it is important to also understand magnetic dipole and electric quadrupole transitions in molecules.

Chapter 4

Electron-Impact Collisions

In this chapter, a brief overview of the theory of electron-impact collisions is presented, focusing on the areas which are most relevant to the experimental studies discussed later in this work. The chapter begins with a basic description of some results from fundamental scattering theory, presenting elements of both the classical and quantum pictures which are relevant to the topic of electron scattering. Later in the chapter, phenomenological and theoretical descriptions of some electron scattering processes are presented, with a focus on inelastic collisions. This includes discussion of both electron-impact excitation to bound states of atoms and molecules and dissociative excitation in molecular systems.

4.1 Scattering Theory

Pure scattering theory is a wide ranging subject. In this section, both classical and quantum mechanical scattering theory are discussed focusing on the elements relevant to electron collisions. First, concepts of classical scattering which make appearances throughout the remainder of the chapter are presented. This is followed by a quantum mechanical description of scattering, providing an exact equation for describing the interaction of the initial and final states with the system's potential. The first Born approximation is then described, which is useful in making the exact solution of the scattering problem more tractable in terms of a perturbation theory. Finally, various relevant cross sections for inelastic electron scattering processes are defined which provide for experimentally achievable measures of scattering.

4.1.1 Classical Scattering

While classical scattering is not directly applicable to electron-scattering, as the latter is a quantum mechanical problem, there is still utility in considering a semi-classical description of electron impact. Here, we consider some of the elements of scattering in the context of classical mechanics which are quite relevant to the present work.

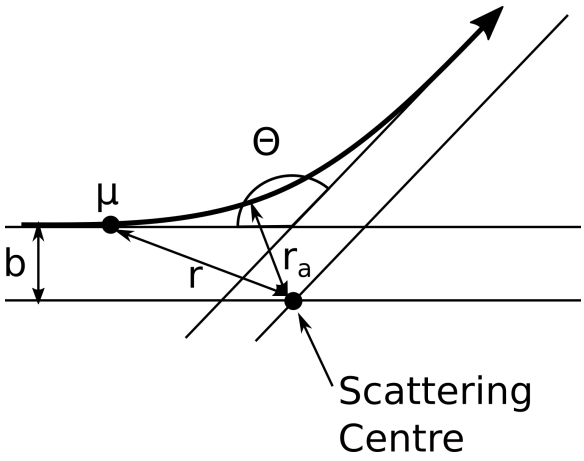

Figure 4.1: Diagram of the two-body classical scattering problem in the centre-of-mass frame. Seen is the centre of mass μ approaching the scattering centre with incoming separation given by the impact parameter b. The separation distance r is indicated in the diagram as well as the scattering angle Θ.

Typically, one considers the scattering process to be a two-body phenomenon. Obviously, this picture is invalid for dissociative collisions where the target fragments; however, it is generally valid for other types of inelastic scattering. Rather than working in the lab frame where the projectile and target with masses m_p and m_t have positions $\mathbf{r}_p$ and $\mathbf{r}_t$, one can work in the center of mass frame which greatly simplifies the mathematics of the problem[77].

In order to move to this frame, one can introduce the center-of-mass co-ordinates. The first quantity is its position

$$\mathbf{R} = \frac{m_p \mathbf{r}_p + m_t \mathbf{r}_t}{m_p + m_t} \tag{4.1}$$

and the second, the reduced mass

$$\mu = \frac{m_p m_t}{m_p + m_t} \tag{4.2}$$

A third co-ordinate describes the separation of the two bodies

$$\mathbf{r} = \mathbf{r}_p - \mathbf{r}_t \tag{4.3}$$

An example of a classical scattering problem can be seen in Figure 4.1 within the center-of-mass frame. Rather than considering the approach of the projectile particle to within the potential of the target, the motion of the center-of-mass is considered. The important parameters to consider in this situation are the center of mass m_c, the impact parameter b and the scattering angle Θ. The impact parameter defines the perpendicular distance of between μ and the scattering centre during the collision while Θ is a measure of the deflection during scattering.

4.1.2 Quantum Treatment of Scattering

The quantum scattering problem considers[65] the evolution of both the projectile and target as a single system. In the non-relativistic limit, this evolution occurs according to the time-dependent Schrödinger equation

$$i\hbar\frac{\partial}{\partial t}\left|\Psi(t)\right\rangle = H\left|\Psi(t)\right\rangle \tag{4.4}$$

where the Hamiltonian consists of three components

$$H = T + H_o + V \tag{4.5}$$

including the kinetic energy of the projectile T, the target's Hamiltonian H_o, and the potential energy generated by the interaction between the target and projectile V.

We can consider the system to initially be in some product state

$$\left|i\right\rangle = \left|\mathbf{k}\right\rangle\left|n_i\right\rangle \tag{4.6}$$

which describes the incoming projectile as a plane wave state with wave vector $\mathbf{k}$ and the target to be in some initial state $\mathbf{n_i}$ being defined by all pertinent quantum numbers. We can assume that there exists some basis in which the initial state is described as

$$\left|i\right\rangle = \sum_j \left|j\right\rangle a_{ji} \qquad\qquad \left|j\right\rangle \equiv \left|\mathbf{k}_j\right\rangle\left|n_j\right\rangle \tag{4.7}$$

so that the total energy of the states $\left|i\right\rangle$ are then eigenstates of the operator $T + H_o$ with energies

$$E_i = \frac{\hbar^2 k^2}{2\mu} + \varepsilon_i \tag{4.8}$$

where ε_i is the internal energy of the target and k is the projectile's initial wave number.

If the initial state is also an eigenvalue of the full Hamiltonian (4.5) then it is also true that

$$H\sum_j \left|j\right\rangle a_{ji} = \sum_j (E_j + V)\left|j\right\rangle a_{ji} = \sum_j \left|j\right\rangle a_{ji}E_i \tag{4.9}$$

So that if we project this onto the final state of the system $\left|f\right\rangle$ then

$$\left\langle f|H|i\right\rangle = E_f a_{fi} + \sum_j \left\langle f|V|j\right\rangle a_{ji} = a_{fi}E_i \tag{4.10}$$

where the term $\left\langle f|V|j\right\rangle$ is the transition amplitude and the projection coefficients are defined by

$$a_{ji} = \left\langle j|i\right\rangle \qquad a_{fi} = \left\langle f|i\right\rangle \tag{4.11}$$

Equation 4.10 encapsulates the interaction between the projectile and target. Solving the scattering problem is then equivalent to determining this interaction term. To find this amplitude, one integrates this kernel[78] over the space of particle positions and internal degrees of freedom of the target through the equation

$$\langle f|V|i\rangle = \int d\mathbf{r} \int d\tau \; e^{-i\mathbf{k}'\cdot\mathbf{r}} \psi_f^*(\tau) V(\mathbf{r},\tau) \psi_i(\tau) e^{i\mathbf{k}\cdot\mathbf{r}} \tag{4.12}$$

At this point, the scattering solution is *exact* involving no approximations.

4.1.3 The Born Approximation

In many cases, exact methods of solution to the scattering amplitude (4.12) are intractable. A useful simplification in situations where scattering of the incoming wave is weak is the *Born approximation*. This is essentially the assumption that the scattered wave can be treated as a perturbation of the incoming wave[77, 78] so that the projectile remains an external entity from the target's constituents and as such, one only needs to consider an interaction potential between the two bodies rather than some intermediary complex. As such, we can represent the state of the system using a set of stationary states[78] that describe the projectile as a free particle and the target as an independent entity subject to its own Hamiltonian H_o.

In the Born approximation, we consider the wave function of the final state to be an asymptotic solution which is a superposition of a plane wave of the same form as the incoming wave and a weakly scattered wave. That is, the final wave has the form[77] for $r \gg 1$ of

$$\psi_f = \psi_{inc} + \psi_{scatt} \approx e^{ikz} + \frac{e^{ik\mathbf{r}}}{r} f(\Theta) \tag{4.13}$$

where we assume a spherical symmetry where the z-axis is aligned along the projectiles incoming direction and ψ_{inc} is normalized to unity for convenience. Under this assumption, the transition amplitude can be approximated[78] as

$$a_{fi} = \delta_{fi} + a_{fi}^{(1)} + \ldots \tag{4.14}$$

neglecting higher order terms. This reduces (4.9) to

$$(E_i - E_f) a_{fi}^{(1)} = \langle f|V|i\rangle \tag{4.15}$$

Note that the left hand side may vanish in the elastic case where $E_i = E_f$ and so dividing both sides by the energy difference may introduce a singularity. As such, determining the scattering coefficient $a_{fi}^{(1)}$ requires the use of complex contour integration[65].

Substituting the asymptotic wave function (4.13), it is possible to solve for the scattering coefficient $a_{fi}^{(1)}$. A full mathematical treatment of this procedure can be found in Fano and

Rau[78]. The end result is that the solution for the scattered wave in the Born approximation can be expressed in the form

$$\psi_{scatt} = -\sqrt{\frac{2\pi\mu^2}{\hbar}} \sum_{n_f} \langle \bar{f}|V|i\rangle \, \psi_f \frac{e^{i\bar{k}'r}}{r} + \mathcal{O}\left(\frac{\hbar}{\bar{k}'r}\right)^2 \tag{4.16}$$

where the final state $|\bar{f}\rangle$ is defined by

$$|\bar{f}\rangle = |\bar{k}'_f\hat{\mathbf{r}}, n_f\rangle \qquad\qquad \bar{k}' \equiv \sqrt{2\mu E_{fp}} \tag{4.17}$$

in terms of the reduced mass μ, the final projectile energy E_{fp}, the final state of the target $|n_f\rangle$, and the scattered projectile's momentum state $|\bar{k}'_f\rangle$.

4.1.4 Cross Sections

The probability for a particle collision process to occur is quantified[79] through its corresponding scattering cross section value. This is the quantity typically measured in collision experiments where scattered particles are usually the object being counted. Since setups can vary in their ability to differentiate between types of scattered particles or to resolve their distributions as functions of angle or other parameters, it is often necessary to work with different cross sectional measures depending on the experiment at hand. In this section, various cross sectional values and their interpretations are described.

The term cross section is originally derived from classical scattering[77] of objects such as hard spheres where it defined the area which a target presented to a projectile and within which, a scattering event may occur. Of course, this picture breaks down when describing scattering between quantum mechanical objects where a wave function description is necessary. While the name persists for historical reasons, the quantity now can be understood in its more modern sense as a measure of the probability that a scattering event may occur.

A differential cross section quantifies the scattering probability as a function of the angle that the outgoing particle makes with the incoming trajectory. The number of particles N_i scattered into a solid angle element $d\Omega$ making an angle (θ, ϕ) with the incident momentum vector $\mathbf{k}_i$ is given by

$$N_i = \frac{d\sigma_i(E_0, E_i, \theta, \phi)}{d\Omega} N_e N_t \tag{4.18}$$

in terms of the number of incident and target particles N_e and N_t and the differential cross section $d\sigma/d\Omega$. One can also arrive at the doubly differential cross section[79] if one also considers the distribution of final energies, so that the number of scattered particles with energies between E_i and $E_i + dE_i$ is $d^3\sigma/dE_i d\Omega$.

If one integrates the differential cross section over all angles, one arrives at the integral cross section

$$\sigma_i(E_0) = \int d\Omega \; \frac{d\sigma_i(E_0, \Omega)}{d\Omega} \tag{4.19}$$

Another associated quantity that may be of utility is the momentum transfer cross section, which quantifies the average momentum imparted by the incoming projectile when scattering off the target and is given by

$$\sigma_i^{MT}(E_0) = \int d\Omega \left[1 - \frac{k_i}{k_0}\cos\theta\right] \frac{d\sigma_i(E_0,\Omega)}{d\Omega} \tag{4.20}$$

and is quantified in terms of the fractional loss of directed momentum $[1-(k_i/k_o)\cos\theta]$ of the projectile during collision.

Scattering can also be quantified by the total scattering cross section that quantifies all possible scattering events. That is, the cross section summed over all possible scattering channels, angles and energies

$$\sigma_T(E_0) = \sum_i \int\int d\Omega\ dE_i\ \frac{d^3\sigma_i(E_0,E_i,\Omega)}{dE_i d\Omega} \tag{4.21}$$

4.2 Electron Scattering

Electron-impact collisions are mainly concerned with the scattering of an electron projectile off an atomic or molecular target. The fact that both the projectile and the constituents of the target are charged particles implies that a Coulomb interaction occurs between them. The long range nature of the $1/r$ dependent Coulomb potential implies that interaction between the scattering potential and the projectile occur well into the asymptotic limit, and so typically, electron-impact is considered within the context of the Coulomb scattering problem[65, 77]. Its formulation is itself is deserving of a fairly long description but will not be discussed here. Instead, the reader is encouraged to consult one of the many texts on the subject including Sakurai[65] and McDaniel[77].

In this section, we first describe phenomenologically some types of scattering processes which may be observed. This broad overview is then followed by more in depth discussions of some of the types of scattering which are encountered in this work. A physical understanding of the types of inelastic scattering leading to bound state excitation in the target is given as well as an explanation for their strengths at various energies. This is followed by a mathematical description of the energy dependence of the cross section values for inelastic scattering, with a focus on the high energy range. Finally, we end with a description of the mechanisms behind different types of dissociative excitation in molecular systems.

4.2.1 Scattering Phenomena

There are several types of processes which may occur during an electron collision event which are either elastic, resulting in a transfer of momentum to the target, or inelastic in which energy is also transferred to the target and causes a change in it's internal configuration. In this section, various classes of scattering phenomenon are described which are relevant

to this research.

One type of scattering which can occur is an elastic collision, where only momentum is transferred to the target through the reaction

$$X + e \rightarrow X + e \tag{4.22}$$

and the projectile leaves with its initial energy.

It is also possible for inelastic scattering to occur with excitation to a bound state, sometimes called electron-impact excitation, which can be described by the general equation

$$X + e \rightarrow X^* + e' \tag{4.23}$$

where the target is left in some excited state X^*. The state to which the target is excited will be dependent on the amount of energy transferred from the projectile and the internal structure of the target.

In cases where that the energy transfer is sufficiently high, it may be possible for one or more of the electrons which are bound to the target to be excited above their binding energy and ejected. This results in ionization of the target through the reaction

$$X + e \rightarrow X^+ + 2e \tag{4.24}$$

Multiple ionization is also possible, provided that sufficient energy is imparted by the incoming electron.

In the case of molecules, it is also possible that the collision may result in dissociation. In this case, the molecule breaks up into one or more fragments through a process such as

$$AB + e \rightarrow A + B + e' \tag{4.25}$$

Both neutral and ionized fragments can be produced. The mechanisms of dissociation are discussed in detail in Section 4.2.4. Dissociative electron attachment is also possible. In this situation, the projectile becomes bound to the system and forms a negative ion upon dissociation through

$$AB + e \rightarrow A^- + B \tag{4.26}$$

4.2.2 Electron-Impact Excitation

When inelastic scattering results in excitation of the target, the routes of atomic and molecular excitation that are possible are heavily dependent on the impact energy[77, 80]. At high (hundreds of eV) and low ($< 50\,\text{eV}$) energies, the dominant excitations are optically allowed, electric dipole transitions. When considering intermediate energies of 20 eV to 100 eV, however, there can be a considerable number of optically forbidden excitations that

may also be permitted along with electric dipole processes. Exchange (or "spin-flip") collisions, where the projectile and a valence electron change places, may also occur at some energies, causing spin forbidden singlet-triplet mixing. In this section, we give a qualitative description of these excitation processes. The mathematical forms of their associated cross sections are given in Section 4.2.3. For a more in depth discussion of the topics covered in this section, the reader is encouraged to read the excellent review article by Hall and Read[80].

The source of the different regimes of electron-impact excitation is the degree to which the incoming electron perturbs the electric field of the target, quantified through the impact parameter (Section 4.1.1). The resulting time-dependent electric field can be considered[80] to be comprised of harmonic components across some spectral range. When considered from this perspective, the passing electron has the same effect as a time-dependent photon field comprised of photons spanning the same spectral range; hence, the electron can be considered to create a spectrum of virtual photons. Therefore, the types of interactions can be considered through this virtual photon spectrum via the multipole moments of the electromagnetic field created by the projectile/target system.

The effect of the impact parameter becomes evident when examining the multipole expansion[81] of the Coulomb potential between the electron and target

$$V(\mathbf{r}) = \frac{1}{4\pi\epsilon_o}\left[\frac{1}{r}\int d\tau' \rho(\mathbf{r}') + \frac{1}{r^2}\int d\tau'\ r' P_1(\cos\theta')\rho(\mathbf{r}') + \frac{1}{r^3}\int d\tau'\ (r')^2 P_2(\cos\theta')\rho(\mathbf{r}') + \ldots\right] \quad (4.27)$$

where $P_n(x)$ are the associated Legendre polynomials. The dominant excitations in a given energy regime can be understood by examining the most significant term in this series for a given separation between target and projectile.

When the impact parameter is large, the electron remains a large distance away from the target as it passes by. Therefore, the electric field remains relatively constant throughout the collision process, and as a result, the series in Equation 4.27 is dominated by the dipole term. This means optical dipole transitions become the most significant excitation mechanism for large impact parameters. Electric dipole transitions are also highly peaked in the forward direction[77], as for $\theta = 0$ the dipole term is also dominant.

At smaller impact parameters, but still at an approach distance which is on the same order as the size of the target, the incoming electron distorts the electric field to a much greater degree. At this point, other terms in the multipole begin to dominate and electric quadrupole transitions become more important so that at this range, optically forbidden transitions are much more likely to occur. These excitations are also enhanced[77] relative to electric dipole transitions at larger scattering angles.

When the electron approaches at very close distances it is possible for exchange collisions

to occur. In this type of collision, the projectile changes places with a valence electron in the target resulting in a change in the multiplicity of the target. This type of collision is predicated on the speed of the projectile being similar to that of the orbiting valence electrons and so is most likely to occur only over a very short energy range. However, it is also the only source of singlet-triplet mixing in electron collisions, as direct excitations such as magnetic excitation of spins are much weaker than the exchange process.

4.2.3 Inelastic Cross Sections for Fast Electrons

It was shown in Section 4.2.2 that there are several types of excitations which can occur during inelastic scattering of electrons. Optically allowed transitions, where states are connected by an electric dipole transition, are the most readily excited. Other types of inelastic scattering include exchange processes and spin-allowed but optically forbidden transitions. The cross sections from some of these processes can be described by Bethe-Born theory at high impact energies[82, 83]. When the cross section is plotted as a function of impact energy, in a so called "excitation function", each type of collision can be seen to have a different functional form in the energy dependence, which allows them to be readily differentiated. Below, expressions for the integral cross section for each of the aforementioned types of collisions are presented. These expressions apply to both atomic and molecular targets. For a more in depth discussion of the Bethe-Born theory applied to fast electron scattering, the reader is encouraged to read the review article by Inokuti[82].

One can arrive at the differential cross section for each type of inelastic scattering from the first Born approximation (Section 4.1.3) via the expression

$$\frac{d\sigma_n}{d\Omega} = \frac{\mu^2 c}{4\pi^2\hbar^4}\frac{k'}{k}\left|\int dK \int d\mathbf{r} \int d\mathbf{r}_1 d\mathbf{r}_2 \ldots d\mathbf{r}_Z \; e^{i(\mathbf{K}\cdot\mathbf{r})} \langle\psi_n(\mathbf{r}_j)|V|\psi_0(\mathbf{r}_j)\rangle\right|^2 \tag{4.28}$$

which is integrated over the angular frequencies of the momentum transfer $\mathbf{K}$, the projectile's position $\mathbf{r}$ and the positions of the target's internal electrons $\mathbf{r}_1, \mathbf{r}_2, \ldots, \mathbf{r}_Z$. The interaction potential V is given by the Coulomb potential

$$V = -\sum_{i=1}^{Z} \frac{ze^2}{|\mathbf{r} - \mathbf{r}_i|} + \frac{zZe^2}{r} \tag{4.29}$$

in terms of the nuclear charge number Z and the projectile charge number z. The factor z ensures that the expression is valid for electrons and positrons. By first integrating over the projectile co-ordinate, one can write this expression in a greatly reduced form as

$$\frac{d\sigma_n}{d\Omega} = 4z^2\left(\frac{\mu e^2}{\hbar^2}\right)^2 \frac{k'}{k}\frac{|\varepsilon_n(\mathbf{K})|^2}{K^4} \tag{4.30}$$

putting the cross section in terms of the momentum transfer $\mathbf{K} = \mathbf{k} - \mathbf{k}'$ and the term

$\varepsilon_n(\mathbf{K})$, which can be interpreted as the inelastic scattering form factor. This factor can be found using the expression

$$\varepsilon_n(\mathbf{K}) = \int d\mathbf{r}_1 d\mathbf{r}_2 \dots d\mathbf{r}_Z \left\langle \psi_n(\mathbf{r}_j) \left| \sum_{m=1}^{Z} e^{i(\mathbf{K}\cdot\mathbf{r_m})} \right| \psi_0(\mathbf{r}_j) \right\rangle \tag{4.31}$$

Rather than being dependent on the momentum transfer vector, this expression can be further reduced to a scalar equation under the assumption that the initial state $|\psi_0\rangle$ is either spherically symmetric or that the starting orientations of the target ensemble are randomly distributed. This is valid in most situations. As θ is related to the momentum transfer direction[82] and ϕ on the anisotropy of the target distribution, the conversion to a scalar equation eliminates all angular dependence from the scattering cross section. One can then write the scattering cross section in the form

$$\frac{d\sigma}{d(\ln Q)} = \frac{\pi z^2 e^4}{E_o} \frac{|\varepsilon_n(K)|^2}{Q} \tag{4.32}$$

in terms of the impact energy E_o, the projectile's charge z, and the quantity

$$Q = \frac{\hbar^2 K^2}{2m_e} \tag{4.33}$$

which has units of energy and is related to the magnitude of the momentum transfer K and the mass of the electron m_e.

Typically in atomic physics, one prefers to use the generalized oscillator strength rather than the inelastic scattering form factor. These two are related by the expression

$$f_n(K) = \frac{E_n}{Q}|\varepsilon_n(K)|^2 = \frac{E_n}{R_\infty K^2 a_o^2}|\varepsilon_n(K)|^2 \tag{4.34}$$

in terms of the change in momentum K, the transition energy E_n, the Rydberg constant R_∞, and the Bohr radius a_o. This expression is just the generalization of the optical oscillator strength

$$f_n = \frac{E_n}{R_\infty} M_n^2 \tag{4.35}$$

which is dependent on the square of the dipole matrix element

$$M_n^2 = \frac{1}{a_o^2} \left| \int \sum_{j=1}^{Z} \langle \psi_n | x_j | \psi_o \rangle \, d\mathbf{r}_1 \dots d\mathbf{r}_Z \right|^2 \tag{4.36}$$

where x_j is a component of $\mathbf{r}_j$. The generalized oscillator strength can be shown to be equal to the optical expression in the limit

$$\lim_{K\to 0} f_n(K) = f_n \tag{4.37}$$

Using this more convenient notation,the differential cross section can be written in the form

$$\frac{d\sigma}{d\left[\ln(Ka_o)^2\right]} = \frac{4\pi a_o^2 z^2}{E_o/R_\infty}\frac{f_n(K)}{E_n/R_\infty} \tag{4.38}$$

From this expression for the differential cross section, one can find the integrated cross section for a given transition by applying the formula

$$\sigma_n = \frac{4\pi a_o^2 z^2}{E_o/R_\infty}\int_{(Ka_o)^2_{min}}^{(Ka_o)^2_{min}} \frac{f_n(K)}{E_n/R}\frac{d(Ka_o)^2}{(Ka_o)^2} \tag{4.39}$$

integrated over all possible momentum transfer values. This general expression can be specialized for different classes of excitations and then expanded in an asymptotic series. The remainder of this section is dedicated to these series solutions.

For optically allowed transitions, we arrive at a solution of the form

$$\sigma_n = \frac{4\pi a_o^2 z^2}{E_o/R_\infty}\left[\frac{f_n}{E_n/R_\infty}\ln\left(\frac{4c_n E_o}{R}\right) + \mathcal{O}\left(\frac{E_n}{E_o}\right)\right] \tag{4.40}$$

which is dependent on the square of the dipole matrix element (4.36) or alternatively, the oscillator strength. The parameter c_n is an experimentally derived constant. One can find this constant[83] by making a plot of $\sigma_n E_o$ against $\ln E_o$, known as a Fano plot[82]. The slope of the line will be proportional to the oscillator strength f_n^{opt} while the constant c_n can be determined from the intercept of the line.

There are two important conclusions to draw from this expression. First, is that the energy dependence of optically allowed collision channels have a $(\ln E_o)/E_o$ dependence at high energies. Second, the electron impact cross section is related to the optical oscillator strength. Thus, if photon collision data is available for some optical channel, the corresponding electronic cross section can be determined from the Fano plot.

One can also derive an expression for optically forbidden but spin-allowed transitions. The asymptotic expansion has a similar form as that for optically allowed transitions and is given by the expression

$$\sigma_n = \frac{4\pi a_o^2 z^2}{E_o/R_\infty}\left[b_n + \frac{\gamma_n}{E_o/R_\infty} + \mathcal{O}\left(\frac{E_n^2}{E_o^2}\right)\right] \tag{4.41}$$

in terms of the parameters

$$b_n = \int_{-\infty}^{\infty} d\left[\ln\left(Ka_o\right)^2\right]\ \frac{f_n(K)}{E_n/R_\infty} \tag{4.42}$$

$$\gamma_n = -\frac{m}{2\mu}f_n - \frac{E_n}{4R_\infty}\ \frac{df_n(K)}{d(Ka_o)^2}\bigg|_{K=0} \tag{4.43}$$

However, since for optically forbidden transitions the asymptotic limit is $f_n = 0$, the cross

section reduces to approximately

$$\sigma_n = \frac{4\pi a_o^2 z^2}{E_o/R_\infty} b_n \tag{4.44}$$

which has an impact energy dependence of E_o^{-1}. From the functional form, one can see that the Fano plot of an optically forbidden transition should yield a flat line.

We can also consider exchange collisions. While this type of excitation is not explained by the Bethe-Born theory, the form of their cross sections is still well known[83]. Exchange interactions are sharply peaked at an energy where the impact velocity of the projectile is on the same order[77, 80] as that of the valence electrons of the target. At higher energies beyond this maximum, the cross section rapidly falls off as E_o^{-3}.

In conclusion, this section demonstrates that inelastic scattering cross sections have forms which demonstrate similar behaviour amongst collision processes that share a common underlying characteristic. As such, we can use the form of an observed relative cross section at higher energies to determine the class of collision process which may be occurring in a given experiment. Optically allowed channels take on a $(\ln E)/E$ dependence while those which are spin forbidden but optically allowed demonstrate a simple $1/E$ dependence at high energy. Those which are both optically and spin forbidden, where the projectile electron is exchanged in the collision, are sharply peaked at some lower energy and then fall off as $1/E^3$ at higher energies. As such, we can say quite a bit about the type of collisions which may be occurring a given experiment simply by studying their energy dependencies.

4.2.4 Dissociative Collisions

During electron scattering from molecules, the projectile may ionize the target by transferring sufficient energy for a single electron to be excited beyond its binding energy. It may also excite atomic constituents beyond their binding energies, resulting in dissociation of the molecule. Two common methods of dissociation can occur in electron collisions, depending on the final state to which the target is excited, namely: direct dissociation and pre-dissociation mechanisms.

In direct dissociation, the collision results in an excitation where one or more atoms are transferred to energy levels that lie beyond the dissociation limit, allowing it/them to escape the molecular potential. The channels by which dissociation occur are predominantly governed by the Franck-Condon principle (Section 3.7.2), with excitation occurring to areas of the molecular potential curve which overlap with the Franck-Condon region. If this region contains the inner repulsive part of the curve and lies above the dissociation limit, then breakup can occur.

A good illustration of the Franck-Condon principle applied to molecular dissociation can be found in Borst and Zipf's analysis[84] of the electron impact dissociation of O_2 and the production of $O(^5P)$. Figure 4.2 shows the potential energy curves of O_2 for the ground $X^3\Sigma_g^-$ state and two excited state curves. Upon excitation to the upper curve, the

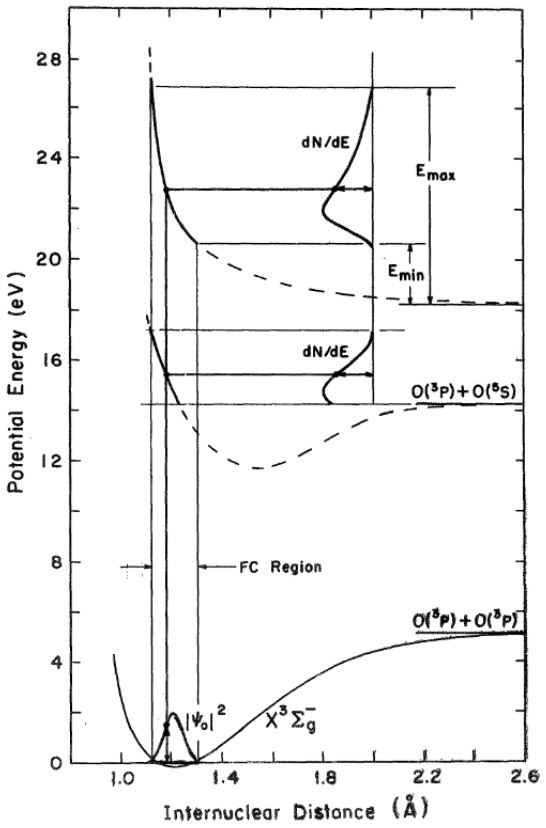

Figure 4.2: Molecular potential curves for O_2 for the ground and select excited states taken from Borst and Zipf[84]. Dissociation can occur from the upper states in the overlapping region above the dissociation limit. In the case of the repulsive state, the entire region results in dissociation. For the attractive potential, part of the region lies below the dissociation limit and if excitation occurs to this part of the curve, the molecule will remain bound rather than dissociate and will instead radiatively decay.

transition will occur to this repulsive state in the region shown which is within the Franck-Condon region of the ground state. The height above the dissociation limit will determine the released kinetic energy of the fragments.

In the second dissociation channel, the molecular potential of the state converging to the $O(^3P) + O(^5S)$ limit is attractive in nature, permitting a bound state. One will notice that now, the Frack-Condon region extends both above and below the dissociation limit. If the excitation occurs to the inner wall above 14 eV, dissociation can occur as the atom has energy in excess of the binding potential. However if on the other hand the excitation occurs to the part of the potential curve below 14 eV, the molecule remains bound and will radiatively decay to the ground state at a later time.

In the case of pre-dissociation, the molecule is initially excited to a bound state where the potential curve is attractive. If this state overlaps with a second repulsive curve, then it may be possible for the molecule to transfer to this second state on time scales faster than

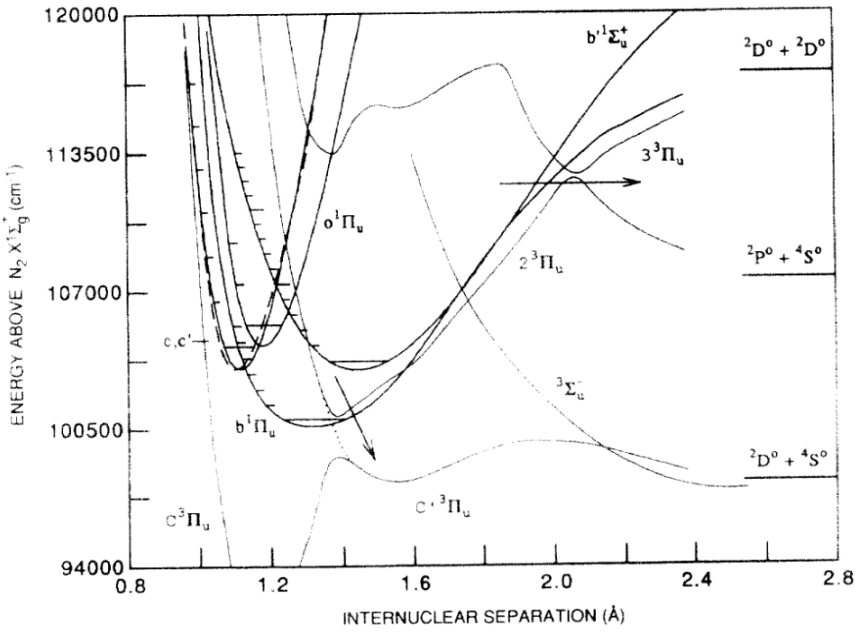

Figure 4.3: Molecular potential curves for N_2 taken from Walter *et al.*[86]. The arrows indicate pre-dissociation processes where there is overlap between the initial attractive state and the final repulsive state. The molecule will undergo a radiationless transition and dissociate.

those of radiative decay processes. The molecule will then pre-dissociate rather than emit a photon. Thus, pre-dissociation is different from the direct mechanism in that the excitation is first to a bound state rather than to a configuration lying above some dissociation limit.

One can understand the pre-dissociation process by considering electron impact of molecular N_2 where pre-dissociation plays a significant role in the dissociation dynamics[85, 86]. Molecular potential curves for the excited state of this system are shown in Figure 4.3, taken from the work of Walter *et al.*[86]. It can be seen that there is a region of overlap between the $b^1\Pi_u$ and $c'^3\Pi_u$ states. If the molecule transitions from the former deeply bound state to the latter, as shown by the arrow in Figure 4.3, its energy will be sufficiently high above the $^2D + {}^4S$ dissociation limit that a pre-dissociation process can occur. The same can be said of the $b'^1\Sigma_u^+$ state's transition to the $3^3\Pi_u$ state, also marked by an arrow.

4.2.5 Conclusion

In this chapter, electron scattering is presented both in a phenomenological and theoretical manner. The quantum treatment of scattering has been described by moving from the classical picture to the time-dependent Schrödinger equation and the various types of cross-section values which can be reported for scattering experiments are described. Electron impact phenomena are outlined and detailed theoretical forms are given for inelastic

scattering cross-sections. It was shown that the latter can be classified as optically allowed, spin-allowed but optically-forbidden, and spin-forbidden exchange collisions. Each class of scattering's cross-section has its own distinct mathematical form as a function of energy. Finally, dissociative collision are described phenomenologically with a special focus on direct and pre-dissociation mechanisms.

This work deals with various electron scattering experiments, with a focus on dissociative production of metastable species from molecular targets. As such, understanding how various dissociation processes occur and can be quantified is important. As the examination of the cross-section as a function of energy in these experiments is an integral component of the analysis, being able to classify the collision channel through the function form of this cross-section is an integral part of this work.

Chapter 5

Metastable Detector Setup

In this chapter, a description is given of the apparatus used in the subsequent experiments to detect metastable products of electron impact collisions. The entire setup is sealed in a vacuum chamber consisting of three stages. The first houses the electron collision chamber, containing the electron and target beams and associated monitoring hardware. This is connected to the detection chamber containing the gas matrix detector by a drift tube which is employed to differentiate the product by velocity, allowing for time-of-flight spectroscopy of the collision products. Additional counting hardware permits an alternative method for acquisition of photon counts as a function of energy to produce excitation functions, permitting a more in-depth analysis of the reaction.

Each of the following sections provide a detailed description a different portion of the system, including the vacuum chamber, the electron gun and associated hardware, the gas matrix detector, and the data acquisition hardware. In the final section, an overview of the different types of analysis methods used in this work are described as well as some of the mathematical details necessary to apply them to the data.

5.1 Vacuum Chamber

A schematic overview of experimental apparatus is shown in Figure 5.1. In the first chamber, electron impact of a target beam generates the metastable products. These then travel down a drift tube to another chamber containing the gas-matrix detection layer. When metastables impinge on this surface, they undergo some process (typically excimer formation) which results in de-excitation and the emission of a photon. This photon is then measured by a photo-multiplier tube (PMT), allowing detection of the metastable species.

The main collision chamber contains all of the equipment necessary to generate the metastable products through electron impact. This includes the electron gun assembly, Faraday cup detector, gas injector and vacuum pumps. The electron gun and Faraday cup assembly are described in detail in Section 5.2. The target gas was injected using a demagnetized stainless steel hypodermic needle 2.3 cm in length with an internal diameter

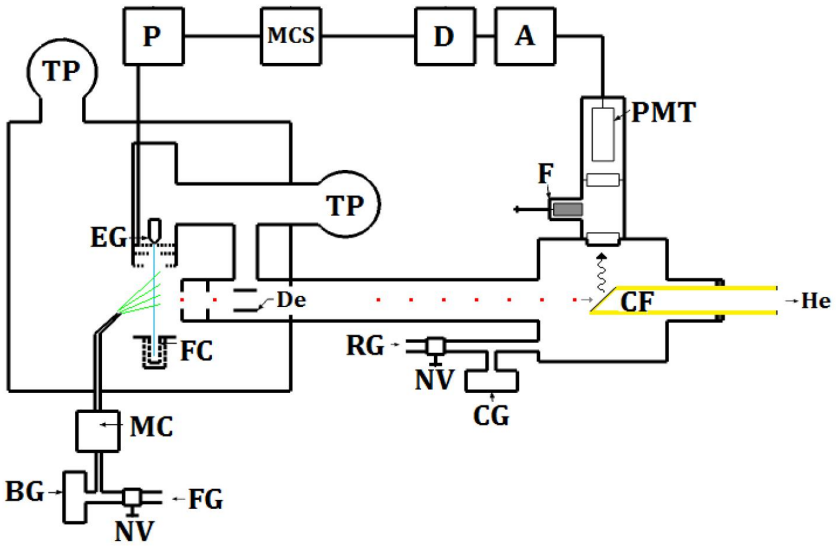

Figure 5.1: Diagram of the experimental apparatus. Shown are the amplifier, A; discriminator D; pulser, P; filter, F; turbopumps TP; electron gun, EG; microwave cavity, MC; Pirani gauge, BG; rare gas supply, RG; deflector plates, De; feed gas, FG; multichannel scaler, MCS; needle valve, NV; photomultiplier tube, PMT. Reproduced from Kedzierski *et al.*[45].

of 0.66 mm. The pressure upstream of the needle was monitored using a MKS Baratron gauge and regulated by a needle value.

Electron impact was typically performed in a crossed beam geometry with the target and electron beams aligned perpendicularly and mutually orthogonally to the drift tube. For dissociation experiments, this is the ideal configuration to allow fragments to travel towards the detector while minimizing collisional losses from the target beam. Alternatively, the injection nozzle could be rotated so that the target beam was injected collinear to the drift tube, allowing for the detection of metastable molecules. Rotation was necessary, as without collinear injection, the initial momentum of the target beam would prevent non-dissociated molecules from reaching the detector.

Differential pumping of the main chamber was also critical to achieving a functioning system. As the target gas was constantly injected into the chamber, the electron cathode was continually exposed to relatively high levels of potentially damaging gases. In initial experiments by Corr[48], the cathode was directly exposed to the O_2 target beam and lasted only about 8 h, motivating the current design where the electron gun housing and drift tube are separately pumped from the main chamber. The introduction of differential pumping prolonged the lifetime of the cathode to months rather than hours and reduced the possibility of in-flight collisional loses of metastables in the drift tube. Pumping was performed with two Varian TV 701 turbo-molecular pumps with pumping speeds of 690 L/s. The use of turbo pumps also created an oil free environment, preventing additional contaminants

from accruing on the electron gun or detector surfaces. Before gas injection, these pumps were capable of maintaining a background pressure of 2×10^{-7} torr, which then rose to around 10^{-4} torr to 10^{-5} torr after gas injection.

After metastables were generated in the main chamber, they would then travel down a 26 cm drift tube towards the detector. Quench plates within this area could be activated to generate an electric field capable of quenching Rydbergs, which was useful for checking that such particles were not present in the detected signal. A plexiglass shutter not shown in Figure 5.1 within the drift tube could also be closed, preventing metastables from reaching the detector but still permitting the detection of optical excitations generated in the initial electron pulse. This was useful in separating the prompt and metastable signals in the case of overlap. Once metastables passed through the drift tube, they would arrive at the detector surface. The details of the construction and operation of the detection region are fully described in Section 5.3.

5.2 Electron Gun

The electron gun system consists of the electron gun assembly and a Faraday cup for current monitoring. A schematic of the electron gun assembly can be seen in Figure 5.2. A Thoriated Iridium cathode was used rather than a conventional Tungsten one. The reason for this is that the former is far more resistant to the harsh environment used in these experiments, including constant exposure to relatively high levels of atmospheric gases and higher chamber pressures that what are optimal for Tungsten cathodes. The choice of cathode combined with differential pumping of the electron gun housing (Section 5.1) were both critical in prolonging the life of the cathode.

Before entering the collision region, the electron beam was shaped by a series of lensing electrodes which allowed for collimation and focusing of the output. The emission current profile as a function of extraction voltage is shown in Figure 5.3 and can be seen to be relatively constant over much of the energy range of the gun. A final gating electrode permitted the electron beam to be pulsed by selectively applying a negative voltage, acting as a grid to prevent the flow of electrons into the collision region.

Magnetic focusing after the final electrode was employed to ensure the beam had a constant cross-sectional area and emission current[51] across a wide energy range. The field was generated by four 1.5 cm diameter, 15 cm long Alnico-V magnetic rods arranged in a quadrupole configuration as shown in the inset of Figure 5.2. The rods were oriented with like poles at the same end. The design also provided another advantage - the open area around the emission aperture permitted free passage of neutral fragments toward the detection chamber while the magnetic field exerted a force on any charged particles created in the collision region, deflecting them from the detector and providing discrimination against ions in the final signal.

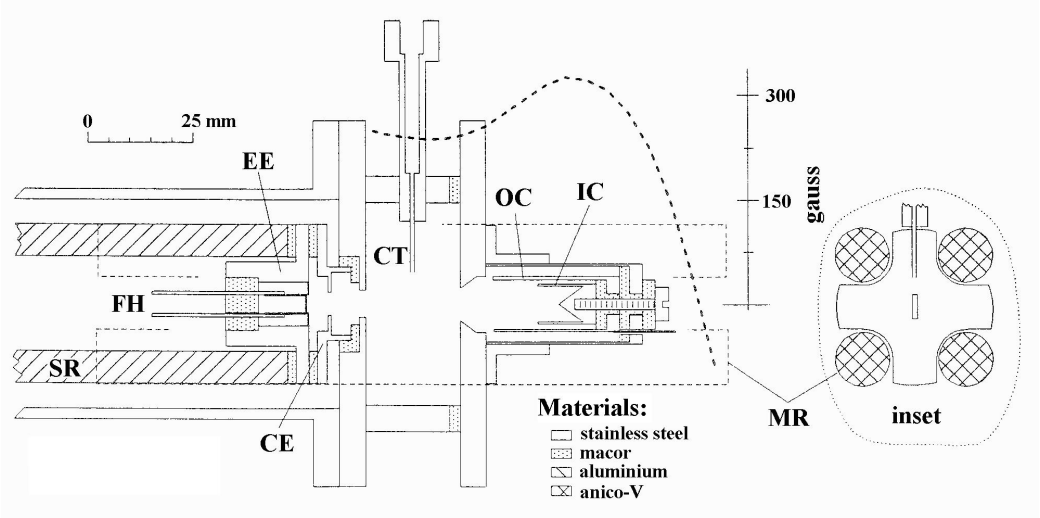

Figure 5.2: Schematic of the electron gun assembly. Shown are the support rods, SR; filament holder, FH; extraction electrode, EE; collimation electrode, CE; gas inlet capillary tube, CT; inner Faraday cup, IC; outer Faraday cup, OC; magnetic rods, MR. In the left schematic the magnetic rods are denoted with a dashed line, showing their orientation with respect to the electrodes and the slit to the gas inlet. A heavy dashed line at the top of the diagram shows the magnitude of the magnetic field, according to the scale on the right. Reproduced from LeClair *et al.*[52].

During the electron beam pulse, a continuous stream of optical excitations were generated in the collision region. This flux of photons would partially reflect off the detector face and arrive as a prompt pulse (see Figure 5.5) which served as an excellent marker of the start of the TOF spectrum. However, the constant glow of the hot cathode was also a source of background radiation throughout the spectrum but could be removed through a constant subtraction in post-processing.

To measure the emission current, the electron beam was collected by a double Faraday cup placed 7.3 cm away from the electron gun filament. The majority of the current (>99%) entered the inner cup (11 mm long and 9.4 mm diameter) which was held at a +20 V bias relative to ground. The beam was collimated by a 7.6 mm aperture before entering the cup, which was maintained at ground.

5.3 Gas-Matrix Detector

The heart of the apparatus is the gas matrix which induces the de-excitation of the metastables, permitting their detection upon radiation of a photon. This layer is formed by depositing a gas, typically a noble one, onto the surface of a cold finger. Usually, the de-excitation mechanism relies on the formation of an excimer on the layer surface. This is the case for rare gas matrices[51] and other solid layers when reacting with metastable atoms but it is also possible for molecular de-excitation to occur through other energy transfer mechanisms[63].

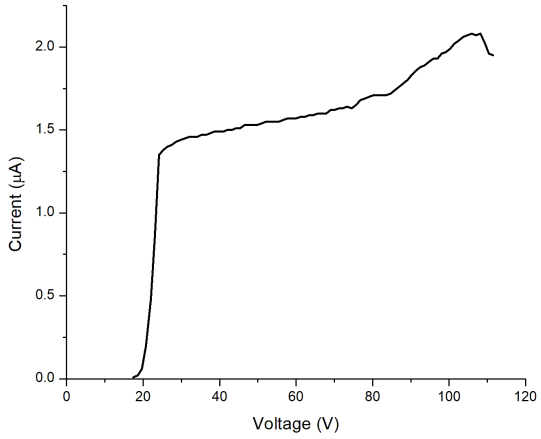

Figure 5.3: Integrated electron current measured by the inner Faraday cup as a function of extraction voltage. Electron pulses were 27 µs long with a repetition rate of 1 kHz.

Solid rare gas layers have been demonstrated to be effective[51] in detecting emission from metastables originating from atoms with a np^4 ground state configuration such as $O(^1S)$, $O(^1D)$ and $S(^1S)$ as well as other atomic and molecular states such as $CO(a^3\Pi)$. Other gases such as N_2 have also been shown[63] to be effective in detecting some of these states as well.

An illustrative example of the excimer formation process is the case of $O(^1S)$ reacting with a solid Xe layer to produce XeO. The potential energy curves for this system are shown in Figure 5.4. As the $O(^1S)$ atom approaches the surface, it binds with Xe in the $2^1\Sigma^+$ state. It can then transition to either the inner repulsive wall of the $^1\Pi$ state, or into the bound $1^1\Sigma^+$ state which radiate in the near IR or ultraviolet respectively. The lifetime of the excimer is around 20 ns[51] while the lifetime of the bare $O(^1S)$ atom in the gas phase is around 0.8 s[18]. A similar process has been observed to occur in other solid layers including other rare gases[51], and N_2[63].

The solid gas layer was formed on a solid copper cold finger (2.5 mm diameter) typically cooled to 18 K to 25 K and this temperature was maintained by a Advanced Research Systems ARS-4HW helium cryostat regulated by a Lakehead 331 Temperature Controller. The cold finger was mirror polished and nickel plated before installation. In order to deflect photons towards the PMT, the face of the cold finger was cut at a 45° angle relative to both the drift tube and the line of sight of the PMT which themselves are perpendicular to each other (see Figure 5.1). While vacuum in the collision chamber and drift tube were maintained by turbo-pumps, additional pumping of the detection chamber was not needed as the cold finger acted as an effective cryopump for maintaining vacuum in this region.

In order to form the layer, gas was flowed over the face of the cold finger, freezing on the surface. Gas injection was controlled by a needle valve upstream of the nozzle and monitored

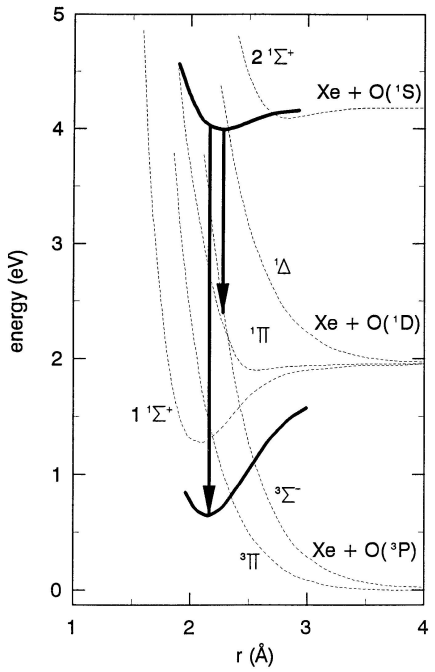

Figure 5.4: Molecular potential curves for the XeO system. The dashed lines represent curves taken from Dunning and Hey[50] and Simmons *et al.*[29] while the solid lines are from Lawrence and Apkarian[44]. The diagram is reproduced from McConkey and Kedzierski[51].

by a Pirani gauge. Injection was performed throughout an experimental run in order to continuously refresh the frozen layer. This was necessary as interactions between the surface and residual target and background gases around the layer would degrade the surface over time. After prolonged data acquisition, thickening of the frozen layer would cause a drop in sensitivity as the surface temperature would increase with increasing distance from the cold finger surface. To mitigate this effect, the layer was boiled off from time to time and re-deposited in order to maintain a working sensitivity.

Detection of the photons emitted from the surface was performed with a Hamamatsu R649 photo-multiplier tube (PMT) with a borosilicate glass window capable of detecting photons in the 300 nm to 850 nm range. The unit was cooled to reduce thermal electrons from the photocathode and PMT using a C10372 thermoelectric cooler. A plexiglass light pipe was placed between the cold finger and PMT in order to increase the solid angle of detection and boost signal levels. Bandpass filters could also be inserted between the light pipe and the PMT to isolate a particular spectral region of interest in any given experiment.

5.4 DAQ System

All time sequenced elements of the system such as the pulsed electron beam and data acquisition (DAQ) modules were controlled by a master oscillator operating typically at

frequencies of about 1 kHz. Control pulses delayed from this master trigger would then activate each individual element. In all experiments, data was acquired by measuring pulses from the PMT corresponding to photons generated at the detector surface. These were first processed by shaping and discrimination electronics before being registered. Two different methods of acquisition were employed either using a multi-channel scaler (MCS) or dual-gated photon counter which could be used for two separate types of photon counting studies.

The signal conditioning chain can be seen in Figure 5.1. Pulses from the PMT were first amplified by an Ortec 474 Timing Filter Amplifier. An Ortec 584 Constant-Fraction Discriminator then discriminated the pulses against noise, generating a fast TTL pulse which was then registered with the counting hardware. Acquisition was performed with either a SR430 multi-channel analyzer or SR400 dual gated photon counter, both by Stanford Research Systems.

5.5 Analysis Methods

When examining metastable collision data there are generally two methods which provide the most relevant information for examining the scattering process. One could measure the time-of-flight spectrum for the arrival of metastables at the detector surface for a fixed impact energy or examine the signal appearing in a given time window while varying the energy to produce an excitation function. Both of these methods were used extensively and are discussed in detail below.

5.5.1 Time-of-Flight Spectroscopy

One method of analysing the metastable products of a collision experiment is through time-of-flight (TOF) spectroscopy. As these are massive particles, there is a measurable time delay (usually tens or hundreds of microseconds) between their excitation by the electron beam and their arrival and subsequent de-excitation at the detector surface. This time delay allowed for a clear separation from the prompt photons produced by electric dipole excitations and metastable particles of differing energies.

To acquire a TOF spectrum, one could use the MCS to count the photons referenced from the start of the scan based on a pulse from the master oscillator. An example of this type of spectrum is shown in Figure 5.5. There are a few features in this scan to be noted. First is the “prompt photon” signal which corresponds to optical excitations in the collision region and are produced throughout the duration of the electron pulse. This prompt feature also acted as a marker for the beginning of the scan during analysis and could also be used in some situations as an internal calibration to normalize between different data sets. A peak or series of peaks (“metastable feature(s)”) in later time bins would also be observed corresponding to the metastables reaching the detector and radiating with arrival times based on their energies.

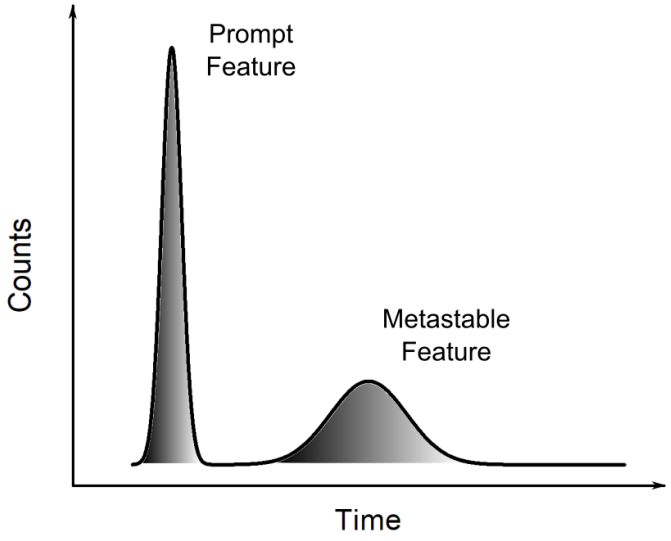

Figure 5.5: Diagram of a typical time-of-flight (TOF) spectrum. Some time after the initial burst of prompt photons excited by the electron gun, metastable products impinge on the detector surface radiating photons.

As the drift tube is of fixed length, the time taken to travel the drift region is directly related to the metastable particle's velocity v or equivalently its kinetic energy $E = (1/2)mv^2$. Thus, it is possible to also form an energy spectrum of the arriving metastables from the TOF distribution. A simple transform exists relating the TOF distribution $F(t)$ and energy distribution $F(E)$ given by

$$F(E) = \frac{t^3}{mD^2}\, F(t) \tag{5.1}$$

in terms of the drift tube length D and the mass of the particle m. The derivation of this transform is outlined in Appendix B.2 and further details can be found in Smyth *et al.*[87]. The time and energy distributions can be useful in emphasizing different parts of the metastable spectrum. An example of the markedly different behaviours in the time and energy domain of a spectrum can be seen in Figure 5.6.

As the electron pulse has a finite width, excitations are produced throughout the pulse length. This can cause a "smearing" of the TOF distribution, broadening the metastable features. For a pulse of width Δt, the energy spectrum has a corresponding broadening of

$$\frac{\Delta E}{E} = \frac{2\Delta t}{t} \tag{5.2}$$

A derivation of this relationship is given in Appendix B.2. Ideally, one would like to work with the shortest electron pulse possible to resolve all of the metastable features in a given

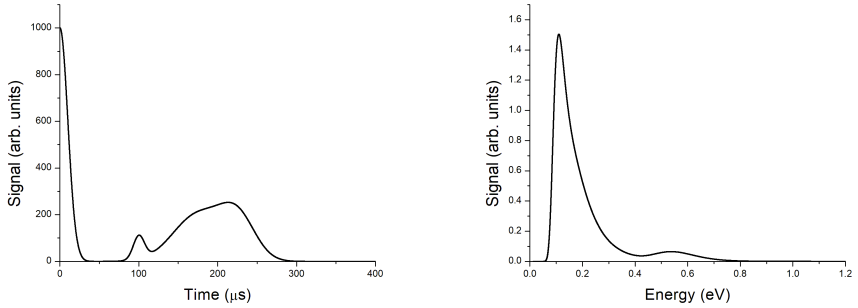

(a) TOF Spectrum (b) Energy Spectrum

Figure 5.6: Demonstration of the time to energy spectrum transform applied to a mock TOF distribution. On the left is the spectrum in the time domain while the plot on the right shows the same distribution transformed into the energy domain. The spectra are markedly different in shape and as such can each be used to emphasize different parts of the distribution.

spectrum but this comes at the cost of reduced signal. As such, there is often a trade-off between the best resolution and high signal-to-noise ratios.

5.5.2 Excitation Functions

One can also examine the cross-section for various metastable products as a function of energy in an *excitation function*. This type of analysis is particularly useful for determining the onset of an excitation channel and identifying the class of excitation through examination of its behaviour over the energy range (Section 4.2.3).

To acquire an excitation function, one can employ a dual-gated photon counter. Two time windows can be established relative to the start of the electron pulse which count the total number of photons arriving within a given time window. It is then possible to simultaneously measure the photons arriving during the prompt photon peak and those in a time window corresponding to one or more metastable features. One can then acquire relative cross sections for the prompt and metastable features while varying the electron impact energy, producing excitation functions for both features. To aid in the automation of this type of acquisition, this work used a program developed by Jeff Hein to automatically configure the photon counter to set up these windows, acquire the photon counts across a desired energy range, and save the individual spectra to disk for further analysis.

Acquiring both the prompt photon and metastable excitation functions simultaneously is often useful for forming an internal energy calibration. As the optical excitation channels in a given collision process are usually well studied in comparison to metastable production, one can look to previous studies to determine energy onsets of these electric dipole channels to fix the impact energy and account for any shifts to the electron energy within the system.

In some serendipitous situations, one may also be able to determine the absolute cross

section for an optically allowed metastable production channel if there is a single or vastly dominant optical excitation in the prompt photon window. If data on the oscillator strength of the metastable feature is available from photodissociation data, one can apply the Born-Bethe theory (Section 4.2.3) to derive the absolute cross-section value.

5.5.3 Data Smoothing

Due to the low signal-to-noise ratios inherent in studies of low probability collision events, combined with the constant background from the hot cathode, there tends to be a great deal of channel-to-channel noise in both the TOF spectra and excitation functions. In order to have a better understanding of the underlying structure of the data, it is often useful to applying smoothing. While adjacent averaging can be employed, more sophisticated methods can also be used to remove noise while distorting the signal tendency as little as possible. One such method is Savitzky-Golay filtering[88].

In this method, successive subsets of adjacent data points are fit with an N-degree polynomial, typically a second or third order one, using least-squares fitting. One can use this method if the data consists of n evenly spaced points (x_i, y_i) for $i = 1, \ldots, n$, where x_i and y_i are the independent and dependent variables respectively. At each point, a change of variable is made

$$z = \frac{x - \bar{x}}{\Delta x} \tag{5.3}$$

where $\bar{x}$ is the central point of the window. The N-degree polynomial is then fit

$$Y = \sum_{k=0}^{N} a_i z^k \tag{5.4}$$

and the smoothed value at the point x_i corresponds to the value of this function at $z = 0$ (*ie.*, a_0).

Chapter 6

Metastable Detection with Alternative Solid Layers

When using solid layers as a detection medium for metastables, one often works with the rare gases xenon and neon, which have different advantages. Xenon has been shown to have a high sensitivity[45] to metastables and higher freezing point relative to other rare gases but often has large red shifts of the excimer radiation relative to the natural wavelengths of the gas phase transitions. This can be problematic in some scenarios as this can shift the radiation out of the visible spectrum and far into the infrared, preventing standard PMTs from detecting the photons. Neon can be used[51] in situations where lower lying states are being examined as less red shifting tends to occur and photon wavelengths are often much closer to those of the natural transitions. States such as $O(^1D)$ are then visible to standard photomultiplier tubes when forming NeO^* excimers. However, high purity samples of these gases are costly and so there is a financial motivation to find less expensive alternatives if possible. This is further compounded by the costs and equipment associated with cooling rare gas layers. While xenon can be frozen[89] at 161 K using liquid nitrogen, neon freezes out at 24 K and requires the use of specialized helium compressors to operate. As such, finding gases which freeze at higher temperatures can bring in added cost savings and widen the applicability of the technology.

Studies by Schoen and Broida[32] and then later by Kedzierski and McConkey[63] have demonstrated that solid N_2 layers are also sensitive to $O(^1S)$ and metastable N_2 states. This suggests that other frozen layers may also be sensitive to certain metastable species and could be used as alternatives to rare gas layers. The lower costs typically associated with atmospheric and easily produced gases further motivates these studies. The use of such layers could also open up possibilities for this technology to be applied directly in the upper atmosphere and beyond as removing the need for deep cooling makes the detection of metastables much easier when such a device is placed on a satellite.

There are also a number of astrophysical motivations for studies of metastable inter-

actions with these frozen layers. It is well known[7, 90–92] that metastable atomic and molecular states can play important roles in the interactions with a variety of ices formed from atmospheric gases. As such, understanding the physical and chemical interactions is of considerable interest.

In this chapter, the use of solid CO_2 and N_2O layers for detection of metastable species are examined and characterized. A summary of other relevant investigations is also provided to put this work into context of previous studies. In the closing section, a review of all solid layers which are known to be sensitive to various metastable species is presented to act as a guide for future experiments where a specific metastable species of interest is being examined.

6.1 N_2 Layers

Some of the earliest studies of the interactions between metastable states and frozen gas layers began with studies of solid N_2. As a great deal of work has already been performed on these layers, here, only a summary is provided for completeness. Beginning in the mid 1950s, Broida and Pellam[93] observed phosphorescence after electron bombardment of solid nitrogen layers frozen at 4.2 K, attributing the signal to atomic nitrogen embedded in the surface. Further studies by Broida's group revealed that these layers were also sensitive to metastable NO and $O(^1S)$ produced in electron dissociation of N_2O[94] and O_2[95]. Measurements of the $O(^1S)$ excimer[63] have determined the emission wavelength to be in the green near 560 nm with a radiative lifetime of approximately $14 \pm 2\,\mu s$.

Solid nitrogen layers have also been found to be sensitive to metastable N_2 molecules. Kedzierski and McConkey[63, 64] were able to observe fluorescence from both the $a^1\Pi_g$ and $^1\Gamma_g^+$ states after electron-impact excitation. For these molecules, it has been proposed that a different de-excitation mechanism is responsible for the decay of these metastable states[63]. Rather than forming an excimer which radiatively decays, as occurs with metastable atomic fragments, it has been proposed that an energy transfer process occurs at the surface which converts these metastables into an intermediate state that has an optically allowed decay channel.

6.2 CO_2 Layers

There are a number of appealing features in using CO_2 as a detection layer, including its cost effectiveness, high freezing point, and its prevalence in Earth's atmosphere and extra-terrestrial environments. Compared to rare gases, it comprises a very large percentage of our atmosphere and is a common product of combustion, making it easier to obtain at economical prices. It also freezes[89] at a much higher temperature of 216 K, making production of a solid layer much easier than for any of the rare gases. This opens the possibility

that metastable detection could be performed at temperatures above those obtainable with liquid He or N_2.

Carbon dioxide is also prevalent in astrophysical environments such as comets and interstellar media. For example, interactions between $O(^1D)$ and CO_2 have been found to play an important role in the Martian atmosphere[90–92] and in comet systems[7].

In this section, measurements of both metastable atomic oxygen and molecular nitrogen are described. The solid layer is also characterized to determine the excimer's radiative lifetime, the reaction mechanism occurring at the surface, and its temperature dependent sensitivity.

6.2.1 Detection of Metastable Oxygen

In order to determine the suitability of solid CO_2 to detect metastable atomic oxygen, measurements of electron-impact dissociation of CO_2 at 65 eV were performed - a process known[51, 56] to be a strong source of both $O(^1S)$ and $O(^1D)$. Emission from the surface was found to occur in both the green near 550 nm and in the red. Both TOF spectra are shown in Figure 6.1, and comparisons are made to those measured for $O(^1S)$ using a Xe layer[56] and $O(^1D)$ with Ne[62]. The shapes and arrival times of the metastable fragments are consistent with those previously observed, suggesting that the present green emission corresponds to $O(^1S)$ while that in the red corresponds to $O(^1D)$.

The CO_2 layer was seen to have a delayed emission relative to solid Xe. One can model this by convolving the response of the xenon layer and an exponential decay term to account for the differences in lifetimes. The XeO^* excimer is known to have a lifetime[51] of 20 ns, which can be considered to be negligible on the time scale of the spectra in Figure 6.1. If one wishes to relate the time evolution of the response of the CO_2 layer, $f_{CO_2}(t)$, to that of xenon, $f_{Xe}(t)$, where the two layers have a difference in lifetimes, τ, this corresponds to the equation

$$f_{CO_2}(t) = \int_0^\tau dt' \; f_{Xe}(t') e^{-(t-t')/\tau} \tag{6.1}$$

The data was fit using the non-linear curve fitting algorithm provided in the SciPy Python package. Using the Xe reference data shown in Figure 6.1a, this model accurately fits the $O(^1S)$ spectrum if a lifetime of 7 ± 5 µs is assumed (see Figure 6.2). It was not possible to determine the lifetime of the corresponding $O(^1D)$ state as there was no available TOF spectrum for this state on a rare gas matrix using the same electron pulse width.

One can also speculate as to the chemistry occurring at the detector surface which gives rise to the observed emissions. One possibility is that atomic oxygen is reacting with the CO_2 ice to form CO_3 which then subsequently radiates. The formation of CO_3 from a $O(^1D)$+CO_2 reaction is well known[96–102]. Theoretical studies by Mebel *et al.*[101] provide a possible reaction pathway which would explain the red photon emission observed from $O(^1D)$ in the present experiment.

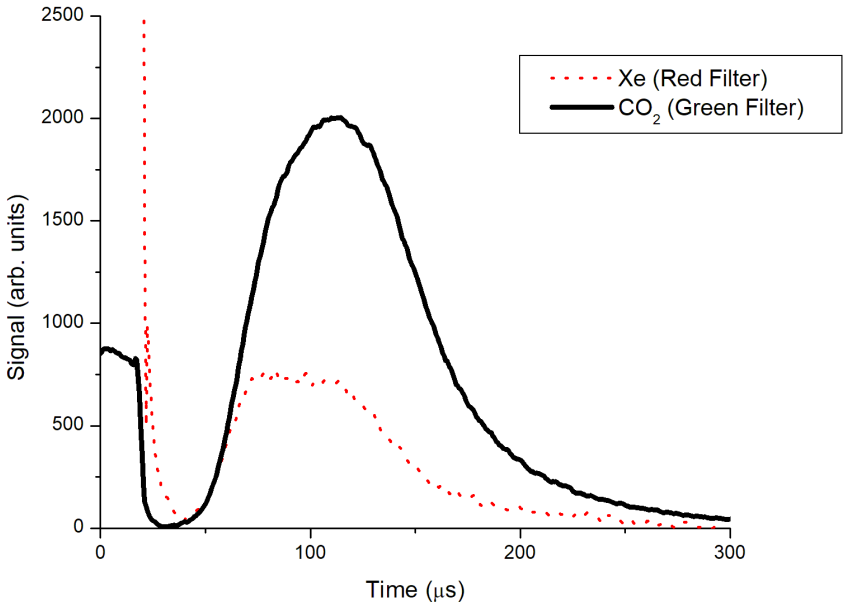

(a) O(^{1}S) with green filter applied for CO_2

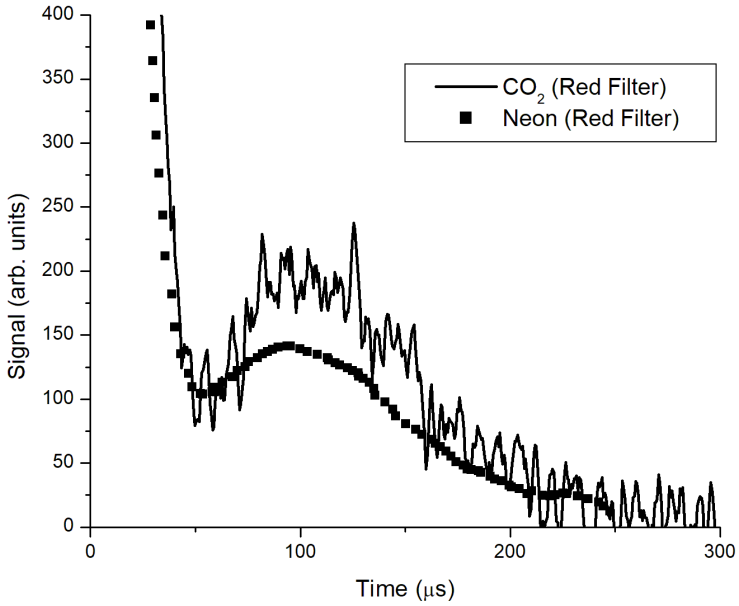

(b) O(^{1}D) with red filter applied for CO_2

Figure 6.1: Emission spectra acquired for both O(^{1}S) and O(^{1}D) from electron-impact of CO_2 at 65 eV using a 27 µs wide electron pulse are shown in 6.1a and 6.1b respectively. The spectra acquired from CO_2 are shown in solid black with constant background subtraction and Savitzky-Golay filtering[88] applied to both. In each figure, a reference scan taken using a solid rare gas layer is also shown. In 6.1a, a TOF spectrum with xenon at 100 eV and a 27 µs pulse width is shown. For 6.1b, a spectrum obtained using neon is shown. The data was taken from Kedzierski and McConkey[62] and acquired at 100 eV impact energy and a 20 µs pulse width. While the impact energy differs between the scans, the spectra are sufficiently comparable to allow for differentiation of the fragment species.

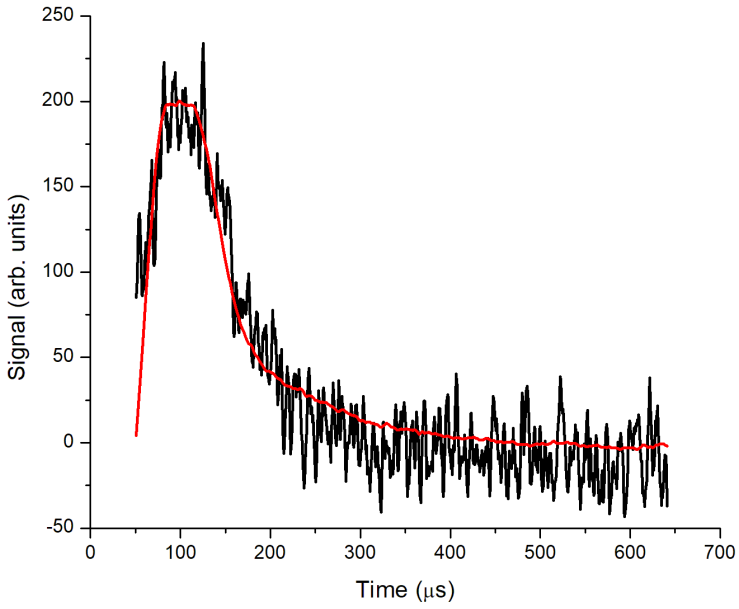

Figure 6.2: TOF spectrum of O(^{1}S) on a CO_2 layer. The fitted line shows the response of the detector assuming a 7 ± 5 µs lifetime for the excimer on the detector surface based on the xenon data in Figure 6.1a.

The process is outlined in Figure 6.3. First, the approaching O(^{1}D) reacts with the CO_2 present on the surface, forming a weakly bound CO_3 complex. This subsequently isomerizes to a transition state at a slightly higher energy which radiatively decays at 697 nm to form a C_{2v}-symmetric three-member cyclic structure. This reaction pathway is possible due to the incoming kinetic energy of the O(^{1}D) atom[101]. Thus, the process follows the reaction pathway

$$CO_2 + O(^1D) \rightarrow CO_3(C_{2\nu},^1 A_1) \rightarrow CO_3(C_s,^1 A') \rightarrow CO_3(C_{2\nu},^1 A_1) + h\nu \ (697\,\text{nm}) \quad (6.2)$$

A secondary process may also occur[100] which causes the final state of Equation 6.2 to dissociate to O(^{3}P) + CO_2 through a phonon interaction with the surrounding CO_2 ice involving singlet-triplet mixing with other intermediary CO_3 states. However, the present apparatus has no method of detecting this dissociation process.

To the author's knowledge, there are no comparable studies for the O(^{1}S) + CO_2 reaction. This is likely due to the fact that much of the experimental work was performed by producing O(^{1}D) through photolysis[96, 97], in which case generating O(^{1}S) is not energetically feasible with the Mercury flash lamps used in these studies. While other studies[100] generated CO_3 via electron impact excitation of oxygen where O(^{1}S) could be created, these studies examined only the vibrational excitations of CO_3 states near the O(^{3}P) + CO_2 dis-

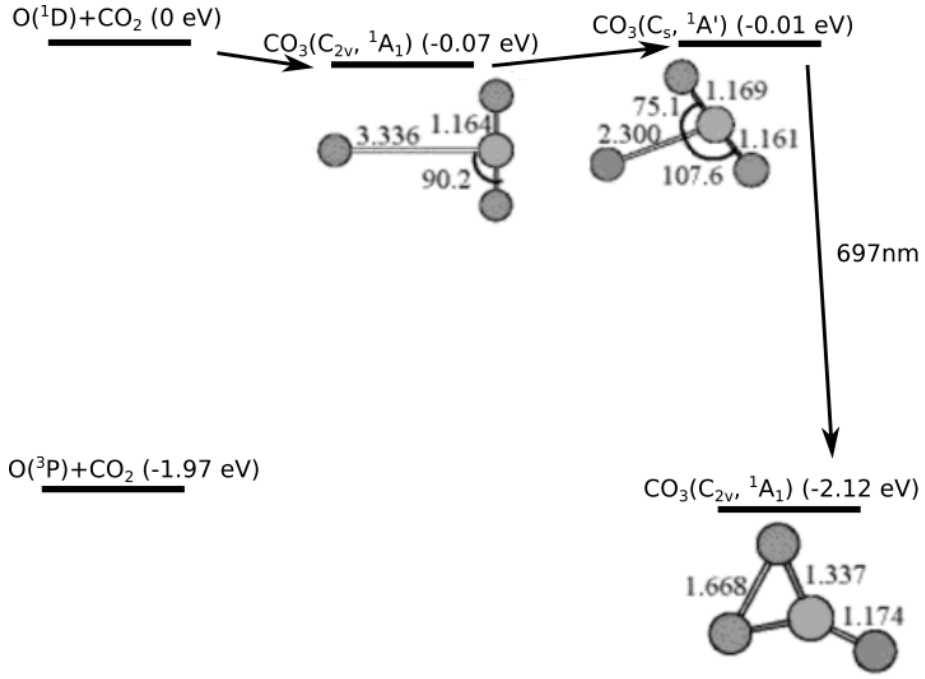

Figure 6.3: Diagram of the CO_3 isomerization process occurring at the detector surface adapted from Mebel *et al.*[101], including their calculated bond lengths and angles. The $O(^1D) + CO_2$ reaction forms a weakly bound CO_3 complex that then isomerizes through an intermediary state to a three-member cyclic structure, radiating at 697 nm in the process. The molecular diagrams for each stage indicate the bond lengths in Angstroms and the angles between the constituent atoms. The energy of each state relative to the $O(^1D) + CO_2$ dissociation limit is shown.

sociation limit using infrared spectroscopy. Without measurements of photons in the visible spectrum, it would be unlikely that these groups could isolate a signal generated by $O(^1S)$. Based on the measurements of the lifetime of the state at the detector surface, the time for the system to bind to form CO_3 and then radiatively decay is $7 \pm 5\,\mu s$. This reaction could follow a similar process to Equation (6.2) where some complex is formed which either isomerizes through a process such as

$$CO_2 + O(^1S) \rightarrow CO_3^* \rightarrow CO_3'^* + h\nu \text{ (green)} \tag{6.3}$$

where the green photon emission occurs through some intermediary CO_3 complex or by some excimer formation process such as

$$CO_2 + O(^1S) \rightarrow CO_3^* \rightarrow O(^3P) + CO_2 + h\nu \text{ (green)} \tag{6.4}$$

Quantum chemistry calculations would be necessary in order to determine any possible channels through which this reaction could occur.

Unfortunately, such computations are non-trivial. The corresponding $O(^1D) + CO_2$ calculations were performed[101] using the multireference complete active space self-consistent field (CASSCF) method which involves extremely large basis sets and heavy computational resources. Calculations of the $O(^1S) + CO_2$ reaction would need to be carried out at the same level of accuracy in order to determine the appropriate transition states between the initial and final products.

There are also arguments against this reaction pathways. In the case of $O(^1D) + CO_2$, the radiative $CO_3(C_s, ^1A') \rightarrow CO_3(C_{2\nu}, ^1A_1)$ transition involves a change of symmetry. This implies that any radiative transition would be rather weak. The TOF spectra of Figure 6.1 are both relative measurements which make comparing the actual strength of the emission from the CO_2 surface difficult. To make such a calibration would require accurate measurements of the electron and target beam densities. The wavelength of emission would also need to be accurately determined in order to account for the quantum efficiency of the PMT at this wavelength for such a calculation. As such, quantifying the absolute conversion efficiency of the detection layer is non-trivial.

Another possibility is that the reaction at the surface involves the formation of carbonate ions (CO_3^{2-}). Production of this ion is known[103] to occur between CO_2 and O. However, to the author's knowledge, information regarding its formation from the ^1D or ^1S states is unavailable. If the transition states of this ion preserve symmetry, then any optical decays to the ground state would certainly dominate the weaker radiation from the neutral process described above. However, additional theoretical or experimental investigation of the ion formation from metastable oxygen would be required to assess the viability of this reaction further.

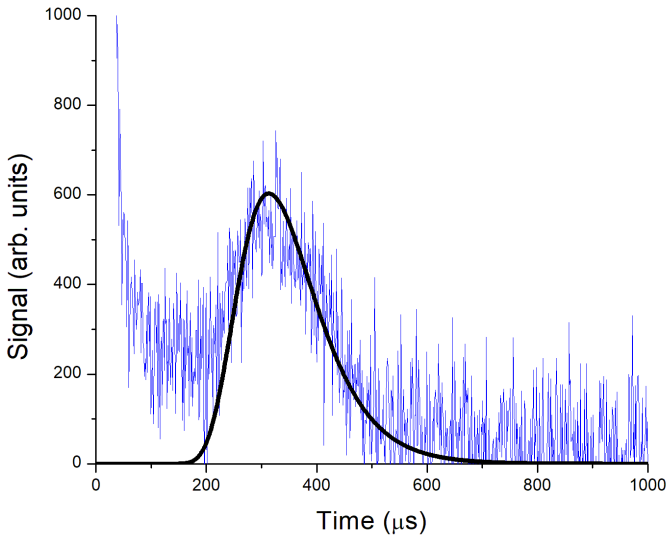

Figure 6.4: Observed TOF signal originating from $N_2(a^1\Pi_g)$ impacting on a solid CO_2 layer with constant background subtraction applied. The solid line indicates the fitted decaying Maxwell-Boltzmann distribution assuming a temperature of 292 K and lifetime of 80 µs. The lifetime of the state is consistent with that of $N_2(a^1\Pi_g)$[64, 104].

6.2.2 Detection of Metastable N_2

Solid CO_2 was also found to be sensitive to metastable states of N_2. Electron-impact of N_2 was performed at 100 eV using a 27 µs electron pulse width. The TOF spectrum measured with no filter applied to the PMT is shown in Figure 6.4. As the signal was only observed for gas injection parallel to the the drift tube, it can be concluded that the signal originates from metastable molecular rather than dissociated atomic states.

The detected molecules likely belong to the set of states measured with solid N_2 layers by Kedzierksi and McConkey[63, 64]. As the $a^1\Pi_g$ and $^1\Gamma_g^+$ states have drastically different lifetimes, one can use fitting techniques to determine which states the present CO_2 layer is sensitive to based on in-flight decay rates.

As the surface is detecting metastable molecular rather than atomic states, one can assume that the particles are travelling with a Maxwell-Boltzmann distribution of speeds. Momentum transfer from the electron beam can be assumed to have a negligible effect on the molecules due to the electron and target beam configuration. If in flight radiative decay is occurring, one can model the measured signal distribution as a Maxwell-Boltzmannn time-of-flight distribution (Appendix B.3) with a decay parameter corresponding to the expression

$$F(t) = f_{MB}(t)\ e^{-t/\tau} \tag{6.5}$$

This model was fit to the spectrum of Figure 6.4 assuming that the signal originated from

a sum of distributions with the form of Equation 6.5 assuming the particles were N_2 (28 u) and a gas temperature of 292 K. As can be seen from the fit in Figure 6.4 that the data is well fit with a single distribution and a lifetime of 80 µs. This is consistent with the reported[63, 104, 105] lifetime of 80^{+40}_{-20}µs for the $a^1\Pi_g$ state, suggesting that the surface is sensitive to this state but not to $^1\Gamma_g^+$. If the latter state was indeed being detected, this would greatly skew the distribution to longer flight times[63].

As no filtering has been applied to the PMT, one cannot comment on the wavelength of the photons being emitted from the frozen layer. Without such information, it would be difficult to determine the exact de-excitation mechanism involved at the surface. It is likely that an energy transfer process is occurring which converts $N_2(a^1\Pi_g)$ to an intermediary state that then emits a photon through an electric dipole transition in a similar manner to the process observed in N_2 layers[63, 64]. Further work would be necessary to determine the wavelength range of the emitted photons in order to ascribe the specific intermediary state being formed.

6.2.3 Temperature Dependence of Layer Sensitivity

Just as with rare gas layers[45, 51], the sensitivity of solid CO_2 as a detector was found to be heavily dependent on the temperature of the cold finger. A study of the sensitivity was performed using electron impact of a gas CO_2 target which produces a significant number of $O(^1S)$ through several channels[56].

Using a 27 µs wide electron pulse with 100 eV impact energy, collisions were performed while varying the temperature of the cold finger between 17.8 K and 48 K. All obtained TOF spectra were normalized by scaling the height of the prompt photon peak to be equal across all spectra after removing any constant background signal. Representative spectra acquired across the temperature range can be seen in Figure 6.5. Photon fluxes arriving 40 µs to 150 µs after the initial prompt peak were then integrated in each scan to act as a proxy for the relative sensitivity of the layer.

The results of the sensitivity study are shown in Figure 6.6. Excimer emission was seen to stop at around 48 K. A nearly linear dependence can be seen as temperatures lower that begins to level off around 25 K. Measurements below 17.8 K could not be performed as this was the lower cooling limit attainable with the cold finger. Drawing from tendencies observed in other solid matrices[45, 64], it is very likely that the relative conversion efficiency plateaus at some temperature.

While CO_2 remains frozen up to 216 K, the likely explanation for the loss of signal above 48 K is increased vapour pressure at the surface of the detector. With this increase comes additional collisional losses which will quench the metastable species before they reach the detector surface. This phenomenon is commonly observed in frozen gas layer detectors[51, 63]. Unfortunately, this also means that CO_2 is not suitable as a high temperature metastable detection layer.

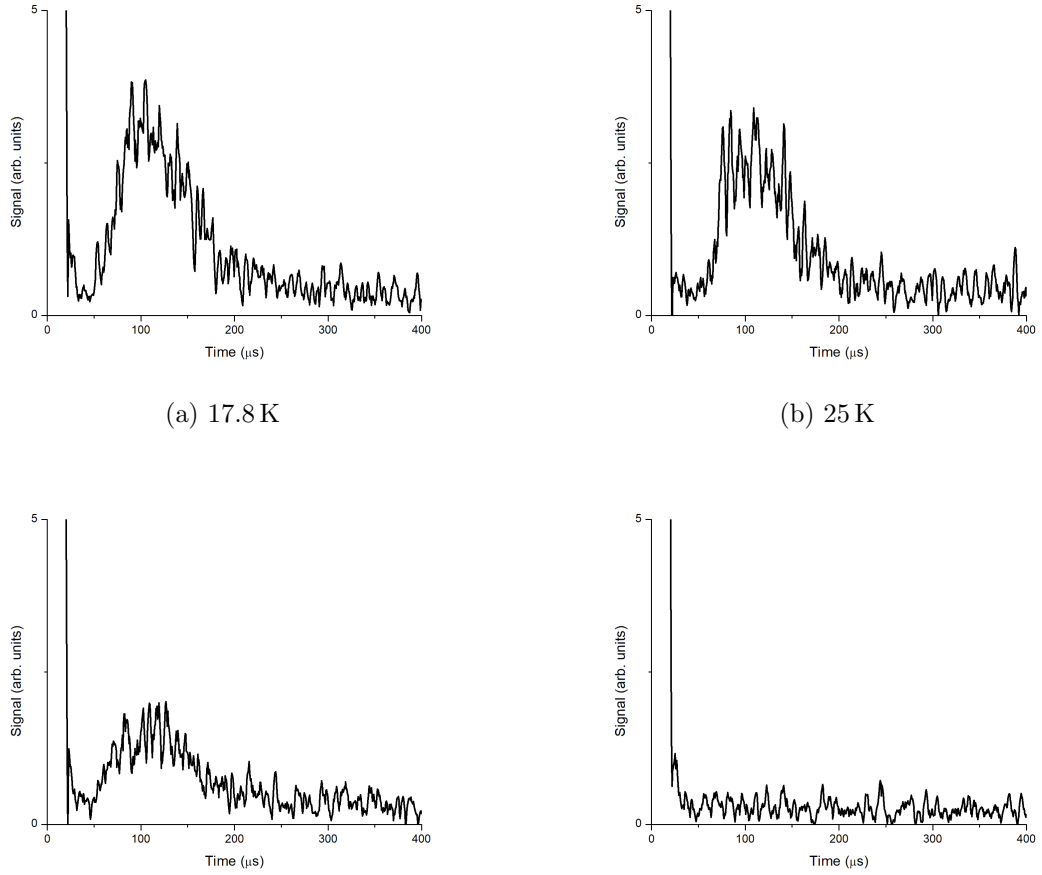

(a) 17.8 K

(b) 25 K

(c) 37 K

(d) 48 K

Figure 6.5: TOF spectra of O(^{1}S) from electron-impact of CO_2 measured with a solid CO_2 layer at various temperatures. All spectra have been normalized to match the heights of the prompt photon peaks for comparison. Savitzky-Golay filtering[88] was then applied to each spectrum. The O(^{1}S) signal can be seen to be maximal at 17.8 K where the detection efficiency was the highest. Sensitiviy can be seen to drop with increasing temperature until the metastable can no longer be observed at 48 K.

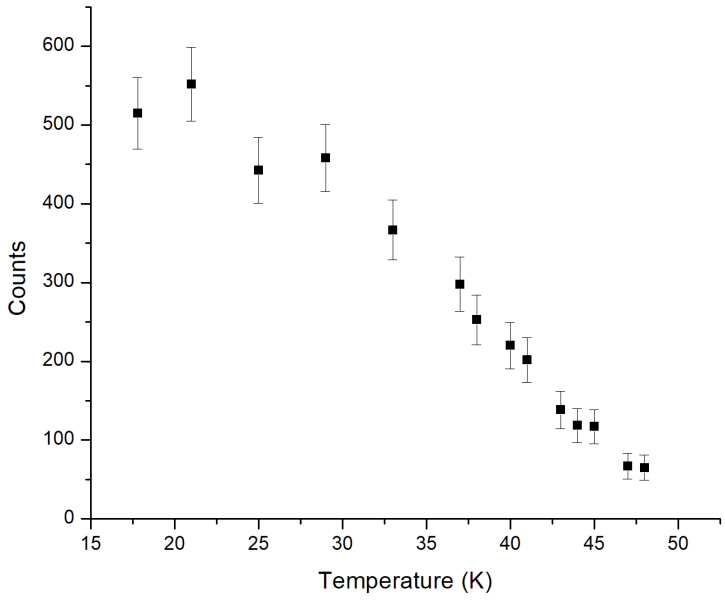

Figure 6.6: Temperature dependent efficiency curve for formation of excimers with a CO_2 layer. Results were obtained by varying the temperature of the cold finger and measuring photon counts after electron impact of CO_2.

6.3 N_2O

The use of solid N_2O was also investigated for its potential in detecting metastable states. These layers were not found to be sensitive to $O(^1S)$ or $O(^1D)$ in these experiments. As Sulphur is isoelectronic with oxygen, it is reasonable to assume that N_2O is also insensitive to the $S(^1S)$ state which is observable with other solid layers which are sensitive to metastable oxygen.

Interestingly, frozen N_2O was still found to be sensitive to $N_2(a^1\Pi_g)$. Shown in Figure 6.7 is the TOF spectrum acquired from electron impact of N_2 at 100 eV with the target beam injected parallel to the drift region.

As with solid CO_2 layers (Section 6.2.2), it was assumed that the source of metastables was singlet states of N_2. The model of Equation 6.5 was again fit to the data of Figure 6.7 using a least squares fitting procedure. Assuming a particle mass of 28 u and a temperature of 292 K, the distribution would correspond to a signal particle species with a lifetime of approximately 90 µs, indicating that the signal again originated from the $a^1\Pi_g$ state. Differences in the lifetime measured for N_2O and CO_2 are still within error for the reported lifetime of this state[63, 104, 105].

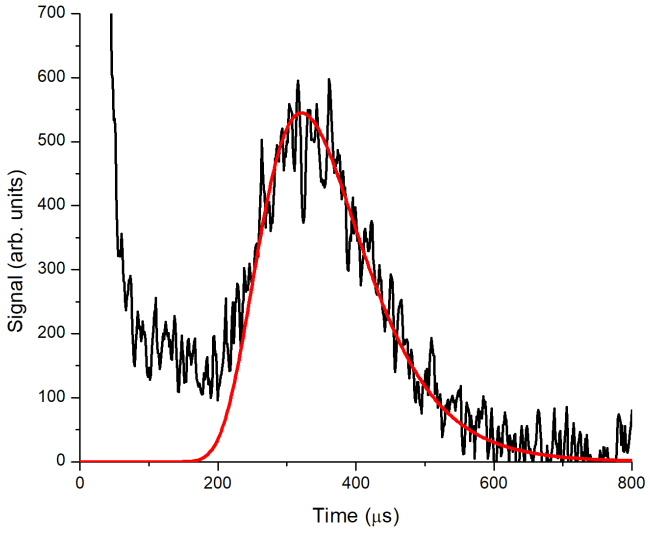

Figure 6.7: TOF spectrum for electron-impact of $N_2(a^1\Pi_g)$ on a N_2O layer at 100 eV. The fitted curve corresponds to a Maxwell-Boltzmann distributed sample of N_2 at 292 K assuming in-flight decay with a lifetime of 90 µs.

6.4 Future Work

While a preliminary study of CO_2 and N_2O surfaces as potential metastable state detectors was conducted in this work, there remains several tests which could be performed in order to better understand the chemistry occurring at these surfaces and their detection characteristics.

It would be of considerable interest to determine the conversion efficiency of these surfaces relative to the rare gases. Experiments involving measurement of metastable states generally take a significant amount of time due to the relatively low excitation cross-sections in comparison to optically allowed channels. As such, any improvement in the efficiency of the detector is greatly desired in order to reduce the acquisition time as much as possible and reduce costs associated with materials.

However, measuring the conversion efficiency is non-trivial. Typically, one normalizes the signal according to the prompt photon peak and then compares the integrated area of the metastable TOF distribution, assuming that the reflectivity of the surfaces are approximately equal. In the ideal case, this measurement needs to be done using the same spectral range in order to ensure that the spectral content of the prompt photon signal is the same, capturing the same optical excitation channels. As the de-excitation process in the various layers differ in their emission wavelengths, this would require the use of different filters to capture the same metastable fragment impacting the spectral content of the prompt signal. In some cases, one can compare the spectra using no filter which guarantees that the spectral

content of the prompt feature is identical but if multiple metastable features are present, one cannot compare the conversion efficiency for a specific state. For example, measuring the signal from CO_2 with no filter would sum signals from both $O(^1S)$ and $O(^1D)$ while in xenon, only the $O(^1S)$ signal would be present, preventing an accurate measurement of the conversion efficiency.

Additional TOF spectra for both $O(^1S)$ and $O(^1D)$ using solid CO_2 would also be desirable in order to achieve a better measurement of the lifetime of the intermediate states formed on the detector surface. The present estimate of the lifetime of the state formed from $O(^1S)$ was hampered by a low signal to noise ratio and so errors are on the order of 70%. Larger acquisition times would lead to a greatly improved statistics, reducing the size of the error bars. Determining the lifetime of $O(^1D)$ would require a comparable reference spectrum from neon employing the same electron pulse width.

Quantum chemistry calculations or additional experiments are also to further clarify the reaction occurring at the CO_2 surface. Without further information, it is not possible to ascertain the exact method by which de-excitation occurs in this system. Such calculations are non-trivial however, as they need to be taken to a very high accuracy, such as the CASSCF level, in order to determine the excited state energy levels. However, considering that the $O(^1S)$ process in particular has not been studied in detail, combined with the application of this process to interstellar ices, there does exist some motivation for such a calculation to be carried out.

6.5 Summary

In this chapter, several frozen layers were examined for their use in the detection of metastable species and compared to previous results for solid rare gases. Studies of CO_2 layers demonstrated they are capable of detecting both $O(^1S)$ and $O(^1D)$, emitting green and red light respectively when impinging on the surface. It was suggested that this process may occur through the production of either neutral CO_3 or its negative ion. The relative conversion efficiency as a function of temperature was also measured.

The suitability of various layers at detecting metastable N_2 was also examined. Both CO_2 and N_2O demonstrated the ability to detect the $a^1\Pi_g$ state but were unable to observe the $^1\Gamma_g^+$ state which has previously been resolved with solid N_2.

A brief summary of the results found in this chapter as well as previous investigations on the use of different layers for detecting metastables, including the rare gases, is provided in Table 6.1. Here, layers which have been found to be sensitive to various metastables is provided while indicating exactly which species they are sensitive to along with references to the relevant literature. This allows one to select the appropriate layer for the metastable in question for future experiments.

Table 6.1: Summary table of observed metastable signals in the optical wavelength range by various solid layers. Detection is based on a surface temperature of 18 K. An x indicates that no measurable signal could be found in the measurements taken within the visible spectrum while ?? indicates that the measurement has not been performed.

	Target					
	O	S	N	N_2	CO	
Detector	Observed Metastables					References
Ne	^{1}S, ^{1}D	^{1}S	x	x	??	[51], This Work
Ar	^{1}S	??	x	x	??	[51]
Kr	^{1}S	??	x	x	??	[51]
Xe	^{1}S	^{1}S	^{2}P	x	$a^3\Pi$	[51, 106]
CO_2	^{1}S, ^{1}D	??	x	$a^1\Pi_g$	??	This Work
N_2	^{1}S	??	x	$a^1\Pi_g$, $^1\Gamma_g^+$	??	[63, 93]
N_2O	x	x	x	$a^1\Pi_g$	??	This Work
H_2O	x	x	x	x	x	This Work

Chapter 7

Metastable N(^{2}P) Production in Electron Impact of N_2

Metastable states of atomic nitrogen have been found to play an important role in a variety of fields including active nitrogen flowing afterglows[107], the aurora[108], combustion[109], and discharge chemistry and plasma processing[9]. These energetic states are very reactive and play a considerable role in the atmospheric chemistry of Earth's upper atmosphere[110] and the atmospheres of other planets and moons in our solar system[111, 112].

In this chapter, electron-impact excitations of the $^2P_{1/2,3/2}$ states are examined. If the system is not quenched, these metastable states decay to the ground state via an electric quadrupole transition at 1040 nm or a magnetic dipole transition at 346.6 nm as shown in Figure 7.1. These states have traditionally been extremely difficult to measure as their reported[113] lifetime is 12 s, providing a strong motivation for the present work.

The ^{2}P state has been investigated by a number of authors. Some of the earliest studies date back almost a century to 1924 where Vegard[115] as well as McLennan and Shrum[116] bombarded frozen N_2 layers with electrons and "canal rays", examining the resulting lu-

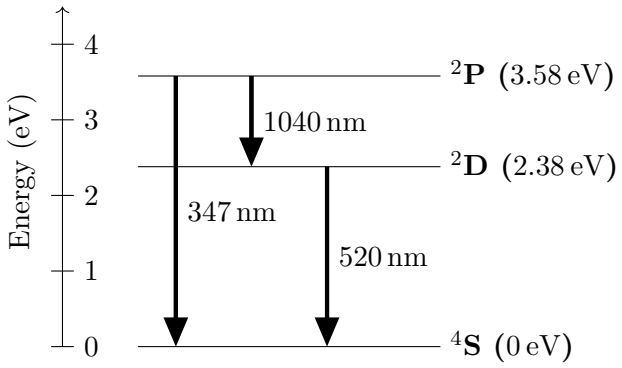

Figure 7.1: Energy level diagram indicating the relevant states in atomic N along with the associated transitions to the ground state. A more detailed level structure can be found in Chamberlain[114], Appendix VI.

minescence. In 1956 Herzfeld and Broida[117], when condensing an N_2 flowing discharge at 4.2 K, also noticed a long lived signal radiating around 523 nm corresponding to the N(^{2}D$\rightarrow^4$S) transition (Figure 7.1). A second, weaker peak was also noted at 347 nm which they attributed to the N(^{2}P$\rightarrow^4$S) transition. Thus, one would expect to observe fluorescence from the rare gas matrix at wavelengths close to those shown in the energy level diagram.

7.1 Experimental Setup

The apparatus is described in detail in Chapter 5. Electron-impact of N_2 was carried out in a crossed-beam mode with fragments being detected orthogonal to the target and projectile beams. In this configuration, one expects to see dissociated atomic N rather than N_2 molecules along the detection axis. The electron beam was pulsed (27 µs width) with fragments drifting to the solid Xe layer which was maintained at 18 K. The impinging metastables formed excimer states which radiated and the resultant photons were detected by the photomultiplier tube.

First, TOF spectra were acquired with a 340 nm filter with a 85 nm FWHM which corresponded to the spectral region where the metastable feature was observed. Acquisition of this spectrum took approximately two weeks. An excitation function was then obtained over the 0 eV to 180 eV range. Taking this data took approximately two months.

7.2 Results and Discussion

The observed TOF spectrum at 100 eV impact energy can be seen in Figure 7.2. In addition to the prompt photons, two peaks can be observed indicating the presence of metastable fragments produced by two separate dissociation channels. The prompt photon signal corresponds to emission from the (0,0) $C^3\Pi_u \rightarrow B^3\Pi_g$ Second Positive band of N_2 which radiates at 337.1 nm[105]. As the filter was centred at 340 nm, the two metastable signals can be associated with the ^{2}P$\rightarrow^4$S transition. No signal could be observed in the region of 520 nm and corresponding to the ^{2}D$\rightarrow^4$S transition, possibly due to the extremely long (200 s) lifetime of the N(^{2}D) state (Figure 7.1).

The two metastable peaks can be separated by fitting separate Gaussian curves to TOF spectrum after the prompt photon peak as seen in Figure 7.2. The two peak centres correspond to released kinetic energies of 2.7 eV and 0.56 eV for the "fast" and "slow" peaks respectively. Overlap of the two peaks can be seen for arrival times of 25 µs to 100 µs. This makes separation of the faster peak difficult due to the significant contribution of the slower peak and the prompt photon pulse in this region and so the major focus of the investigation was on the slower peak. The faster metastables are commented on later in the chapter.

For the slower peak, fragments can be observed to arrive for times up to approximately 300 µs after the prompt photons and are well separated from the faster signal in the 100 µs

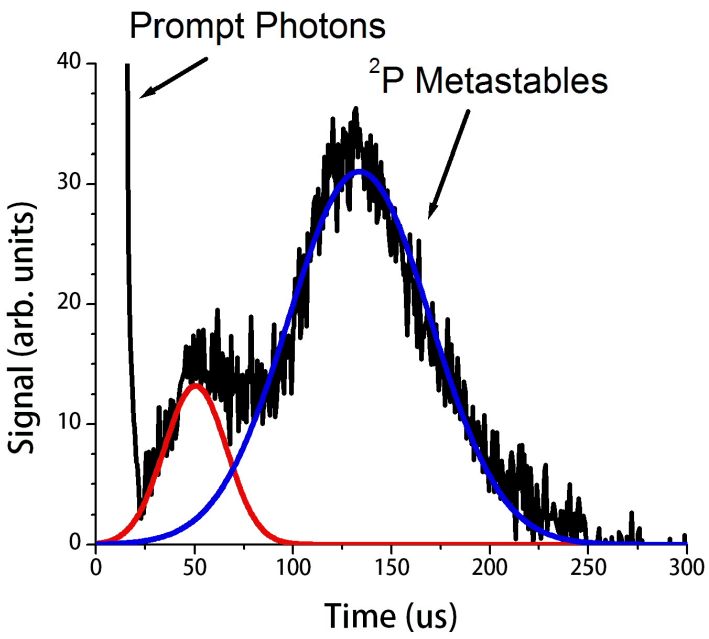

Figure 7.2: Photon TOF spectrum for e-N collisions at 100 eV impact energy.

to 300 µs range. This tail corresponds to total released kinetic energies of approximately 0.1 eV, assuming equal energy sharing between the two fragments upon dissociation of the parent N_2 molecule. This implies that the parent molecule has a threshold energy very close to the dissociation limit for production of N(^{2}P), which is confirmed in the proceeding analysis.

In addition to the TOF spectrum, one can also consider the excitation probability of the slower peak as a function of energy. In order to eliminate any contribution from the faster metastable group, photon counting was gated to measure signals arriving 100 µs to 200 µs after the prompt photons. Both the prompt and metastable signals for the 5 eV to 30 eV range can be seen in Figure 7.3. A constant background subtraction has been applied to eliminate any photons coming from the cathode which arrive throughout the counting windows. The prompt photons are the result of emission by excitation of the (0,0) $C^3\Pi_u \rightarrow B^3\Pi_g$ Second Positive band which radiates at 337.1 nm. Excitation of this state has been shown[118, 119] to be strongly peaked around 14 eV, which allows the impact energy scale to be fixed without the introduction of additional calibration targets.

Examination of the excitation function over the 0 eV to 180 eV range, as seen in Figure 7.4, provides additional information regarding possible excitation mechanisms for the production of N(^{2}P) metastables. While there is considerable noise due to low statistics, one can still observe a rapid onset from threshold to a shoulder region near 25 eV to 30 eV before the signal reaches a maximum and then a gradual fall off at higher energies. One may also be tempted to interpret further structure in the high energy tail above 75 eV; however

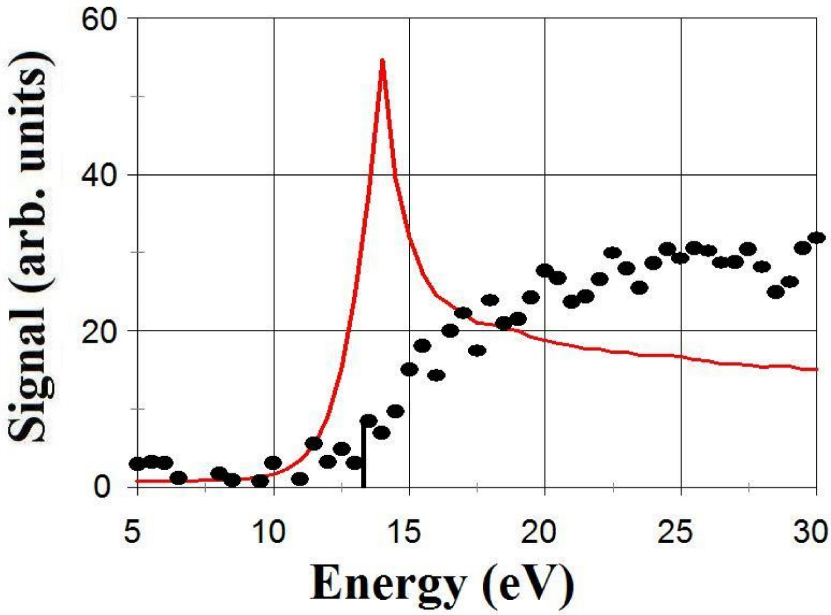

Figure 7.3: Excitation functions for the $C^3\Pi_u \rightarrow B^3\Pi_g$ (0,0) Second Positive band (solid curve) and metastable signal (dots) arriving 100 µs to 200 µs of the prompt photon signal. Constant background subtraction has been applied to the metastable signal. The vertical line at 13.33 eV is shown corresponding to the theoretical value for dissociation into N(^2P) + N(^4S).

these variations are likely due to statistical noise. Including the constant background from the cathode, the $\sqrt{n}$ uncertainty in the signal is approximately 9 units which more than accounts for the fluctuations in the tail. The shoulder in Figure 7.4 however, suggests a two channel excitation process. The rapid onset from threshold is typical (Section 4.2.3) of a spin flip process while the broad, slowly decreasing tail at high energies is indicative of an optical dipole or at least spin-allowed transition.

It is observed in Figure 7.3 that the threshold for metastable production is very close to the theoretically determined dissociation limit for N(^{2}P) + N(^{4}S) of 13.33 eV. This, combined with the kinetic energy distribution of Figure 7.7, would suggest that a direct dissociation process

$$e + \mathrm{N}_2(X^1\Sigma_g^+, \nu = 0) \rightarrow e' + \mathrm{N}_2^* \rightarrow \mathrm{N}(^2\mathrm{P}) + \mathrm{N}(^4\mathrm{S}) \tag{7.1}$$

is a significant contributor to the observed metastable signal. This is further evidenced by the molecular potential curves shown in Figure 7.5, adapted from the work of Hochlaf[120]. Excitation from the ground state corresponds to the shaded Franck-Condon region. It can be seen that below 15 eV, the only state which crosses this region is the $B'^3\Sigma_u^-$ state making it a likely candidate for the intermediate N_2^* state in Equation (7.1). The other states in Figure 7.5 can be ruled out as they would correspond to a higher threshold energy. In

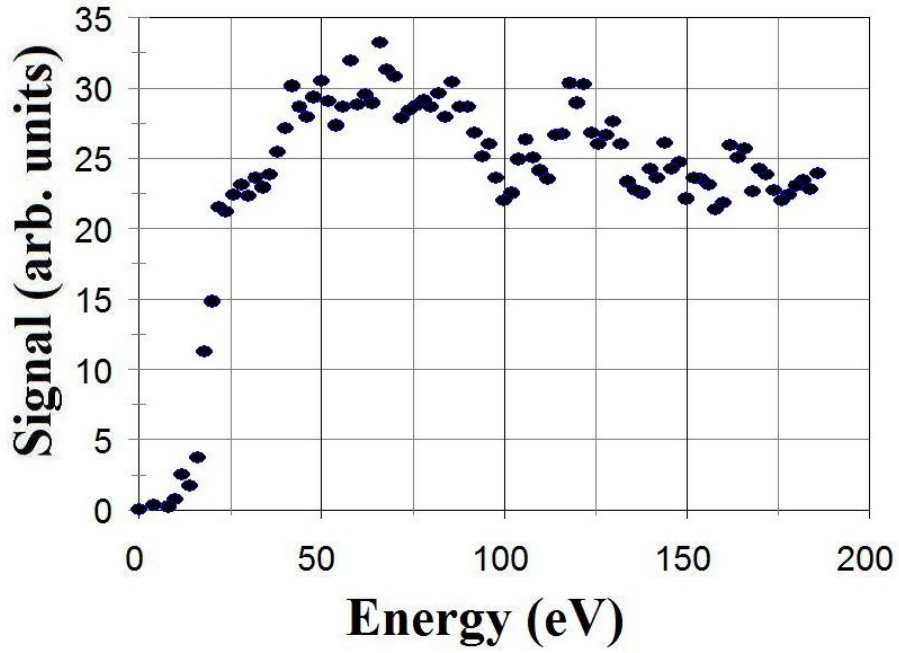

Figure 7.4: Excitation function for the observed metastable signal for the 0 eV to 180 eV energy range. Counts correspond to metastables arriving 100 µs to 200 µs after the prompt photons. A constant background subtraction has been applied followed by adjacent average smoothing. Including this background, the statistical uncertainty in the points is about 9 units.

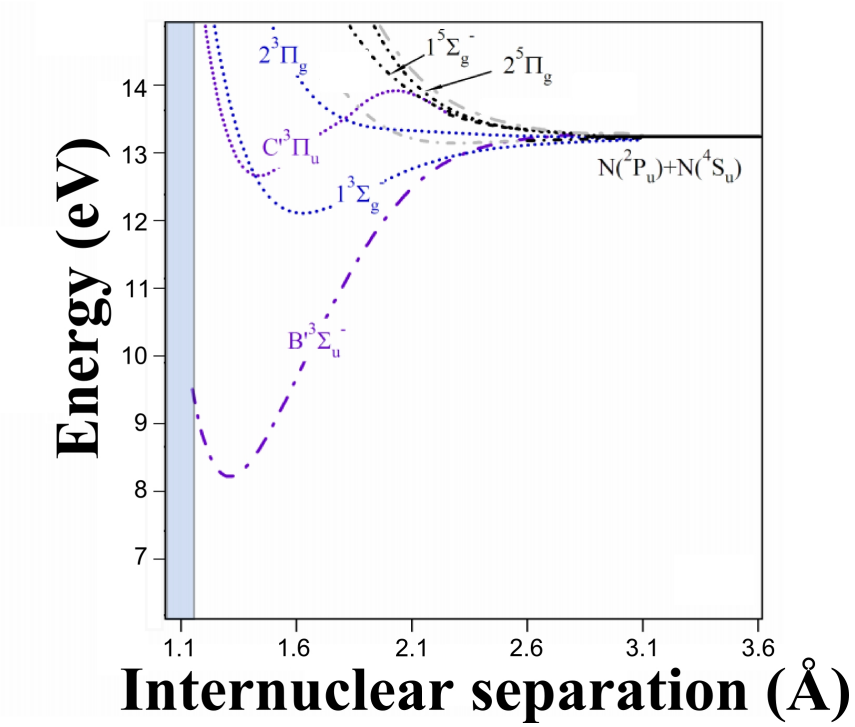

Figure 7.5: Molecular potentials for the N_2 system including the $B'^3\Sigma_u^-$ state converging to the N(^{2}P) + N(^{4}S) dissociation limit. The figures is adapted from the work of Hochlaf[120]. The Franck-Condon region is shaded for excitation from the ground state corresponding[121] to internuclear separations of 1.06 Å to 1.16 Å[105].

contrast, the $B'^3\Sigma_u^-$ potential overlaps the Franck-Condon region along the inner repulsive portion of the curve and so excitation into this state could be occurring up to and even beyond the dissociation limit, producing N(^{2}P) fragments with very little kinetic energy. This would correspond to a threshold close to 13.33 eV. Additional evidence can also be seen in the 0 eV to 20 eV behaviour of the excitation function (Figure 7.4) where the onset is characterized by a rapid increase from the threshold. This is indicative of a spin flip process[82] like the singlet-triplet transition which has been proposed.

The second excitation channel is likely a pre-dissociation process. In electron impact studies of neutral N_2, Cosby[85] found evidence of pre-dissociation into mostly N(^{2}D) + N(^{4}S), but also weakly into N(^{2}P) + N(^{4}S). Ajello *et al*[122], in their cross section measurements of electron impact of N_2 into the $c_4'^1\Sigma_u^+$ and $b'^1\Sigma_u^+$ states, also found that the latter state is 84% pre-dissociated with a yield that increases with vibrational quantum number. Figure 7.6, adapted from Little and Tennyson[123], shows the potential curves for these two states. It can be seen that higher vibrational levels of the $b'^1\Sigma_u^+$ state certainly lie close to the N(^{2}P) + N(^{4}S) dissociation limit. Such an excitation from the ground state would also be dipole allowed suggesting that the pre-dissociation mechanism follows the reaction

$$e + N_2(X^1\Sigma_g^+, \nu = 0) \rightarrow e' + N_2(b'^1\Sigma_u^+) \rightarrow N_2^*(\text{pre-diss.}) \rightarrow N(^2P) + N(^4S) \qquad (7.2)$$

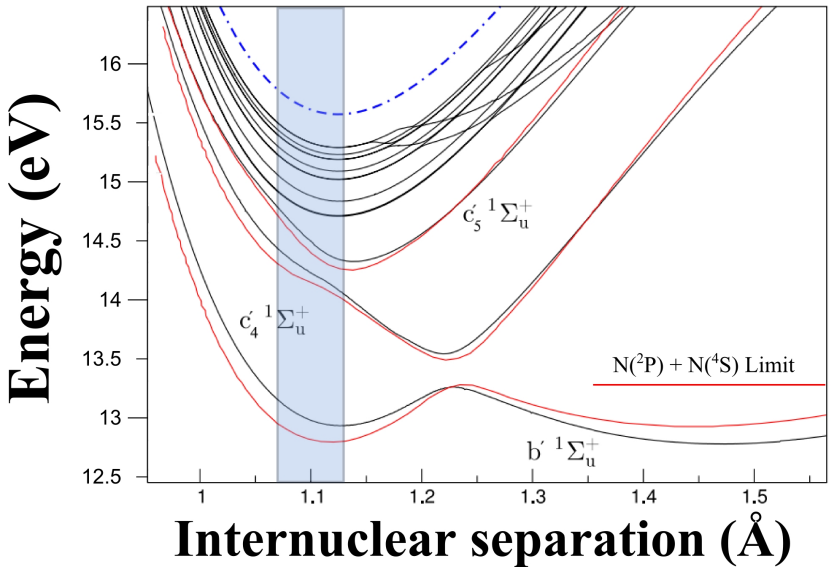

Figure 7.6: Molecular potentials for the N_2 system including the $c_4{}'{}^1\Sigma_u^+$ state adapted from Little and Tennnyson[123]. The $N(^2P_0) + N(^4S_0)$ dissociation limit at 13.3 eV is indicated by the solid line on the right. The Franck-Condon region is shaded for internuclear spacings of 1.06 Å to 1.16 Å[105]. The black curves represent the calculations of Little and Tennyson compared to the previous work of Spelsberg and Meyer[124] which is in red.

An optical dipole process is also supported by the higher energy region of Figure 7.4, with a broad maximum and gradual decline which is the behaviour predicted by Bethe-Born theory for optically allowed transitions[82]. This reaction would also imply the existence of singlet-triplet mixing, as the singular multiplicities of the final dissociated state is inconsistent with a pure dipole transition process.

While significant overlap of the slow and fast peaks in the 25 µs to 100 µs range prevented acquisition of an excitation function for the fast peak, one can still make some comments on possible excitation routes for this signal. To glean more information, one can transform the TOF spectrum of Figure 7.2 into the energy domain as in Figure 7.7 by applying Equation (5.1) under the assumption of equal energy sharing between the dissociated fragments. One sees that the slower peak corresponds to products with kinetic energies mostly below 2 eV while the faster one is produced by fragments over a much broader energy range of about 1 eV to 7 eV while peaking near 3 eV.

The energy range of the faster $N(^2P)$ fragments would imply that the inner repulsive part of the excited state potential curves crosses the Franck-Condon region around 14 eV to 20 eV in order for there to be sufficient energy for excitation of the $N(^2P)$ and the kinetic energy of the released fragment, assuming dissociation into the $N(^2P) + N(^4S)$ final state.

Considering the numerous theoretical calculations[105, 120, 123–128] of high lying excited N_2 states, possible states which could account for the fast peak can be seen in Figure 7.5 can be identified. The inner repulsive curves of the $C'^3\Pi_u$ and $1^3\Sigma_g$ states can be seen to

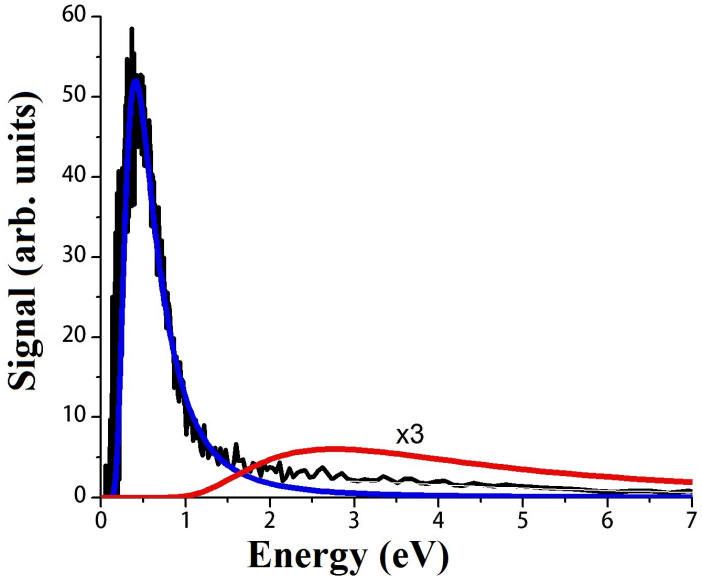

Figure 7.7: Observed spectrum of the released kinetic energy for N(^{2}P) fragments from dissociation of N_2 at 100 eV impact energy based on the data of Figure 7.2. The solid lines correspond to the Gaussian peaks plotted in Figure 7.2. The high energy curve has been multiplied by a factor of 3 for clarity.

cross the Franck-Condon region above 15 eV and could be possible candidates. Excitation into these states at this energy would result in a released kinetic energy of roughly 1.7 eV which would be in agreement with the observed signal of Figure 7.7. Any states contributing to this signal would also require mixture with a singlet state for appreciable excitation at higher energies as observed in Figure 7.2.

While production of N(^2P) is possible by higher energy dissociation states with partner fragments other than N(^{4}S), this remains unlikely. Higher energy excitations would produce steeper inner repulsive curves[71], resulting in higher appearance thresholds and increased kinetic energy upon release than those observed in the TOF spectrum.

7.3 Conclusion

In this chapter, the production of N(^{2}P) was selectively observed from dissociative excitation of N_2 using a novel rare gas matrix detector. Measurement using TOF methods revealed two separate excitation channels, or groups of channels which lead to a final N(^{2}P) fragment upon dissociation. Using the released kinetic energy, we were able to suggest parent molecular states according to their alignment with the Franck-Condon region of the ground state and recent theoretical calculations. It was found that both direct and pre-dissociation mechanisms are most likely involved.

Chapter 8

Observation of Electron Impact Dissociation of OCS Using a Cold Neon Matrix

Carbonyl sulphide (OCS) is a linear triatomic molecule that is of interest in several fields. It is believed to play a role in the chemistry of the sulphur cycle[1] in Earth's atmosphere and is present in astrophysical phenomena such as diffuse and interstellar dark clouds[129]. It also appears as a pollutant in various low-temperature plasmas[130] and possesses a strong permanent electric dipole moment[131] making it a standard reference for dipole measurements.

One of the earliest studies of metastable states formed by electron-impact dissociation of OCS was by van Brunt and Mumma[132] who found that the process resulted in a variety of metastable fragments including CO($a^3\Pi$), S(^{5}S), and O(^{5}S) in addition to a number of high lying Rydberg states. However, they were unable to isolate these various fragments or their associated collision channels with their apparatus. Further work was performed by Barnett *et al.*[133] who were able to further resolve these dissociation fragments and determined their kinetic energy distributions through the combination of channeltron and tantalum Auger detectors. Kedzierski *et al.*[60] have also studied the production of S(^{1}S) using a solid xenon detector. They observed that this particular state was only produced through a single dipole-allowed channel

$$\mathrm{OCS} + e \rightarrow \mathrm{CO}(X, \nu) + \mathrm{S}(^1\mathrm{S}) + e' \tag{8.1}$$

where the CO fragment is excited with a few quanta of vibrational energy. However, to the author's knowledge no studies of the S(^{1}D) state are present in the literature.

The present work re-examines dissociation of this molecule using a solid neon detector with the motivation of trying to observe the production of S(^{1}D) from electron impact. It has previously been shown[45] with O(^{1}S) and O(^1D) that the use of different rare

gases, such as neon and xenon, can result in significant changes to the spectral emission of excimers formed by these metastable states. In the case of $O(^1D)$, moving from xenon to neon shifted the emission from the infra-red to the visible range permitting study of this state using traditional PMT detectors. As sulphur is isoelectronic with oxygen, it is hoped that a similar effect will enable the detection of $S(^1D)$ using a solid neon layer.

The production of $S(^1D)$ through photodissociation has been studied extensively[134–141], revealing several optical channels. Dissociation via the first absorption band in the 192 nm to 248 nm region has been shown[139] to produce $S(^1D)$ and $S(^3P)$ with a branching ratio of 95:5. Production is dominated by two dissociation channels throughout most of the band[137]. Recently Bai *et al.*[141] have also shown that a third, spin forbidden channel opens up at ~ 210 nm.

A representation of the potential energy surface along the OC-S bond is shown in Figure 8.1. It can be seen that there are three molecular states, $1^1\Sigma^+$, $1^1\Pi$, and $1^1\Delta$ which converge to the $S(^1D)$ limit. In the linear geometry, transitions into these states are optically forbidden but upon bending the $1^1\Sigma^+$ maps onto the $1^1A''$ state while $1^1\Pi$, and $1^1\Delta$ split into A' and A'' Renner-Teller pairs[137], which are then accessible through vibronic coupling. As electron collisions relax optical selection rules governing photodissociation, these transitions could occur even in the purely linear configuration and so it may be possible to observe $S(^1D)$ from dissociation of these states in the present study.

In regards to the detection of metastable sulphur by rare gas matrices, much of the previous experimental and theoretical work has been performed with xenon and Argon. To the author's knowledge, there is very little theoretical information on the molecular structure of neon sulphide (NeS). Klos *et al.*[143] have calculated potential curves for the $^3\Pi$ and $^3\Sigma^-$ states converging to the $S(^3P)$ dissociation limit for several sulphur-rare gas dimers, including neon, with accompanying experimental data. Aquilanti *et al.*[144] have provided similar data for NeS subject to a magnetic field where the Zeeman interactions separate the hyperfine levels. However, there appears to be no calculations for potential curves beyond the ground state manifold.

Yamanishi *et al.*[145] have determined the potential curves for excited states of XeS which may serve as a guide for the possible behaviour of the NeS. They show a series of repulsive curves converging to the Xe + $S(^3P)$ ground state while states converging to the $S(^1S)$ and $S(^1D)$ limits are attractive. Lara *et al.*[146], also found similar trends in the potential curves for states converging to the $S(^3P)$ and $S(^1D)$ limits in ArS. The nature of these curves is similar to those observed in XeO[51] and NeO[45], which suggests that similar trends may exist in NeS.

The lack of data regarding the production of $S(^1D)$ through electron impact provides the primary motivation for the present work. A secondary objective is to glean information regarding the suitability of neon as a detector for observing $S(^1D)$ or $S(^1S)$ states.

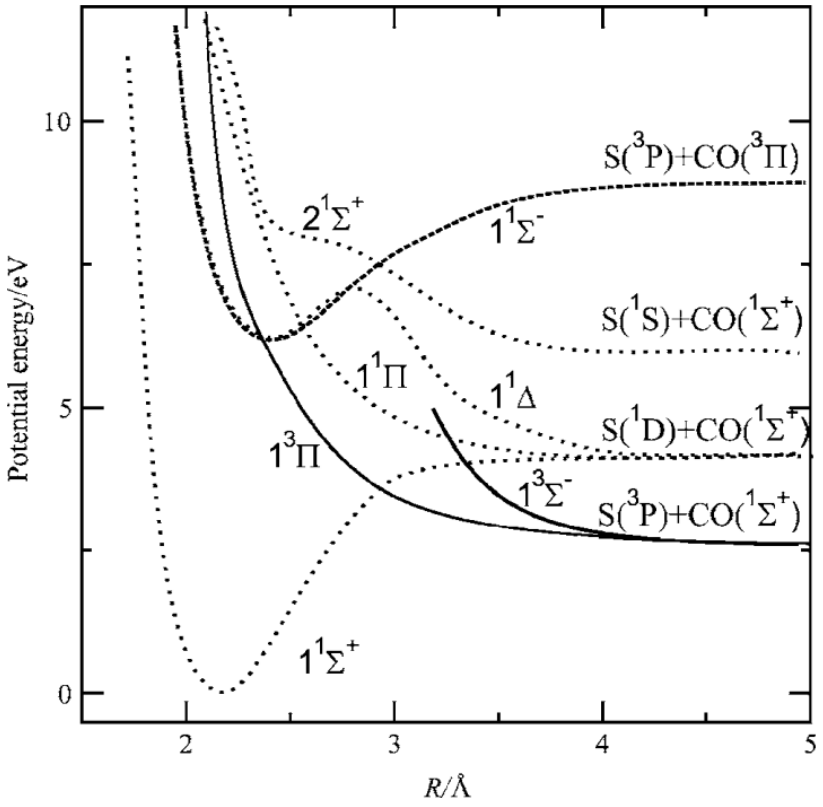

Figure 8.1: Potential energy curves for the OC-S bond assuming the C-O bond is at its equilibrium length of 1.13 Å. Singlet and triplet states are denoted with a dashed line or a solid line respectively. Figure is adapted from Brouard *et al.*[142].

8.1 Setup

Electron impact studies were conducted using the apparatus described in Chapter 5. The electron and OCS molecular beams were arranged in a crossed geometry, mutually orthogonal to the line of sight of the detector. This ensured that only dissociated fragments arrive at the detection surface as opposed to metastable OCS states. During gas injection, the chamber was maintained at 10^{-5} torr.

A 27 µs electron beam pulse with energy of 100 eV was introduced, dissociating the OCS target. Collision fragments would then travel down the drift tube toward the detection layer maintained at 21 K, forming an excimer state and subsequently radiating. The resulting photons were then detected by the PMT and registered by the MCS to produce a time-of-flight spectrum. Emission from both neon and xenon layers were examined in order to allow for comparison with the previous results of Kedzierski *et al.*[60].

A series of passband filters were places in front of the PMT to selectively measure different parts of the optical wavelength region in order to isolate the metastable feature. These filters were characterized by an 85 nm FWHM and a 80% transmittance at the centre of the band.

8.2 Results

The observed TOF spectra, without any bandpass filtering applied, can be seen in Figure 8.2 for both neon and xenon layers. In both cases, a single dominant metastable feature is observed that peaks around 125 µs. The TOF peak seen in the xenon spectrum was attributed to S(^{1}S) by Kedzierski *et al.*[60] produced through the dissociation channel described in Equation (8.1). As the peak in the neon spectrum has the same shape and arrival time, this would suggest that the feature also originates from the same metastable species, namely S(^{1}S). As no additional metastable features were observed, it is very likely that no S(^{1}D) signal was measured.

Passband filters centred at 400, 450, 500, 550, and 600 nm as well as a red filter were all unable to detect emission. A clear metastable signal was only visible when applying a 340 nm filter, shown in Figure 8.3, a wavelength significantly smaller than that of the gas phase S(^{1}D-^{3}P) transition at 458 nm (Figure 8.4). When comparing the integrated counts between the filtered and unfiltered curves of Figure 8.3 arriving in the 70 µs to 210 µs region, it was found that about 17% of the signal is transmitted. After consulting the manufacturer supplied transmittance curve for the filter, it was found that such a transmission ratio is characteristic of light of approximately 270 nm or 380 nm. As the former is well beyond the frequency cut-off of the PMT, the latter is likely close to the wavelength of the observed radiation.

Radiation at such a short wavelength presents a number of possibilities. It could be the case that it is indeed caused by a S(^{1}S) excimer whose emission wavelength is significantly

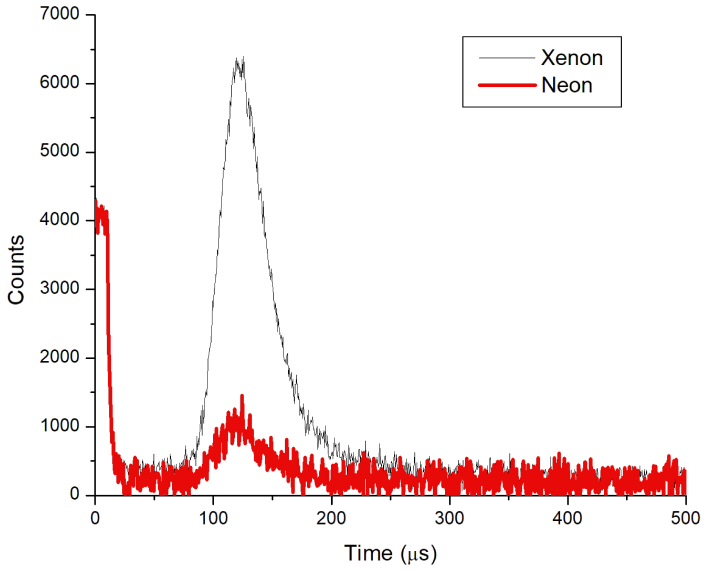

Figure 8.2: Observed TOF spectrum from electron impact of OCS at 100 eV using both xenon and neon matrices, shown with thin and thick lines, respectively. A constant background has been removed from both spectra before scaling to match the prompt photon peak in both measurements which allows for comparison of the relative strength of the metastable features. It can be seen that a significantly larger S(^{1}S) signal is observed when using the Xe matrix in comparison to the Ne matrix.

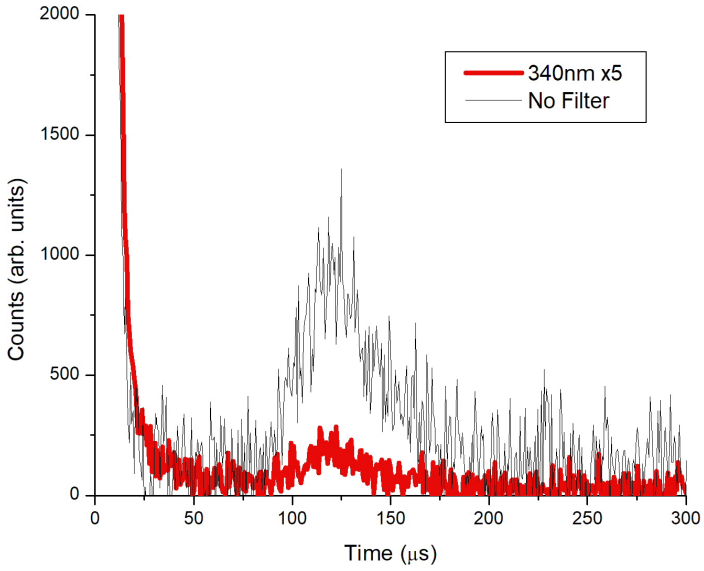

Figure 8.3: Comparison of the TOF spectra of electron impact of OCS using a neon matrix without a PMT filter and applying a 340 nm UV bandpass filter. The UV signal has been scaled by a factor 5 for clarity. Both signals have similar TOF distributions.

blue-shifted from the natural transition wavelength. Another possibility is that the radiation originates from an excimer formed by another metastable state such as CO($a^3\Pi$) or S(^{5}S). Finally, a different excitation mechanism may be occurring during the interaction with S(^{1}S) at the detector surface that does not correspond to an excimer process. All of these possibilities will be discussed in detail in Section 8.3.

The released kinetic energy of the fragments were also plotted in Figure 8.5 based on Gaussian curve fitting of the TOF peaks of Figure 8.2. The neon data was fit by first assuming that the fragments were atomic sulphur and then again assuming they were CO fragments. Both distributions are shown in Figure 8.5. It can be seen that the distribution

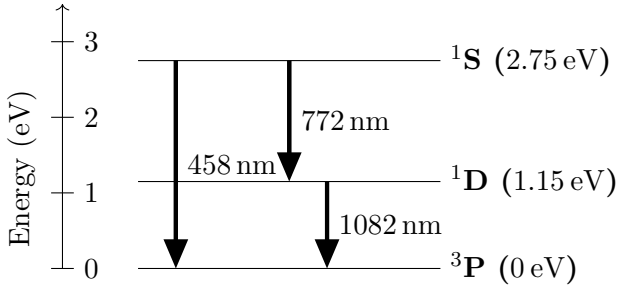

Figure 8.4: Energy level diagram for atomic sulphur with transitions within the ground configuration. Spectroscopic data has been taken from the NIST spectral database[147].

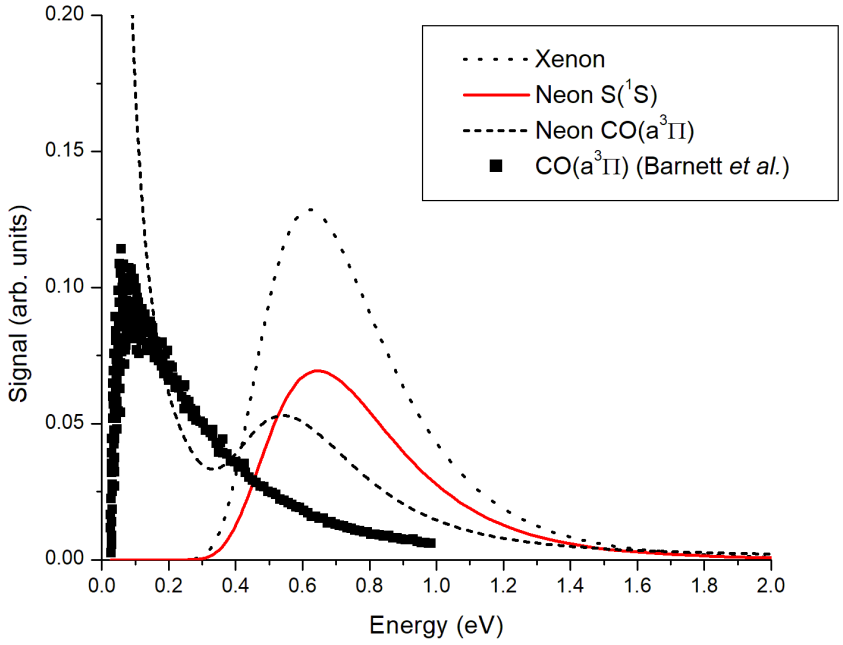

Figure 8.5: Released kinetic energy distribution from neon at 100 eV impact energy. The solid curve is fit assuming the incident particle is atomic sulphur while the dashed line assumed the particle is CO. For comparison the dotted line shows the released kinetic energy distribution of $S(^1S)$ from Xeon and the dots indicated the distribution of $CO(a^3\Pi)$ reported by Barnett *et al.*[133]. Comparing the shapes of these curves, it is very likely that the signal observed with solid neon originates from atomic sulphur.

in which the signal was assumed to be $S(^1S)$ has a similar shape and arrival time as that observed using a solid xenon layer, suggesting that the distributions correspond to the same metastable species. On the other hand, when comparing the distribution assuming CO to the released kinetic energy spectrum reported by Barnett *et al.*[133], they can be seen to be very dissimilar, suggesting that the observed emission is not due to detection of $CO(a^3\Pi)$.

In their analysis of $S(^1S)$ production, Kedzierski *et al.*[60] set the threshold for the dissociation channel of Equation 8.1 at 8.1 eV. Assuming this to be correct, the total energy transfer to the S atom is approximately 8.4 eV to 10.1 eV. Considering the potential energy surface of Figure 8.1, such energies suggest that dissociation producing $S(^1S)$ occurs after excitation to the inner wall of the $2^1\Sigma^+$ curve.

Excitation functions were not obtained in this study. During the course of this work, the rotary vane pump backing the vacuum system failed due to degradation of the seals on the roughing pump. This was likely due to damage from the injected OCS. As such, the experiment was stopped before further data could be taken.

8.3 Discussion

While no signals from $S(^1D)$ were observed, this is likely due to the fact that the PMT was blind to the radiant photons rather than from a lack of production. Considering the gas wavelength of the $S(^1D \rightarrow ^3P)$ transition of 1082 nm, the Xe + $S(^1D)$ excimer radiation is likely beyond the 850 nm cutoff of the PMT detector and much farther into the infrared. In future experiments, detection of such infrared photons would be possible with the use of single-photon avalanche photodiodes which are sensitive[148] in this spectral range.

It is possible however, to make some comments on the the dissociation channels that produce $S(^1D)$ based on the results obtained for $S(^1S)$ and from previous photodissociation studies. As the inner walls of the $2^1\Sigma^+$ and $1^1\Pi$ states are quite close, the Franck-Condon factor for excitation into the latter state should be quite high. Such a channel is also optically allowed and so one would expect the majority of $S(^1D)$ production to occur through the process

$$OCS + e \rightarrow OCS(1^1\Pi) + e' \rightarrow CO + S(^1D) + e' \tag{8.2}$$

Production of $S(^1D)$ may also occur from the $1^1\Delta$ state. As previously noted, this state is optically forbidden in the linear geometry but excitation would still be possible during electron-impact which can break optical dipole selection rules. Neglecting any vibronic coupling, this transition is spin-allowed but optically forbidden and so one would expect the electron-impact cross section to have a mostly E^{-1} dependence at higher impact energies (Section 4.2.3).

The question remains as to the source of the ultraviolet emission observed in this experiment. As previously mentioned, there appear to be three probable explanations. If the signal does indeed originate from $S(^1S)$, then the radiation at near 340 nm is significantly

blue shifted from the gas phase S(^{1}S-^{3}P) transition at 458 nm (see Figure 8.4). It may also be possible that the signal is due to radiation from another metastable species observed in dissociation of OCS such as CO($a^3\Pi$) or S(^{5}S). Finally, another reaction may be occurring between the detector and S(^{1}S).

Such a significant blue-shift to the excimer radiation is highly unlikely. It would require that the Ne + S(^{1}S) excimer forms a repulsive potential curve and then radiates to the ground state well above the dissociation limit. Since molecular vibrations occur on timescales orders of magnitude less than optical transitions, one would expect that such a formation would quickly dissociate rather than optically decay.

Barnett *et al.*[133] had previously reported detection of the CO($a^3\Pi$) state in electron-impact dissociation of OCS. While the emission wavelength from a neon surface for this metastable excimer is unknown, previous work in xenon[47] found radiation to occur at 320 nm and it is reasonable to assume that the emission is occurring near this wavelength and so would be weakly transmitted by the 340 nm filter. However, when comparing the released kinetic energy distributions of Barnett *et al.* to the present data in Figure 8.5, the two are very dissimilar which appears to rule this possibility out.

While S(^{5}S) may be the source of the observed signal in Figure 8.2, there are several arguments why it is an unlikely candidate. First, Delalic *et al.*[149] have determined the lifetime of S(^{5}S) to be 9.2 µs. Such a short lifetime would imply that the state should decay before reaching the detector surface unless the released kinetic energy was significantly higher than those seen in Figure 8.5 if the signal is atomic sulphur. As such, the number of particles reaching the detector surface would be marginal and therefore unlikely to provide a sufficient signal to be detected. Second, comparing the flight times measured by Barnett *et al.*[133] for S(^{5}S) fragments and accounting for differences in the flight tube lengths between their apparatus and the one used in these experiments, the observed TOFs do not align with their measurements of S(^{5}S). While the fact that their data was taken at 30 eV impact energy while the present spectrum was obtained at 100 eV, permitting the opening of new dissociation channels, the above evidence provides a strong basis that the signal does not originate from S(^{5}S).

It may also be possible that the signal can be attributed to O(^{1}S). Previous studies by LeClair *et al.*[57] have shown that a secondary excimer emission from O(^{1}S) in xenon, corresponding to the O(^{1}S-^{3}P) transition is visible with a 340 nm filter. The corresponding decay process in neon has not been reported but would still be red-shifted from the gas phase wavelength at 297 nm[147] and may possibly be detectable with the applied filter. While the production of O(^{1}S) from dissociation of OCS is quite low[60], there may have been sufficient production in this experiment for a metastable feature to be visible in the TOF spectrum of Figure 8.2.

Detection of O(^{5}S) is another possibility. In their studies of metastable production in OCS, van Brunt and Mumma[132] noted that one of their observed features may have been

attributable to O(^{5}S) production through either of the following processes

$$\mathrm{OCS} + e \rightarrow \mathrm{O}(^5\mathrm{S}) + \mathrm{C}(^3\mathrm{P}) + \mathrm{S}(^1\mathrm{D}) + e' \tag{8.3}$$

$$\rightarrow \mathrm{O}(^5\mathrm{S}) + \mathrm{C}(^1\mathrm{D}) + \mathrm{S}(^3\mathrm{P}) + e' \tag{8.4}$$

Their kinetic energy distribution would also be consistent with that of Figure 8.5 if the observed particle was assumed to be oxygen instead of sulphur. Observation of O(^{5}S) with solid neon layers has never been reported and so it is unknown if the layer would even be sensitive to this state.

A final possibility is that the radiation is due to a different process occurring at the surface other than excimer formation. A direct conversion process may be occurring to an excited level in neon which then subsequently radiates. There is a large number of spectral lines corresponding to the $2p^5 4p - 2p^5 3s$ manifold transitions near 370 nm. These lines would certainly be detectable with the ultraviolet filter in place and would be seen to occur when the S(^{1}S) atoms reach the detector. However, these excited states all lie over 20 eV above the ground state. Therefore, S(^{1}S) atoms reaching the detector with the kinetic energy distribution of Figure 8.5 would not be able to transfer sufficient energy to excite atoms within the solid neon layer from the ground state. This makes such a conversion process energetically infeasible.

8.4 Future Work

There are a number of hypotheses which have been presented in this chapter to explain the observed data. However, further experiments are required in order to determine definitively the reaction mechanism which is producing the observed ultraviolet emission. Below, several possible extensions of this investigation are discussed which would further elucidate the situation.

In principle, one could examine the excitation function for the observed metastable feature to determine its appearance energy. This was not possible using the present setup due to low signal strengths and the detrimental effect of OCS on the vacuum equipment with prolonged use. Pumps which are more suited to working with corrosive gases would be ideal for this situation and would permit the acquisition of the data needed to produce an excitation function. The measured onset energy could be compared with those previously obtained[60] for S(^{1}S) from xenon and if they are found to differ, would indicate that the source of the emission was a different metastable species.

Quantum chemistry calculations of the excited states of Ne + S(^{1}S) and excimers formed from other relevant metastable species such as O(^{1}S) would also shed light on the situation. Calculations of the emission wavelengths from these species could be compared with those measured in this experiment to determine if there is any correspondence. As in the calculations of low lying states of XeS[145] and ArS[146], these would need to be conducted

at the CASSCF level, which involves significant computational resources and a rigorous theoretical treatments. However, these would also aid future research with solid neon layers by providing a guide for which excimers can be observed within a given spectral range.

8.5 Conclusion

Electron-impact dissociation of OCS was examined using a solid neon detector. Production of $S(^1D)$ was not observed, likely because the excimer emissions were beyond the wavelength range of the PMT detector. However, a metastable feature was observed in the ultraviolet near 340 nm. While the species which was detected could not be identified TOF and kinetic energy spectra for this feature are presented but excitation functions could not be obtained. Possible explanations for this ultraviolet feature are suggested along with further experiments which would aid in determining its origin.

Chapter 9

Production of O(^{1}S) and CO($a^3\Pi$) in Electron Impact on Methanol

Electron alcohol collisions play an important role in a wide variety of settings including astrophysics and radiation biology. Methanol in particular has been observed to play an important role in a variety of astrophysical environments. Spectral lines from methanol have been shown to appear in cold dark clouds[150], the warm gas regions around newborn stars[151], in galactic cores[152] and plays a role in cometary processes[153].

An understanding of electron interactions with methanol also has important biological considerations. Nearly two decades ago, Boudaiffa *et al.*[154] showed that dissociative electron attachment (DEA) could result in single and double strand breaking of DNA molecules and has stimulated renewed interest in electron collisions with biomolecules. As methanol is the simplest organic molecule containing both a hydroxyl and methyl group, it serves as a prototypical biomolecule[155] and can bridge the gap between the study of small and large molecular collisions. Furthermore, methanol can serve as an analogue to water[156] with one of the hydrogen atoms replaced with a methyl group which allows for a comparison to other measurements in water, a much simpler and widely studied molecule. As such, studies of methanol are important to our understanding of electron interactions with biomolecules.

Much of the work regarding electron-impact dissociation of methanol has been concerned with dissociative ionization collisions. Numerous measurements of the partial ionization cross sections have been reported[157–160] after dissociation of the monocation CH_3OH^+ through mass spectroscopy techniques. However, measurements of the neutral electron-impact dissociation process appear to be much more limited. One of the few available studies is by Donohue *et al.*[161] who considered the optical emission from neutral and ionized excited state fragments.

The production of metastable CO($a^3\Pi$) in electron impact of methanol has also been reported by Lepage *et al.*[11]. Using high resolution electron energy-loss spectroscopy (HREELS), they identified several ionization and DEA channels involved in production

of this state. They were also able to measure the total cross-section for production of this state over the energy range of 6 eV to 21 eV. However, to the author's knowledge there does not appear to be studies of other metastable dissociative fragments such as $O(^1S)$.

A great deal of information can also be gained from consideration of the numerous photodissociation studies in the field. Several photoionization experiments[162–165] have reported relative cross sections for a number of ion fragments through various mass spectrometry techniques. These studies include the seminal work of Burton *et al.*[163], who report absolute cross-sections for photoabsorption and photoionization processes resulting in CH_3OH^+ in addition to branching ratios for a wide range of fragments in the 6 eV to 360 eV range.

The neutral photodissociation process has also been studied extensively[166–174]. Studies at 193 nm[167, 168] have shown that the majority of dissociation pathway at this energy is due the rupture of the OH bond and CO bond stretching while about 14% of the yield could be due to cleavage of the CO bond. Investigations at 157 nm[170, 172, 173] have revealed a much more complex set of dissociation channels at this higher energy. For instance Harich *et al.*[170] found production of both atomic and molecular Hydrogen to occur.

In this chapter, electron-impact collisions are studied using a solid Xenon detector in order to understand the role metastable $O(^1S)$ and $CO(a^3\Pi)$ play in the dissociation processes. The production of $O(^1S)$ has not been previously investigated and the selective nature of the detector used in this work makes it an ideal apparatus for such studies. Furthermore, it is hoped to extend the energy range over which production of $CO(a^3\Pi)$ production is considered.

9.1 Experimental Setup

The experimental apparatus is described in Chapter 5. A crossed electron-molecular beam setup was used to produce collision fragments. High-pressure liquid chromatography (HPLC) grade methanol from OmniSolv with a stated purity of $\geq$ 99.9% was used as the target. To produce the target beam, the methanol was first loaded into a steel bottle placed under vacuum. A gaseous beam of methanol was then generated through vapour pressure. The injection pressure was maintained at less that 10.5 mtorr throughout the study to prevent loss of metastables through collisional quenching in the interaction region.

The metastable collision fragments were detected using a Xenon layer deposited on the cold finger. After forming an excimer upon impact, the fragments would decay and emit a photon which was detected by the photomultiplier tube. Filters were placed between the light pipe and the PMT in order to selectively observe radiation from a single excimer. The two observable features occurred within the range of the 340 nm bandpass filter (85 nm FWHM) and within the red. Acquisition of the TOF spectra took approximately two weeks each while the excitation functions took between one and two months each.

During acquisition of TOF spectra, electron emission currents were maintained around 4 µA. However, this was lowered to less than 1.5 µA while measuring the excitation function in order to minimize any energy shifting effects which may occur in the interaction region due to space-charge effects. In both cases, emission currents are well within the linear regime where secondary electron scattering effects can be assumed to be negligible.

In order to calibrate the energy scale of the excitation functions, an external reference gas was used. In the ultraviolet, N_2 was injected and the (0, 0) $C^3\Pi_u \rightarrow B^3\Pi_g$ transition of the Second Positive band[105] was used, which radiates at 337.1 nm and whose cross-section for this feature is strongly peaked[118, 119] at 14 eV. Calibration in the red was performed with H_2 using the onset for production of the Balmer-α line at 656.3 nm as the excitation threshold of 16.6 eV is well studied[175].

9.2 Results

Distinct metastable features were observed when measuring TOF spectra using red and 340 nm ultraviolet filters, shown in Figures 9.1 and 9.2 respectively. Constant background subtraction and Savitzky-Golay smoothing[88] have been applied to both spectra. Previ-

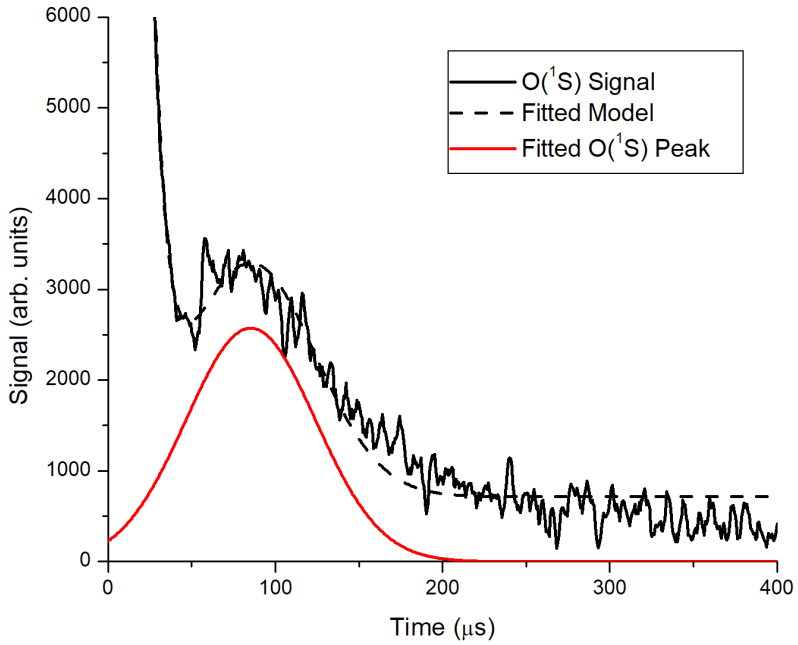

Figure 9.1: TOF spectrum of O(^1S) from electron impact of methanol at 100 eV. Savitzky-Golay smoothing has been applied to the data. Also shown with a dashed line is the fitted model of Equation 9.1 as well as the fitted Gaussian peak associated with the metastable O(^{1}S) signal which is shown below the curve with the solid line.

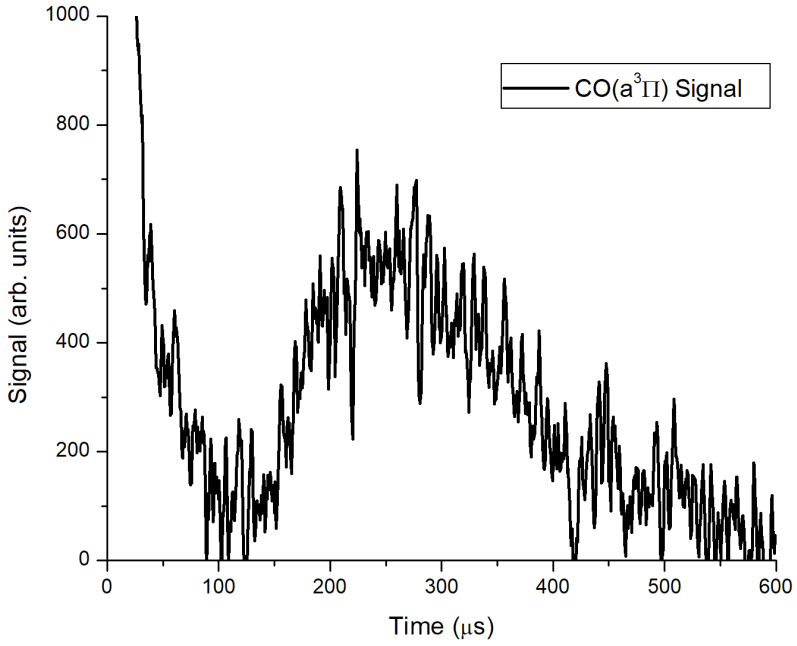

Figure 9.2: Observed TOF spectrum at 100 eV impact energy in the ultraviolet range with a 340 nm filter applied. This corresponds to signals from CO($a^3\Pi$).

ously radiation in the red from Xenon solid layers has been shown[51] and so the feature in Figure 9.1 can be concluded to correspond with radiation from O(^{1}S). On the other hand, ultraviolet light from Xenon excimers have previously been shown[56] to originate from both the O(^{1}S-^{3}P) transition and from metastable CO($a^3\Pi$). However, considering the markedly different shapes of the spectra in Figures 9.1 and 9.2, the ultraviolet emission in Figure 9.2 can be readily argued to originate from CO($a^3\Pi$) rather than a secondary O(^{1}S) emission.

As the O(^{1}S) signal in Figure 9.1 is heavily overlapped with the prompt photon peak, curve fitting was applied to separate out the metastable feature. The data were fitted assuming a Gaussian peak overlapped with an exponential decay corresponding to the function

$$f(t) = Ae^{-t/\tau} + Be^{-(t-t_o)^2/w} + C \tag{9.1}$$

Fitting was performed using SciPy's least-squares curve fitting function. The model is shown in Figure 9.1 using the dashed line while the Gaussian peak representing the O(^{1}S) metastable feature is also shown. The model appears to fit the data fairly well overall.

It may be observed that the Gaussian peak has not fully decayed at 0 µs and appears to extend to negative time values. First, it should be noted that the actual spectrum data have been shifted so that the zero index corresponds to the middle of the prompt photon peak. As such, it may be possible that some very high energy metastables are being generated

within the prompt photon peak. It is also likely that the position of the Gaussian is an indication that a more complicated model could be more accurate in fitting this spectrum. That being said, the fitted peak present in Figure 9.1 should be sufficiently representative for determining the approximate position of the majority of the O(^{1}S) metastables and for considering their energy distribution.

The CO($a^3\Pi$) spectrum in Figure 9.2 can also be considered. The feature is very broad, occupying a range of approximately 100 µs to 500 µs. The overall shape of the spectrum suggests that it is comprised of more than one feature which are overlapping and poorly resolved, partly due to low signal rates. While it may be possible to resolve these individual contributions using a smaller electron pulse width, this would also result in even lower production rates which would severely lower the signal-to-noise ratio. This ratio was already hampered by the fact that the plexiglass light pipe heavily attenuates[176] at 320 nm and the low quantum efficiency of the PMT at this wavelength [177].

In addition to the TOF distributions, one can also consider the released kinetic energy of the metastable fragments as shown in Figure 9.3. The TOF spectra were converted into the energy domain using the transform described in Appendix B.2. As the non-linear transformation tends to become obscured at lower energies due to the contribution of background counts at large time values, pretreatment of the data was necessary before applying the transform. In the case of the O(^{1}S) spectrum of Figure 9.1, both the fitted Gaussian peak and the full TOF spectrum were fit. As no fitting was applied to the CO($a^3\Pi$) data in the time domain, only points between 100 µs to 500 µs which correspond to the time region occupied by the observed feature were used to form the energy spectrum in Figure 9.3b.

When examining the kinetic energy distribution of the O(^{1}S) feature in Figure 9.3a, one can see that the distribution peaks at approximately 0.4 eV and spans from 0.1 eV and beyond 2 eV. Meanwhile, the CO($a^3\Pi$) kinetic energy distribution in Figure 9.3b can be seen to peak at much lower energies. A peak can be seen around 75 meV and the distribution extends up to about 0.4 eV. The high number of counts at extremely low energies is more likely an artefact of the non-linear transformation rather than an indication of structure.

Excitation functions were also acquired for both O(^{1}S) and CO($a^3\Pi$) shown in Figure 9.4. Low photon count rates and poor signal-to-noise ratios prevented high quality data from being obtained in both cases, likely due to very low metastable production rates in comparison to the background photon flux from the hot cathode. In the case of O(^{1}S), added difficulty was encountered by the heavy overlap of the prompt photon peak with the metastable feature. In order to prevent contamination, photon counts for the metastable feature could only be acquired in the 100 µs to 250 µs range. Due to these difficulties, the threshold region in particular is highly obscured in each scan. In order to aid in examination of the excitation functions, Savtizky-Golay smoothing[88] was applied to both figures.

The O(^{1}S) cross-section in Figure 9.4a appears to rise somewhere in the 11 eV to 15 eV range while reaching a maximum at around 40 eV and then slowly tapering off at higher

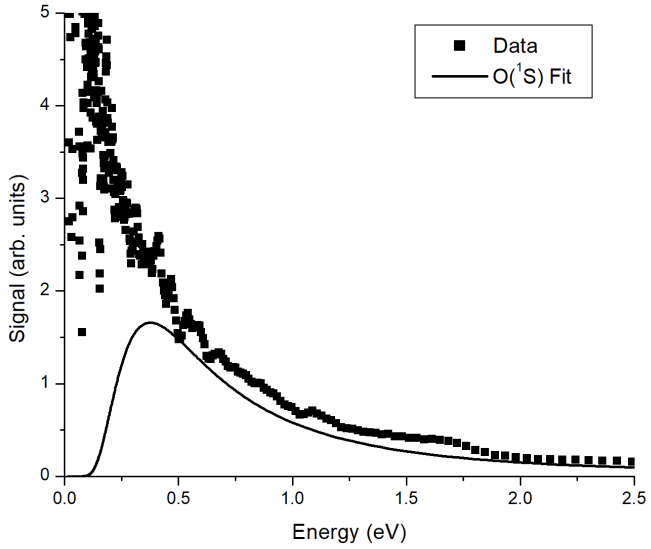

(a) $O(^1S)$

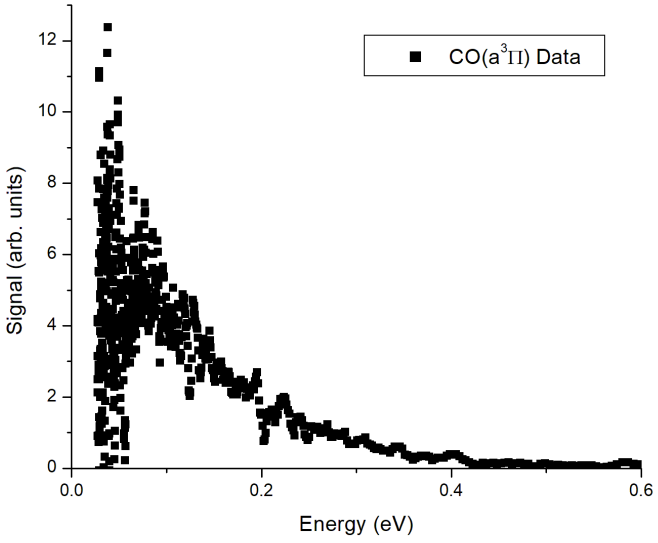

(b) $CO(a^3\Pi)$

Figure 9.3: Kinetic energy spectra for $O(^1S)$ and $CO(a^3\Pi)$ fragments from methanol at 100 eV impact energy. Savitzky-Golay smoothing[88] has been applied to both spectra after transformation into the energy domain.

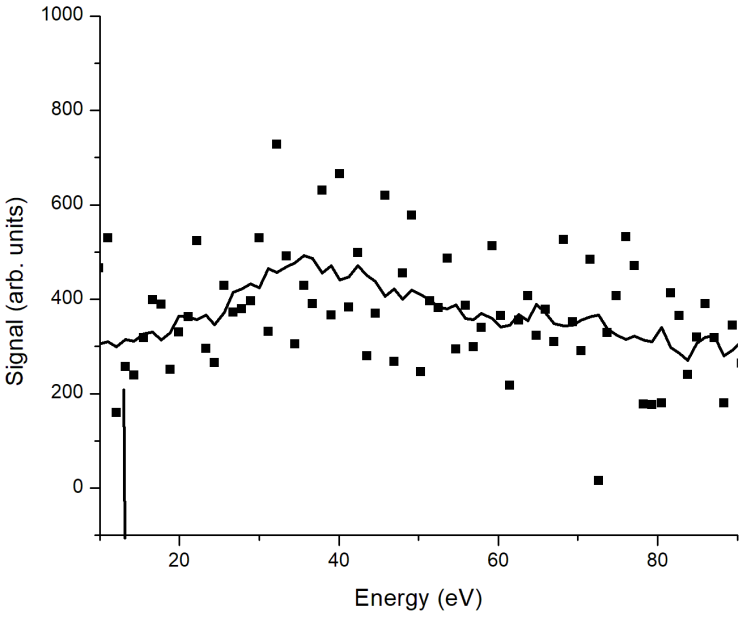

(a) O(^{1}S)

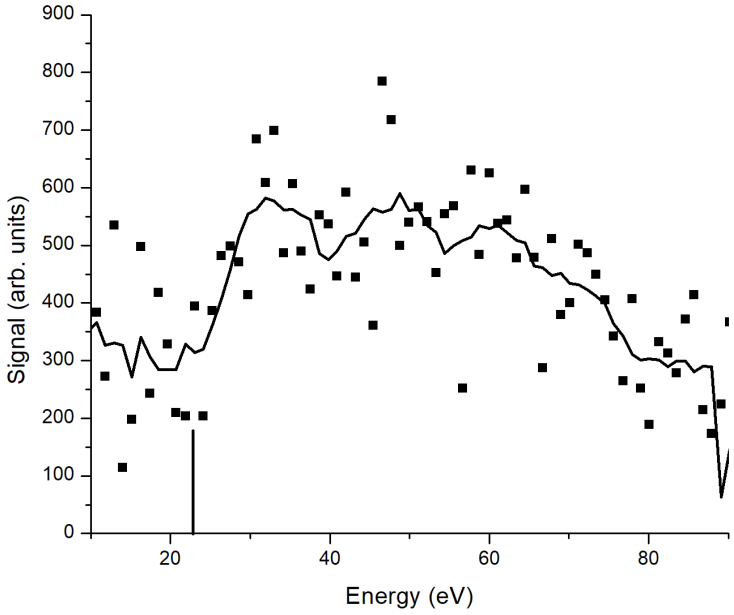

(b) CO($a^3\Pi$)

Figure 9.4: Excitation functions for O(^{1}S) and CO($a^3\Pi$) for 10 eV to 90 eV impact energy. The measured points are shown with dots while the solid line shows the excitation function after Savitzky-Golay smoothing[88] has been applied. Vertical lines denoted the suggested threshold for production of each metastable species.

energies. Meanwhile, the CO($a^3\Pi$) cross-section in Figure 9.4b appears to have an onset somewhere below 23 eV and then reaches a very broad maximum around 30 eV before very slowly tapering off. While it is certainly possible that additional structure is contained within these excitation functions, improved statistics are needed to determine it with any certainty.

9.3 Discussion

Overall, the statistical quality of the excitation functions is poorer than what is desirable. However, this is due to a very low signal-to-noise ratio rather than an insufficient data acquisition time. As such, one can conclude that the cross sections for production of both O(^{1}S) and CO($a^3\Pi$) are extremely low. This truly does speak to the power of the present technique that it can actually measurably detect such low probability events in any real capacity. At the same time, such low signal-to-noise ratios make definite determination of the thresholds for production of both species difficult. However, with the present excitation data and with aid of the kinetic energy data, it is possible to make some comments on what excitation mechanisms may or may not be occurring for each species.

As methanol is a very complex molecule, there is a very wide array of dissociation pathways which can occur. Burton *et al.*[163] have calculated the thermodynamic dissociation limits for zero kinetic energy fragments from a wide array of pathways in their comprehensive photo-dissociation studies of methanol. Their work can serve as an excellent guide for determining which pathways are energetically allowed. They also experimentally measured the appearance potentials for a number of these pathways through ion mass-spectroscopy. However, it should also be noted that other pathways which they did not observe have also been reported in the literature and so their observations are by no means a definitive list.

9.3.1 Production of O(^{1}S)

First, the total released kinetic energy upon dissociation can be considered. One can assume that the O(^{1}S) atom is travelling directly toward the detector and that the remaining fragments, some arrangement of a Carbon and three or four Hydrogen atoms, have an equal translational momentum away from the detector. As such, the released kinetic energy release of these remaining fragments is either approximately

$$E_2 \approx \frac{m_{O+H} E_1}{m_{C+3H}} \approx 1.1 E_1 \tag{9.2}$$

in the case of the Hydroxyl fragments travelling towards the detector or

$$E_2 \approx \frac{m_O E_1}{m_{C+4H}} \approx E_1 \tag{9.3}$$

if only the oxygen atoms travels in this direction. However, in both cases approximating the total translational energy to be roughly equal to twice that of the $O(^1S)$ atom is well within the accuracy achievable with the present data. From the distribution of Figure 9.3a, is most probably 0.8 eV and is at a minimum approximately 0.2 eV.

The observed production threshold of $O(^1S)$ at approximately 13 eV does place some constraints on possible excitation pathways. Dissociative ionization by first forming CH_3OH^+ is only possible[163] above 18.15 eV which rules out any of these channels. Considering the threshold observed in Figure 9.4a, the process responsible for production of $O(^1S)$ must therefore be a neutral dissociation channel.

At these energies, one possible channel exists that produces the final state

$$CH_3OH + e \rightarrow CH_3 + O(^1S) + H + e' \tag{9.4}$$

Assuming zero kinetic energy of the dissociated fragments, this process has a minimum threshold of 12.5 eV. Including the total kinetic energy of the fragments, this implies a minimum threshold of 12.7 eV and the most probably energy being 13.3 eV which would correspond to the observed threshold. A second, process would also be energetically allowed above 12.2 eV corresponding to

$$CH_3OH + e \rightarrow CH_2 + H_2 + O(^1S) + e' \tag{9.5}$$

which including the total released kinetic energy, would lead to a threshold of 12.4 eV.

There is certainly a great deal of evidence that dissociation through one of these channels is occurring. In the photodissociation measurements of Sato *et al.*[165] at 24.3 eV, they were able to observe production of O^+. Based on the thermodynamic dissociation limits[163], the only two fragmentation pathways which are energetically possible at their energy are those described in Equations 9.4 and 9.5. As other dissociative ionization studies were unable to individually resolve CH_4^+ and O^+, the latter ions would not have been reported even if they were indeed detecting these fragments.

Breaking of the CO bond by photodissociation has been observed in methanol above 6.4 eV into ground state neutral fragments by Satyapal *et al.*[167]. While the production of $O(^1S)$ in the present work implies that a higher lying excited state has been accessed, these studies certainly suggest that breakage of the CO bond is possible. Theoretical studies by Kayanuma *et al.*[178] considering the CO bond have shown that there exist several repulsive excited state curves, and while it is not possible to identify which may correspond to that observed in this work, their data does suggest that such a fragmentation mechanism is possible. The only excited state[179, 180] of OH which converges to the $O(^1S)$ + $H(^2S)$ limit is the repulsive $B^2\Sigma^-$ state. Thus, this is very likely the intermediary state to which the OH fragment is excited to during the collision event.

Based on the above arguments, the most likely dissociative pathway resulting in the

final products of Equation 9.4 is through the process

$$CH_3OH + e \rightarrow CH_3 + OH(B^2\Sigma^-) + e' \rightarrow CH_3 + O(^1S) + H(^2S) \tag{9.6}$$

Considering the low resolution of the threshold in Figure 9.4a, it may be the case that the Methyl fragment leaves with a few quanta of vibrational energy but further investigation would be required to say anything about this product of the reaction.

The reaction of Equation 9.5 cannot be ruled out but arguments can be made that it is much less probable than the process proposed in Equation 9.6. The production of H_2 has been studied by Harich *et al.*[170] who noted that production can occur through both 3-center elimination from the Methyl group and 4-center elimination of Hydrogen from both C and O sites. However, they also determined the relative branching ratio of atomic versus molecular Hydrogen elimination channels to be 1:0.21. Considering the already low excitation probability of this process, it is likely that the dominant dissociation channel is the one described in Equation 9.4a.

9.3.2 Production of CO($a^3\Pi$)

First, one can consider the implications of the kinetic energy spectrum of Figure 9.3b. For the CO fragments to travel directly towards to detector, the Hydrogen atoms originally bound to the Methyl group should travel in the opposite direction. If the Hydroxyl dissociation occurs towards the detector, then the kinetic energy of the remaining three Hydrogen should be

$$E_K \approx \frac{m_{CO+H} E_{CO}}{m_{3H}} \approx 9.6 E_{CO} \tag{9.7}$$

Assuming only 75 meV for E_{CO}, this is only about 0.7 eV. If instead the kinetics are such that all four Hydrogen move away from the detector then this ratio is lowered to

$$E_K \approx \frac{m_{CO} E_{CO}}{m_{4H}} \approx 7 E_{CO} \tag{9.8}$$

which would correspond to only 0.6 eV. This is only approximate as this neglects the motion of the Hydrogen in the plane perpendicular to the detector axis but demonstrates that the dissociation threshold should be near the thermodynamic limit. Furthermore, the deviation from this limit is on the order of the energy resolution of the excitation function and so resolving the difference in this work is not practical.

The 8 eV to 21 eV impact energy region has been extensively studied by Lepage *et al.*[11]. They noted several dissociation channels which were likely taking place especially at lower energies where DEA resonances were likely occurring. At above 25 eV, they noted that the

direct dissociative ionization channels

$$CH_3OH + e \rightarrow CH_3OH^+ + 2e \rightarrow H^+ + CO(a^3\Pi) + H_2 + H + 2e \qquad (24.87\,\text{eV}) \quad (9.9)$$

$$\rightarrow H_2^+ + CO(a^3\Pi) + H_2 + 2e \qquad (22.22\,\text{eV}) \quad (9.10)$$

were dominant. The thermodynamically determined dissociation limits are listed next to each channel. This was supported by an observed[163] rise in H^+ and H_2^+ production above 21 eV in the photodissociation data, corresponding to dissociation into ground state CO. Based on the rise in the excitation function around 23 eV in Figure 9.4b, these processes are likely responsible for the metastable signal observed in the present data.

9.4 Future Work

While a preliminary study of the production of $O(^1S)$ and $CO(a^3\Pi)$ production was performed, there is a need for data of a higher statistical quality in order to better understand the underlying excitation channels. Without accurate threshold data, an in depth study of these processes cannot be performed. These studies can be conducted with the present setup but would require significantly longer acquisition times to improve the statistics. Another alternative would be to increase the signal-to-noise ratios through modifications to the present experimental setup.

One of the issues which prevented increased count rates specifically in acquisition of the $CO(a^3\Pi)$ data was that the photon detection was not optimized for the ultraviolet photons emitted from the $XeCO^*$ excimer. In previous experiments[56], a quartz lens was placed between the cold finger and the PMT rather than a plexi-glass light pipe. While the latter increases the solid angle of detection, quartz has a better transmission efficiency for ultraviolet light[51] and installing such a lens would likely increase the photon count rates. This could be considered as a means of reducing acquisition time and improving the signal-to-noise ratio.

Improved statistics for the $CO(a^3\Pi)$ excitation function would be desirable. In their EELS study, Lepage *et al*[11] measured the absolute total cross-section for production of CO in the 8 eV to 21 eV and so it might be possible to normalize to their data, extending the measurement of the absolute cross-section up to around 100 eV.

On the other hand, the best way to improve the quality of data for the $O(^1S)$ excitation function is with longer acquisition times. The photon detection setup is optimized for studies of Xe + $O(^1S)$ excimer and so there is not much on the equipment side which can be adjusted. Increased count rates can be achieved by increasing either the electron current or the density of the target beam. However, at some point increasing either can cause additional experimental difficulties. At higher electron currents, energy shifts can be induced in the interaction region due to space charge effects which are not trivially accounted for. On the other hand, increasing the target beam density can result in collisional quenching

of the metastables before they reach the rare gas surface which prevents their detection. As such, great care must be taken to ensure these effects are not occurring if these parameters were further adjusted with the present setup.

Additional data on the production of $O(^1S)$ is even more important than for $CO(a^3\Pi)$ as the present work appears to be the first measurement of this state from methanol. As the threshold is still very uncertain, it would be of considerable interest to be able to identify the excitation channels which produce this species. While some routes of production have been suggested, accurate threshold data is required to be able to definitively assign excitation channels.

9.5 Conclusion

The production of $CO(a^3\Pi)$ and $O(^1S)$ in electron-impact dissociation of methanol was examined using a solid Xenon detector. A direct dissociation mechanism has been proposed for the production of $O(^1S)$ while previous studies of $CO(a^3\Pi)$ have been extended to 90 eV. Observation of these results goes to highlight the utility of solid rare gas layers in the detection of low probability metastable state excitation processes. Even with such small cross sections for production, the use of solid layers as a detector allows for very selective isolation of these particular metastable species while essentially filtering out all of the other possible excitation channels. Experiments like this demonstrate the true power of the technique to be sensitive to processes which would otherwise be extremely difficult to measure through more traditional methods.

Chapter 10

Conclusion

In this work, the detection of metastable atoms has been extended on three major fronts. First, the range of solid surfaces which are sensitive to $O(^1S)$ and other metastable species has been expanded. Second, the detection of a new metastable species, namely $N(^2P)$, has been performed with solid xenon layers. Finally, measurements of $O(^1S)$ production in methanol have been presented for the first time. This work at the same time also raises some questions of scientific interest which, while not fully answered, are interesting avenues to explore in future scientific research.

The results of Chapter 6 demonstrate that CO_2 is also a suitable surface for the detection of $O(^1S)$ and $O(^1D)$ in the optical range. It has been demonstrated that excimer formation occurs on these solid surfaces likely through a O + CO_2 reaction to form a CO_3 excimer. The $O(^1D)$ excimer has been studied in the literature and provides a likely explanation for the observed emissions. This work demonstrates that a similar reaction with $O(^1S)$ may also occur. While no studies of the latter are available, the experiments presented here provide an approximate emission wavelength and radiative lifetime for this state, which would be of interest in future studies of this system. Furthermore, measurements of the sensitivity of solid CO_2 layers have been obtained over a temperature range of 17.8 K to 45 K. This work demonstrates that solid CO_2 can be used as an alternative layer for the detection of metastable oxygen which may be more cost effective than traditional rare gas layers.

Solid CO_2 and N_2O have also been found to be sensitive to metastable $N_2(a^1\Pi_g)$ which react with this species through an energy transfer mechanism. These results are summarized along with all available work on detection of metastables with frozen gas layers to provide an easy reference for future research to determine a suitable layer for the detection of a particular metastable species for future experiments.

In Chapter 7 studies of $N(^2P)$ production from N_2 are presented. While this metastable state has been observed in solid nitrogen in previous studies, this is the first reported detection of metastable atomic nitrogen using solid xenon surfaces. In this study, two groups of metastable atoms were detected with two distinct kinetic energies upon release. While the faster group could not be studied due to its proximity to the prompt photon

peak, excitation studies were performed of the slower group. Two dissociation mechanisms were found to be responsible for formation of these metastables which correspond to a direct and a pre-dissociation process. Intermediary products for both reaction channels have been proposed and discussed. Possible parent states have also been proposed which led to formation of the faster metastable atoms.

Investigations into electron-impact dissociation of OCS are reported in Chapter 8. While the goal of observing S(^{1}D) production could not be achieved as the emission was outside of the spectral range of the PMT, some interesting results were obtained, which certainly could warrant further study. It was determined that the excimer formed from S(^{1}S) in solid neon likely radiates at a much shorter wavelength than the gas phase transition. This is quite atypical of radiation from solid rare gas layers which have been observed to red shift the radiation of metastable species when forming a bound state on the surface. As such, understanding the results would require further study on one or more fronts which will be outlined in Section 10.1.

Production of metastable O(^{1}S) and CO($a^3\Pi$) in dissociative electron collisions with methanol are examined in Chapter 9. This work reports what appear to be the first observations of O(^{1}S) from this molecule and extends a previous study of production of CO($a^3\Pi$). TOF and released kinetic energy spectra are reported for each species in addition to cross section measurements in the 10 eV to 90 eV range. Low signal-to-noise ratios prevented high detail studies but it was revealed that O(^{1}S) is likely produced through a single direct dissociation channel after breakage of the CO bond.

Throughout these experiments, it has been demonstrated that this method is an extremely powerful tool for measuring metastable production in electron-impact collisions. While excitation of these states occurs with very low probability in comparison to other optically allowed excitation and dissociation channels, the solid layer detectors used in this work are able to measure these very specific excitation pathways while being insensitive to the multitude of other excited states that are also being produced. As such, it has a wide application to the study of species which would otherwise be extremely difficult to isolate and study through more traditional optical or electron energy loss methods.

10.1 Future Work

There is a great deal of future work which can be done to extend the results and conclusions obtained in the present studies. While each of the experiments has contributed to our understanding of these poorly understood metastable production channels, there is certainly much more that can be done in each area of study to further our knowledge and understanding of these phenomena.

Studies of what solid layers are sensitive to particular metastable species are by no means comprehensive. While this and previous studies have done a great deal of work determining

the sensitivity of solid rare gas and atmospheric gas layers to metastable species, there remains some gaps in the understanding of the chemistry occurring at these surfaces. In particular, studies of the $O(^1S) + CO_2$ reaction would be of particular use. While a reaction pathway for the reaction of $O(^1D) + CO_2$ exists in the literature, there appear to be no studies associated with the $O(^1S)$ reactant. As such, quantum chemistry calculations would be of particular use in determining the route taken to form CO_3 on the surface in this experiment. The emission wavelengths and excimer lifetime estimates which have been provided in this work would be of utility in verifying these theoretical models and improving our understanding of the CO_3 system.

In addition to understanding the reaction, there remains work to be done in characterizing this surface. It would be of interest to determine the conversion efficiency of CO_2 when forming excimers with metastable oxygen. Studies of $O(^1D)$ have been known[51] to take considerable acquisition time due to the lowered efficiency of solid rare-gas layers relative to $O(^1S)$ and any opportunity for improvement would certainly be welcome in future studies of this metastable state.

As the primary goal of observing $S(^1D)$ production using solid neon layers was not accomplished, it may be desirable to examine production of this metastable species using a modified experimental apparatus. Given that $O(^1D)$ has been observed using solid rare gas layers and that $S(^1D)$ is isoelectronic with the former state, it is likely that the radiation was simply at a longer wavelength that our present PMT is blind to. Replacement of the PMT with another detector such as an avalanche photodiode that is sensitive to the IR would be a possible candidate. Using such a detector, observation of this state would be likely and measurements of $S(^1D)$ production could then be performed. This would also bring about added difficulties however as APDs typically have very small surface areas in comparison to PMTs resulting in a significantly reduced solid angle of detection which would drastically reduce count rates. Any studies involving OCS would also require the use of an improved vacuum system which is better suited to corrosive gases.

Given that the source of the ultraviolet emission observed from dissociation of OCS using solid neon was not definitively identified, it would also be of interest to conduct further study to determine the radiation source. Several possible explanations have been provided in Chapter 8 such as emission from a different metastable species. Metastable oxygen states such as $O(^5S)$ could be detected from electron-impact dissociation of less corrosive gases such as CO_2 or O_2 and so these could be candidate gases to study for production of this state. Excitation functions could also be obtained to determine the production threshold which would provide a better understanding of the radiation source.

Finally, additional measurements of electron-impact dissociation of methanol are needed to fully understand the reactions which have been observed to occur. As poor signal to noise ratios prevented higher count rates in the reported cross section measurements, there reaches a point of diminishing returns from additional acquisition using the present apparatus. As

such, more detailed study of methanol may not be desirable. Study of other alcohols such as ethanol may be of interest however. It is very likely that the production of both $O(^1S)$ and $CO(a^3\Pi)$ is present in these larger molecules. An understanding of the similarities and differences between the alcohols would at the very least provide additional data for the biological interests that electron collisions with these organic molecules is based upon, furthering our understanding of the role this type of scattering plays in larger biomolecules. Furthermore, it may provide insight into the kinetics of the fragmentation process that leads to production of these metastable states in the alcohols.

Appendices

Appendix A

Scientific Constants and Data

Table A.1: Table of relevant scientific constants. Data taken from CODATA recommended values[181].

Quantity	Symbol	Value	Units
Speed of light in a vacuum	c	299 792 458	m/s
Electron volt	eV	$(1.602\,176\,565 \pm 0.000\,000\,035) \times 10^{-28}$	J
Planck's constant	h	$(6.626\,069\,57 \pm 0.000\,000\,29) \times 10^{-34}$ $(4.135\,667\,516 \pm 0.000\,000\,091) \times 10^{-15}$	J s eV s
Reduced Planck's constant ($h/2\pi$)	$\hbar$	$(1.054\,571\,726 \pm 0.000\,000\,047) \times 10^{-34}$ $(6.582\,119\,28 \pm 0.000\,000\,15) \times 10^{-16}$	J s eV s
Boltzmann's constant	k_B	$(1.380\,648\,8 \pm 0.000\,001\,3) \times 10^{-23}$ $(8.617\,332\,4 \pm 0.000\,007\,8) \times 10^{-5}$	J/K eV/K
Elementary charge	e	$(1.602\,176\,565 \pm 0.000\,000\,035) \times 10^{-19}$	C
Angstrom	Å	1×10^{-10}	m
Mass of the electron	m_e	$(9.109\,382\,91 \pm 0.000\,000\,40) \times 10^{-31}$	kg
Atomic mass constant ($\frac{1}{12}$m(^{12}C))	m_u	$(1.660\,538\,921 \pm 0.000\,000\,073) \times 10^{-27}$	kg
Torrent	torr	101 325/760	Pa

Table A.2: Table of relevant atomic scale units and constants. Numerical values taken from CODATA recommended values[181].

Quantity	Symbol	Definition	Value
Bohr Radius	a_o	$\frac{\hbar^2}{m_e e^2}$	$0.529\,18 \times 10^{-8}$/cm
Bohr Magneton	μ_B	$\frac{e\hbar}{2m_e}$	$9.274\,009 \times 10^{-24}$ J/T
Rydberg Energy	R	$\frac{m_e e^4}{2\hbar^2}$	13.606 eV
Fine-structure Constant	α	$\frac{1}{4\pi\epsilon_o}\frac{e^2}{\hbar c}$	0.007 297 352

Table A.3: Table of ionization energies of relevant atoms and molecules. Data taken from the CRC Handbook[89].

Element	Ionization Energy (eV)
H	13.598443
C	11.26030
O	13.61805
CH	10.64
CH_2	10.396
CH_3	9.843
CH_3OH	10.846

Appendix B

Relevant Transforms

B.1 Energy Unit Conversions

In this work, several units of energy are used which are more representative of the scales used in this work and provide added convenience. Specifically, it is of great utility to express many quantities relevant to atomic collisions in units of electron volts rather than joules. In addition, when working with optical processes it is convenient to talk in term's of the photon wavelength rather than providing a direct energy value. In this section, we outline how to convert between joules and electron volts or photon wavelengths.

The electron volt (eV) is defined as the amount of energy gained by a single electron travelling across a potential difference of one volt. One can compute the energy in joules by considering that a 1 V field can equivalently be written as 1 J/C and the energy of an electron passing through this potential can be found by multiplying by the fundamental charge 1.602×10^{-19} C. Therefore, an electron volt is related to a joule by

$$1\,\mathrm{eV} = 1.602 \times 10^{-19}\,\mathrm{J} \tag{B.1}$$

A more accurate value for the fundamental charge e is provided in Appendix A.1.

When dealing with photons, one can also represent its' energy in several units which are convenient in a variety of contexts. However, the majority make use of the Planck relation

$$E = h\nu = \hbar\omega \tag{B.2}$$

Therefore, one can readily express a photon's energy in terms of its frequency or wavelength. In this work, we make extensive use of the latter relationship. Given that a photon, which travels at the speed of light c has a frequency/wavelength relationship determined by

$$c = \lambda\nu \tag{B.3}$$

Therefore, one can determine the photon energy from the wavelength using the formula

$$E = \frac{hc}{\lambda} \tag{B.4}$$

B.2 Time-of-Flight to Energy Distribution

When one has a time-of-flight spectrum in collision experiments, it is in some cases useful to examine the energy distribution of the collision products. As the time and energy domain have a non-linear dependence, the transformation between the two has the effect of emphasizing different parts of the spectrum which may be useful in analysis. The method for conducting such a transformation has previously been outlined by Smyth *et al.*[87] and an overview of the procedure is given below.

If one has a time domain distribution $f(t)$ and wishes to determine the corresponding function over the energy $F(E)$ one can start by considering the spectral density in the equivalent intervals of the time and energy domain

$$F(t)\ dt = F(E)\ dE \tag{B.5}$$

Time and energy are related by the equation

$$E = \frac{m}{2}\frac{D^2}{t^2} \tag{B.6}$$

One can then take the derivative of this relation

$$\frac{dE}{dt} = -\frac{mD^2}{2}\left(-2t^{-3}\right) = -\frac{mD^2}{t^3} \tag{B.7}$$

Equation B.5 can then be rearranged in terms of this derivative

$$F(E) = f(t)\left|\frac{dt}{dE}\right| \tag{B.8}$$

Which determine the final transform from time to the energy domain

$$F(E) = \frac{t^3}{mD^2} f(t) \tag{B.9}$$

One can also consider the effect of uncertainty in the time position has on the energy. If one has a time uncertainty Δt, then one can determine the corresponding energy uncertainty from

$$(\Delta E)^2 = \left(\frac{\partial E}{\partial t}\right)^2 (\Delta t)^2 \tag{B.10}$$

assuming that all other factors are known with certainty. Then, applying the derivative of

(B.7) one has

$$(\Delta E)^2 = \left(\frac{mD^2}{t^3}\right)^2 (\Delta t)^2 = \left(\frac{2E}{t}\right)^2 (\Delta t)^2 \tag{B.11}$$

Assuming that these are all positive definite quantities, one can then relate the relative errors in the time and energy domain by the equation

$$\frac{\Delta E}{E} = \frac{2\Delta t}{t} \tag{B.12}$$

B.3 Maxwell-Boltzmann Time-of-Flight Distribution

In the section, we derive the time-of-flight distribution for a gas possessing a Maxwell-Boltzmann distribution of speeds travelling a fixed distance. In this work, gas samples move from the collision region to the detector through a fixed distance. Knowing the length of the drift tube, the particle mass and the sample temperature, one can relate the flight times to the Maxwell-Boltzmann distribution of speeds through a simple relationship.

The Maxwell-Boltzmann distribution of speeds is given by

$$f(v) = \left(\frac{m}{2\pi k_B T}\right)^{3/2} 4\pi v^2 \exp\left(-\frac{mv^2}{2k_B T}\right) \tag{B.13}$$

We wish to determine the TOF distribution for particles travelling a fixed distance D. The TOF and velocity distributions occupy equal differential elements

$$F(t)dt = f(v)dv = f(v)\left|\frac{dv}{dt}\right| dt \tag{B.14}$$

which are related by the derivative

$$\frac{dv}{dt} = \frac{d}{dt}\left(\frac{D}{t}\right) = -\frac{D}{t^2} \tag{B.15}$$

Therefore the TOF distribution for a sample of particles of mass m and temperature T is determined by

$$F(t) = \left(\frac{m}{2\pi k_B T}\right)^{3/2} \frac{4\pi D^3}{t^4} \exp\left(\frac{-mD^2}{2k_B T t^2}\right) \tag{B.16}$$

Appendix C

Wigner-Eckart Theorem

The Wigner-Eckart is a powerful tool for determining the effect of vector operators on angular momentum eigenstates. For a rank k tensor $T_q^{(k)}$ operator acting on angular momentum states $|\alpha;\ j,m\rangle$, the matrix elements of the tensor operator are given by

$$\langle \alpha';\ j',m'|T_q^{(k)}|\alpha;\ j,m\rangle = \langle jk;\ mq|jk;\ j'm'\rangle \frac{\langle \alpha';\ j'\|T^{(k)}\|\alpha;\ j\rangle}{\sqrt{2j+1}} \tag{C.1}$$

There are two very important implications of this results. First, the matrix elements can be written in terms of a reduced matrix element $\langle \alpha';\ j'\|T^{(k)}\|\alpha;\ j\rangle$ which is *independent* of m and m'. Second, the dependence on m is completely described by the associated Clebsh-Gordan coefficient

$$C^{jm}_{kqj'm'} = \langle jk;\ mq|jk;\ j'm'\rangle \tag{C.2}$$

for adding momentum j and k to get j'.

Often when working with angular momentum states, it is useful to use the Wigner j symbols. The Wigner $3-j$ symbol can be connected to the Clebsch-Gordan coefficients through the relationship

$$\begin{pmatrix} j_1 & j_2 & j_3 \\ m_1 & m_2 & m_3 \end{pmatrix} \equiv \frac{(-1)^{j_1-j_2-m_3}}{\sqrt{2j_3+1}} C^{j_1,m_1}_{j_2,m_2,j_3,m_3} \tag{C.3}$$

The Wigner $3-j$ symbols obey a set of selection rules. The symbol will be zero unless

$$m_1 + m_2 + m_3 = 0 \tag{C.4a}$$

$$j_1 + j_2 + j_3 = n \tag{C.4b}$$

$$|m_i| \leq j_i \tag{C.4c}$$

$$|j_1 - j_2| \leq j_3 \leq j_1 + j_2 \tag{C.4d}$$

where n is an integer. Furthermore, if $m_1 = m_2 = m_3 = 0$, n must be an even integer.

The Wigner $6-j$ symbol can also be used when working with multiple momentum basis.

The symbols is defined as a summation over the $3j$-symbols

$$\begin{Bmatrix} j_1 & j_2 & j_3 \\ j_4 & j_5 & j_6 \end{Bmatrix} = \sum_{m_i} (-1)^S \begin{pmatrix} j_1 & j_2 & j_3 \\ m_1 & m_2 & -m_3 \end{pmatrix} \begin{pmatrix} j_1 & j_5 & j_6 \\ -m_1 & m_5 & m_6 \end{pmatrix} \times \begin{pmatrix} j_4 & j_5 & j_3 \\ m_4 & -m_5 & m_3 \end{pmatrix} \begin{pmatrix} j_4 & j_2 & j_6 \\ -m_4 & -m_2 & -m_6 \end{pmatrix} \quad \text{(C.5)}$$

where the phase factor is summed over the 6 m values

$$S = \sum_{k=1}^{6} (j_k - m_k) \quad \text{(C.6)}$$

The value of the $6-j$symbol is zero unless $|j_2 - j_3| \leq j_1 \leq j_2 + j_3$.

Bibliography

[1] J. Polanyi and P. Young, "Photochemistry of adsorbed molecules. vii. ultraviolet photoejection and photodesorption of ocs on lif(001)," *The Journal of chemical physics*, vol. 93, no. 5, p. 3673, 1990.

[2] Y. Hiraki, L. Tong, H. Fukunishi, K. Nanbu, Y. Kasai, and A. Ichimura, "Generation of metastable oxygen atom o(^{1}d) in sprite halos," *Geophysical research letters*, vol. 31, no. 14, 2004.

[3] B. Sharpee and T. Slanger, "O(^{1}d$_2$-^{3}p2, 1, 0) 630.0, 636.4, and 639.2 nm forbidden emission line intensity ratios measured in the terrestrial nightglow," *The Journal of Physical Chemistry A*, vol. 110, no. 21, p. 6707, 2006.

[4] J. R. Lyons, "Transfer of mass-independent fractionation in ozone to other oxygen-containing radicals in the atmosphere," *Geophysical Research Letters*, vol. 28, no. 17, p. 3231, 2001.

[5] M. Baasandorj, E. L. Fleming, C. H. Jackman, and J. B. Burkholder, "O(^{1}d) kinetic study of key ozone depleting substances and greenhouse gases," *The Journal of Physical Chemistry A*, vol. 117, no. 12, p. 2434, 2013.

[6] T. Slanger, P. Cosby, D. Huestis, and T. Bida, "Discovery of the atomic oxygen green line in the venus night airglow," *Science*, vol. 291, no. 5503, p. 463, 2001.

[7] A. Bhardwaj and S. Haider, "Chemistry of o(^{1}d) atoms in the coma: Implications for cometary missions," *Advances in Space Research*, vol. 29, no. 5, p. 745, 2002.

[8] D. L. Huestis, T. G. Slanger, B. D. Sharpee, and J. L. Fox, "Chemical origins of the mars ultraviolet dayglow," *Faraday discussions*, vol. 147, p. 307, 2010.

[9] J. T. Herron, "Evaluated chemical kinetics data for reactions of n(^{2}d), n(^{2}p), and n$_2$($a^3\Sigma_u^+$) in the gas phase," *Journal of Physical and Chemical Reference Data*, vol. 28, no. 5, p. 1453, 1999.

[10] S. Rochkind and G. E. Ouaknine, "New trend in neuroscience: Low-power laser effect on peripheral and central nervous system (basic science, preclinical and clinical studies)," *Neurological research*, vol. 14, no. 1, p. 2, 1992.

[11] M. Lepage, M. Michaud, and L. Sanche, "Low energy electron total scattering cross section for the production of co within condensed methanol," *The Journal of chemical physics*, vol. 107, no. 9, p. 3478, 1997.

[12] R. Sensenig, S. Kalghatgi, E. Cerchar, G. Fridman, A. Shereshevsky, B. Torabi, K. P. Arjunan, E. Podolsky, A. Fridman, G. Friedman, *et al.*, "Retracted article: Non-thermal plasma induces apoptosis in melanoma cells via production of intracellular reactive oxygen species," *Annals of biomedical engineering*, vol. 39, no. 2, p. 674, 2011.

[13] C. Chen, D. Liu, Z. Liu, A. Yang, H. Chen, G. Shama, and M. Kong, "A model of plasma-biofilm and plasma-tissue interactions at ambient pressure," *Plasma Chemistry and Plasma Processing*, vol. 34, no. 3, p. 403, 2014.

[14] H. Cheng, X. Liu, X. Lu, and D. Liu, "Numerical study on propagation mechanism and bio-medicine applications of plasma jet," *High Voltage*, vol. 1, no. 2, p. 62, 2016.

[15] Y. He, Y. Inamori, M. Mizuochi, H. Kong, N. Iwami, and T. Sun, "Nitrous oxide emissions from aerated composting of organic waste," *Environmental Science & Technology*, vol. 35, no. 11, p. 2347, 2001.

[16] C. Simon, O. Witasse, F. Leblanc, G. Gronoff, and J.-L. Bertaux, "Dayglow on mars: Kinetic modelling with spicam uv limb data," *Planetary and Space Science*, vol. 57, no. 8-9, p. 1008, 2009.

[17] A. Stiepen, J.-C. Gérard, S. Bougher, F. Montmessin, B. Hubert, and J.-L. Bertaux, "Mars thermospheric scale height: Co cameron and co_2^+ dayglow observations from mars express," *Icarus*, vol. 245, p. 295, 2015.

[18] Y. Itikawa and A. Ichimura, "Cross sections for collisions of electrons and photons with atomic oxygen," *Journal of Physical and Chemical Reference Data*, vol. 19, no. 3, p. 637, 1990.

[19] R. Gilpin and K. Welge, "Time-of-flight spectroscopy of metastable photodissociation fragments. n_2o dissociation in the vacuum uv," *The Journal of Chemical Physics*, vol. 55, no. 2, p. 975, 1971.

[20] G. Allcock and J. McConkey, "Dissociation patterns in n_2o following electron impact," *Chemical Physics*, vol. 34, no. 2, p. 169, 1978.

[21] N. Mason, "Measurement of the lifetime of metastable species by electron impact dissociation of molecules," *Measurement Science and Technology*, vol. 1, no. 7, p. 596, 1990.

[22] E. Stone, G. Lawrence, and C. Fairchild, "Kinetic energies and angular distributions of oxygen atom photofragments produced by photodissociation of o_2 and n_2o in the vacuum ultraviolet," *The Journal of Chemical Physics*, vol. 65, no. 12, p. 5083, 1976.

[23] J. C. McLennan and G. Shrum, "On the origin of the auroral green line 5577 å, and other spectra associated with aurora borealis," *Proceedings of the Royal Society of London. Series A, Containing Papers of a Mathematical and Physical Character*, vol. 108, no. 747, p. 501, 1925.

[24] C. Kenty, J. Aicher, E. Noel, A. Poritsky, and V. Paolino, "A new band system in the green excited in a mixture of xenon and oxygen and the energy of dissociation of co," *Physical Review*, vol. 69, p. 36, 1946.

[25] R. Herman and L. Herman, "Emission of dilute oxygen in an atmosphere of xenon," *Journal de Physique et le Radium*, vol. 11, p. 69, 1950.

[26] C. D. Cooper, G. Cobb, and E. Tolnas, "Visible spectra of xeo and kro," *Journal of Molecular Spectroscopy*, vol. 7, no. 1-6, p. 223, 1961.

[27] D. Cunningham and K. Clark, "Rates of collision-induced emission from metastable o(^{1}s) atoms," *The Journal of Chemical Physics*, vol. 61, no. 3, p. 1118, 1974.

[28] D. Huestis, R. Gutcheck, R. Hill, M. McCusker, and D. Lorents, "Studies of e-beam pumped molecular lasers," STANFORD RESEARCH INST MENLO PARK CA, Tech. Rep., 1975.

[29] J. Simmons, A. Maki, and J. Hougen, "Spectroscopic analysis of the $d^1\Sigma^+ \rightarrow a^1\Sigma^+$ and $d^1\Sigma^+ \rightarrow b^1\Pi$ green band systems of xeo," *Journal of Molecular Spectroscopy*, vol. 74, no. 1, p. 70, 1979.

[30] V. E. Bondybey, A. M. Smith, and J. Agreiter, "New developments in matrix isolation spectroscopy," *Chemical reviews*, vol. 96, no. 6, p. 2113, 1996.

[31] L. Vegard and G. Kvifte, "The green auroral line as an initiator of phosphorescence in condensed systems," *Nature*, vol. 162, no. 4129, p. 967, 1948.

[32] L. Schoen and H. Broida, "Spectra emitted from rare gas-oxygen solids during electron bombardment," *The Journal of Chemical Physics*, vol. 32, no. 4, p. 1184, 1960.

[33] C. Girardet, D. Maillard, and J. Fournier, "Deexcitation time shortening for the electronic states of trapped oxygen by matrix doping. i. theoretical aspects," *The Journal of chemical physics*, vol. 84, no. 8, p. 4429, 1986.

[34] A. Belov, I. Y. Fugol, E. Yurtaeva, and O. Bazhan, "Luminescence of oxygen-rare gas exciplex compounds in rare gas matrices," *Journal of luminescence*, vol. 91, no. 1-2, p. 107, 2000.

[35] A. Belov and E. Yurtaeva, "Xenon excimer compounds with oxygen in inert-gas crystal matrices," *Low Temperature Physics*, vol. 27, no. 11, p. 938, 2001.

[36] J. Goodman, J. Tully, V. Bondybey, and L. Brus, "Excited state spectroscopy, subpicosecond predissociation, and solvation of diatomic xeo in solid rare gas hosts," *The Journal of Chemical Physics*, vol. 66, no. 11, p. 4802, 1977.

[37] R. Taylor and W. Walker, "Photoluminescence of aro and kro in doped rare-gas matrices," *The Journal of Chemical Physics*, vol. 70, no. 1, p. 284, 1979.

[38] ——, "Photoluminescence of ars, krs, and xes in rare-gas matrices," *Applied Physics Letters*, vol. 35, no. 5, p. 359, 1979.

[39] R. Taylor, W. Walker, K. Monahan, and V. Rehn, "Photodissociative production of o(^{1}s) from n_2o and s(^{1}s) from ocs in rare gas matrices," *The Journal of Chemical Physics*, vol. 72, no. 12, p. 6743, 1980.

[40] R. Taylor, W. Scott, P. Findley, Z. Wu, W. Walker, and K. Monahan, "Matrix interactions with rare-gas oxide excimers," *The Journal of Chemical Physics*, vol. 74, no. 7, p. 3718, 1981.

[41] J. Fournier, H. Mohammed, J. Deson, and D. Maillard, "Vacuum uv photolysis of co2. rare-gas oxide formation in matrices," *Chemical Physics*, vol. 70, no. 1-2, p. 39, 1982.

[42] D. Maillard, J. P. Perchard, J. Fournier, H. H. Mohammed, and C. Girardet, "Rare-gas oxide excimers in matrices," *Chemical Physics Letters*, vol. 86, no. 4, p. 420, 1982.

[43] D. Maillard, J. Fournier, H. H. Mohammed, and C. Girardet, "Crystal-split electronic states of an atom in a rare gas crystal. calculation of the absorption and fluorescence spectra of trapped oxygen (^{3}p, ^{1}d, ^{1}s) atoms," *The Journal of chemical physics*, vol. 78, no. 9, p. 5480, 1983.

[44] W. Lawrence and V. Apkarian, "Electronic spectroscopy of oxygen atoms trapped in solid xenon," *The Journal of chemical physics*, vol. 97, no. 4, p. 2229, 1992.

[45] W. Kedzierski, E. Blejdea, A. DiCarlo, and J. McConkey, "Metastable oxygen atom detection using rare gas matrices," *Journal of Physics B: Atomic, Molecular and Optical Physics*, vol. 43, no. 8, p. 085 204, 2010.

[46] H. Kiefl, E. Karl, and J. Fricke, "Cross section measurements with selectively detected o(^{1}s) beam atoms," *Journal of Physics B: Atomic and Molecular Physics*, vol. 16, no. 22, p. 4165, 1983.

[47] L. R. LeClair and J. McConkey, "Selective detection of o($^1s_0$) following electron impact dissociation of o2 and n_2o using a xeo* conversion technique," *The Journal of chemical physics*, vol. 99, no. 6, p. 4566, 1993.

[48] J. J. Corr, "Metastable fragment production following electron impact on sulfur hexafluoride and oxygen.," 1987.

[49] J. Corr, M. Khakoo, A. McConkey, and J. McConkey, "Excitation of metastable fragments following electron impact on o_2," *Bulletin of the American Physical Society*, vol. 33, p. 139, 1988.

[50] T. H. Dunning Jr and P. J. Hay, "Low-lying electronic states of the rare gas oxides," *The Journal of Chemical Physics*, vol. 66, no. 8, p. 3767, 1977.

[51] J. W. McConkey and W. Kedzierski, "Detection of metastable atoms and molecules using rare gas matrices," in *Advances In Atomic, Molecular, and Optical Physics*, vol. 63, Elsevier, 2014, p. 1.

[52] L. R. LeClair, "Production and detection of metastable atomic oxygen(ph. d. thesis)," 1993.

[53] L. LeClair, J. Corr, and J. McConkey, "Production of o(^{1}s) from n_2o by electron impact," *Journal of Physics B: Atomic, Molecular and Optical Physics*, vol. 25, no. 24, p. L647, 1992.

[54] J. Derbyshire, W. Kedzierski, and J. McConkey, "New dissociation channels in d_2o," *Physical review letters*, vol. 79, no. 12, p. 2229, 1997.

[55] W. Kedzierski, J. Derbyshire, C. Malone, and J. McConkey, "Isotope effects in the electron impact break-up of water," *Journal of Physics B: Atomic, Molecular and Optical Physics*, vol. 31, no. 24, p. 5361, 1998.

[56] L. R. LeClair and J. McConkey, "On o(^{1}s) and co($a^3\Pi$) production from electron impact dissociation of co_2," *Journal of Physics B: Atomic, Molecular and Optical Physics*, vol. 27, no. 17, p. 4039, 1994.

[57] L. R. LeClair, M. D. Brown, and J. W. McConkey, "Selective detection of o(^{1}s) and co($a^3\Pi$) following electron impact on co using solid xenon," *Chemical physics*, vol. 189, no. 3, p. 769, 1994.

[58] L. R. LeClair, J. M. Derbyshire, and J. W. McConkey, "O(^{1}s) production following electron impact dissociative excitation of no," *Journal of Geophysical Research: Planets*, vol. 101, no. E3, p. 7585, 1996.

[59] W. Kedzierski, C. Malone, and J. McConkey, "Dissociative excitation of so_2 by electron impact," *Canadian Journal of Physics*, vol. 78, no. 5-6, p. 617, 2000.

[60] W. Kedzierski, J. Borbely, and J. McConkey, "Electron impact dissociation of ocs," *Journal of Physics B: Atomic, Molecular and Optical Physics*, vol. 34, no. 20, p. 4027, 2001.

[61] W. Kedzierski, E. Blejdea, A. DiCarlo, and J. McConkey, "Electron impact dissociation of n_2o and co_2 with single particle detection of o(^{1}d$_2$)," *Chemical Physics Letters*, vol. 498, no. 1-3, p. 38, 2010.

[62] W. Kedzierski, J. Hein, C. Tiessen, D. Lukic, J. Trocchi, T. Mlinaric, and J. McConkey, "Production of o(^{1}d) following electron impact on co_2," *Canadian Journal of Physics*, vol. 91, no. 12, p. 1044, 2013.

[63] W. Kedzierski and J. McConkey, "Use of solid n_2 surfaces in metastable particle detection," *Review of Scientific Instruments*, vol. 87, no. 12, p. 123 110, 2016.

[64] ——, "Selective detection of singlet gerade metastable states of n_2," *The Journal of chemical physics*, vol. 145, no. 4, p. 044 313, 2016.

[65] J. J. Sakurai and J. Napolitano, *Modern Quantum Mechanics*. 2011.

[66] R. D. Cowan, *The theory of atomic structure and spectra*, 3. Univ of California Press, 1981.

[67] E. U. Condon and H. Odabasi, *Atomic structure*. CUP Archive, 1980.

[68] W. Heitler, *The quantum theory of radiation*. Courier Corporation, 1984.

[69] H. Lefebvre-Brion and R. W. Field, *The Spectra and Dynamics of Diatomic Molecules: Revised and Enlarged Edition*. Academic Press, 2004.

[70] P. R. Bunker and P. Jensen, *Molecular symmetry and spectroscopy*. NRC Research Press, 2006.

[71] G. Herzberg, "Molecular spectra and molecular structure. vol. 1: Spectra of diatomic molecules," *New York: Van Nostrand Reinhold, 1950, 2nd ed.*, 1950.

[72] J. K. Watson, "Simplification of the molecular vibration-rotation hamiltonian," *Molecular Physics*, vol. 15, no. 5, p. 479, 1968.

[73] R. N. Zare, *Angular momentum: understanding spatial aspects in chemistry and physics*. New York, 1988.

[74] E. U. Condon, "Nuclear motions associated with electron transitions in diatomic molecules," *Phys. Rev.*, vol. 32, pp. 858–872, 6 Dec. 1928.

[75] P. F. Bernath, *Spectra of atoms and molecules*. Oxford university press, 2015.

[76] M. M. Somoza, *Franck-condon diagram*, [Online; accessed October 26, 2018], 2006. [Online]. Available: `https://upload.wikimedia.org/wikipedia/commons/0/0e/Franck-Condon-diagram.png`.

[77] E. McDaniel, *Atomic collisions: electron and photon projectiles*, ser. Atomic Collisions. Wiley, 1989, ISBN: 9780471853077.

[78] U. Fano and A. Rau, *Atomic Collisions and Spectra*. Academic Press, 1986, p. 344.

[79] I. E. McCarthy and E. Weigold, *Electron-atom collisions*. World Scientific, 1995, vol. 235.

[80] R. Hall and F. Read, "Molecular spectroscopy by electron scattering," in *Electron-Molecule Collisions*, Springer, 1984, ch. 5, p. 351.

[81] D. J. Griffiths, *Introduction to electrodynamics; 4th ed.* Boston, MA: Pearson, 2013.

[82] M. Inokuti, "Inelastic collisions of fast charged particles with atoms and molecules the bethe theory revisited," *Reviews of modern physics*, vol. 43, no. 3, p. 297, 1971.

[83] J. McConkey, "Electron-atom and electron-molecule collisions," in *Springer handbook of atomic, molecular, and optical physics*, G. W. Drake, Ed., Springer Science & Business Media, 2006, ch. 63.

[84] W. L. Borst and E. Zipf, "Energy spectra of metastable oxygen atoms produced by electron-impact dissociation of o_2," *Physical Review A*, vol. 4, no. 1, p. 153, 1971.

[85] P. Cosby, "Electron-impact dissociation of nitrogen," *The Journal of chemical physics*, vol. 98, no. 12, p. 9544, 1993.

[86] C. Walter, P. C. Cosby, and H. Helm, "Predissociation quantum yields of singlet nitrogen," *Physical Review A*, vol. 50, no. 4, p. 2930, 1994.

[87] K. C. Smyth, J. A. Schiavone, and R. S. Freund, "Dissociative excitation of n_2 by electron impact: Translational spectroscopy of long-lived high-rydberg fragment atoms," *The Journal of Chemical Physics*, vol. 59, no. 10, p. 5225, 1973.

[88] S. J. Orfanidis, *Introduction to signal processing*. Prentice-Hall, Inc., 1995.

[89] W. M. Haynes, *CRC handbook of chemistry and physics*. CRC press, 2014.

[90] D. Bogard, R. Clayton, K. Marti, T. Owen, and G. Turner, "Martian volatiles: Isotopic composition, origin, and evolution," in *Chronology and evolution of Mars*, Springer, 2001, p. 425.

[91] Y. L. Yung and W. B. DeMore, *Photochemistry of planetary atmospheres*. Oxford University Press, 1998.

[92] V. Moroz, "Chemical composition of the atmosphere of mars," *Advances in Space Research*, vol. 22, no. 3, p. 449, 1998.

[93] H. Broida and J. Pellam, "Phosphorescence of atoms and molecules of solid nitrogen at 4.2 k," *Physical Review*, vol. 95, no. 3, p. 845, 1954.

[94] M. Peyron and H. Broida, "Spectra emitted from solid nitrogen condensed at very low temperatures from a gas discharge," *The Journal of Chemical Physics*, vol. 30, no. 1, p. 139, 1959.

[95] H. Broida and M. Peyron, "Emission spectra of n_2, o_2, and no molecules trapped in solid matrices," *The Journal of Chemical Physics*, vol. 32, no. 4, p. 1068, 1960.

[96] D. Katakis and H. Taube, "Some photochemical reactions of o_3 in the gas phase," *The Journal of Chemical Physics*, vol. 36, no. 2, p. 416, 1962.

[97] N. G. Moll, D. R. Clutter, and W. E. Thompson, "Carbon trioxide: Its production, infrared spectrum, and structure studied in a matrix of solid co_2," *The Journal of Chemical Physics*, vol. 45, no. 12, p. 4469, 1966.

[98] J. M. Parnis, L. E. Hoover, T. D. Fridgen, and R. D. Lafleur, "Stabilization of the primary products of atomic oxygen (^{1}d) reactions with carbon monoxide, carbon dioxide, methane and other hydrocarbons in cryogenic matrixes," *The Journal of Physical Chemistry*, vol. 97, no. 41, p. 10 708, 1993.

[99] M. J. Perri, A. L. Van Wyngarden, J. J. Lin, Y. T. Lee, and K. A. Boering, "Energy dependence of oxygen isotope exchange and quenching in the o(^{1}d)+co$_2$ reaction: A crossed molecular beam study," *The Journal of Physical Chemistry A*, vol. 108, no. 39, p. 7995, 2004.

[100] C. J. Bennett, C. Jamieson, A. M. Mebel, and R. I. Kaiser, "Untangling the formation of the cyclic carbon trioxide isomer in low temperature carbon dioxide ices," *Physical Chemistry Chemical Physics*, vol. 6, no. 4, p. 735, 2004.

[101] A. Mebel, M. Hayashi, V. Kislov, and S. Lin, "Theoretical study of oxygen isotope exchange and quenching in the o(^{1}d)+co$_2$ reaction," *The Journal of Physical Chemistry A*, vol. 108, no. 39, p. 7983, 2004.

[102] Y. Liu, I. B. Bersuker, W. Zou, and J. E. Boggs, "Combined jahn- teller and pseudo-jahn- teller effect in the co$_3$ molecule: A seven-state six-mode problem," *Journal of chemical theory and computation*, vol. 5, no. 10, p. 2679, 2009.

[103] I. Stensgaard, E. Lægsgaard, and F. Besenbacher, "The reaction of carbon dioxide with an oxygen precovered ag (110) surface," *The Journal of chemical physics*, vol. 103, no. 22, p. 9825, 1995.

[104] W. J. Marinelli, W. J. Kessler, B. D. Green, and W. A. Blumberg, "Quenching of n$_2$($a^1\Pi_g$, v'= 0) by n$_2$, o$_2$, co, co$_2$, ch$_4$, h$_2$, and ar," *The Journal of Chemical Physics*, vol. 90, no. 4, p. 2167, 1989.

[105] A. Lofthus and P. H. Krupenie, "The spectrum of molecular nitrogen," *Journal of physical and chemical reference Data*, vol. 6, no. 1, p. 113, 1977.

[106] W. Kedzierski, J. Dech, and J. McConkey, "N(^{2}p) production in electron-n$_2$ collisions," *Journal of Physics B: Atomic, Molecular and Optical Physics*, vol. 50, no. 21, p. 215 201, 2017.

[107] C.-L. Lin and F. Kaufman, "Reactions of metastable nitrogen atoms," *The Journal of Chemical Physics*, vol. 55, no. 8, p. 3760, 1971.

[108] E. Zipf, P. Espy, and C. Boyle, "The excitation and collisional deactivation of metastable n(^{2}p) atoms in auroras," *Journal of Geophysical Research: Space Physics*, vol. 85, no. A2, p. 687, 1980.

[109] D. Baulch, C. Bowman, C. Cobos, R. Cox, T. Just, J. Kerr, M. Pilling, D. Stocker, J. Troe, W. Tsang, *et al.*, "Evaluated kinetic data for combustion modeling: Supplement ii," *Journal of physical and chemical reference data*, vol. 34, no. 3, p. 757, 2005.

[110] S. Chakrabarti, "Ground based spectroscopic studies of sunlit airglow and aurora," *Journal of atmospheric and solar-terrestrial physics*, vol. 60, no. 14, p. 1403, 1998.

[111] F. Bakalian, "Production of hot nitrogen atoms in the martian thermosphere," *Icarus*, vol. 183, no. 1, p. 69, 2006.

[112] H. Imanaka and M. A. Smith, "Formation of nitrogenated organic aerosols in the titan upper atmosphere," *Proceedings of the National Academy of Sciences*, vol. 107, no. 28, p. 12 423, 2010.

[113] J. Levaton and J. Amorim, "Metastable atomic species in the n_2 flowing afterglow," *Chemical Physics*, vol. 397, p. 9, 2012.

[114] J. W. Chamberlain, *Physics of the Aurora and Airglow: International Geophysics Series*. Elsevier, 2016, vol. 2.

[115] L. Vegard, *The auroral spectrum and the upper atmosphere*, 1924.

[116] G. Shrum, "On the luminescence of nitrogen, argon, and other condensed gases at very low temperatures," *Proc. R. Soc. Lond. A*, vol. 106, no. 736, p. 138, 1924.

[117] C. Herzfeld and H. Broida, "Interpretation of spectra of atoms and molecules in solid nitrogen condensed at 4.2 k," *Physical Review*, vol. 101, no. 2, p. 606, 1956.

[118] D. Burns, F. Simpson, and J. McConkey, "Absolute cross sections for electron excitation of the second positive bands of nitrogen," *Journal of Physics B: Atomic and Molecular Physics*, vol. 2, no. 1, p. 52, 1969.

[119] D. Shemansky, J. Ajello, and I. Kanik, "Electron excitation function of the n_2 second positive system," *The Astrophysical Journal*, vol. 452, p. 472, 1995.

[120] M. Hochlaf, H. Ndome, D. Hammoutène, and M. Vervloet, "Valence–rydberg electronic states of n_2: Spectroscopy and spin–orbit couplings," *Journal of Physics B: Atomic, Molecular and Optical Physics*, vol. 43, no. 24, p. 245 101, 2010.

[121] F. R. Gilmore, "Potential energy curves for n_2, no, o_2, and corresponding ions," 1966.

[122] J. M. Ajello, G. K. James, B. O. Franklin, and D. E. Shemansky, "Medium-resolution studies of extreme ultraviolet emission from n_2 by electron impact: Vibrational perturbations and cross sections of the $c_4'^1\Sigma_u^+$ and $b'^1\Sigma_u^+$ states," *Physical Review A*, vol. 40, no. 7, p. 3524, 1989.

[123] D. A. Little and J. Tennyson, "An ab initio study of singlet and triplet rydberg states of n_2," *Journal of Physics B: Atomic, Molecular and Optical Physics*, vol. 46, no. 14, p. 145 102, 2013.

[124] D. Spelsberg and W. Meyer, "Dipole-allowed excited states of n_2: Potential energy curves, vibrational analysis, and absorption intensities," *The Journal of Chemical Physics*, vol. 115, no. 14, p. 6438, 2001.

[125] S. Tilford and P. Wilkinson, "The emission spectrum of molecular nitrogen in the region 900–1130 å," *Journal of Molecular Spectroscopy*, vol. 12, no. 3, p. 231, 1964.

[126] H. H. Michels, "Electronic structure of excited states of selected atmospheric systems," *Advances in Chemical Physics: The Excited State in Chemical Physics, Part II*, p. 225, 1981.

[127] W. Ermler, A. McLean, and R. Mulliken, "Ab initio study of valence-state potential energy curves of nitrogen," *The Journal of Physical Chemistry*, vol. 86, no. 8, p. 1305, 1982.

[128] W. C. Ermler, J. P. Clark, and R. S. Mulliken, "A binitio calculations of potential energy curves and transition moments of $^1\Sigma_g^+$ and $^1\Sigma_u^+$ states of n_2," *The Journal of chemical physics*, vol. 86, no. 1, p. 370, 1987.

[129] E. F. van Dishoeck, *The chemistry of diffuse and dark interstellar clouds*. Oxford University Press: Oxford, 1998.

[130] M. Kawada, O. Sueoka, and M. Kimura, "Vibrational excitation of carbon oxysulfide molecules by positron and electron impacts," *The Journal of Chemical Physics*, vol. 112, no. 16, p. 7057, 2000.

[131] J. S. Muenter, "Electric dipole moment of carbonyl sulfide," *The Journal of Chemical Physics*, vol. 48, no. 10, p. 4544, 1968.

[132] R. Van Brunt and M. Mumma, "Fast metastable fragments produced by dissociative excitation of carbonyl sulfide," *The Journal of Chemical Physics*, vol. 63, no. 8, p. 3210, 1975.

[133] S. Barnett, N. Mason, and W. Newell, "Dissociative excitation of metastable fragments by electron impact on carbonyl sulphide, carbon dioxide and carbon monoxide," *Journal of Physics B: Atomic, Molecular and Optical Physics*, vol. 25, no. 6, p. 1307, 1992.

[134] A. Sugita, M. Mashino, M. Kawasaki, Y. Matsumi, R. Bersohn, G. Trott-Kriegeskorte, and K.-H. Gericke, "Effect of molecular bending on the photodissociation of ocs," *The Journal of Chemical Physics*, vol. 112, no. 16, p. 7095, 2000.

[135] M. H. Kim, W. Li, S. K. Lee, and A. G. Suits, "Probing of the hot-band excitations in the photodissociation of ocs at 288 nm by dc slice imaging," *Canadian journal of chemistry*, vol. 82, no. 6, p. 880, 2004.

[136] S. K. Lee, R. Silva, S. Thamanna, O. S. Vasyutinskii, and A. G. Suits, "$S(^1d_2)$ atomic orbital polarization in the photodissociation of ocs at 193 nm: Construction of the complete density matrix," *The Journal of chemical physics*, vol. 125, no. 14, p. 144 318, 2006.

[137] M. Brouard, A. Green, F. Quadrini, and C. Vallance, "Photodissociation dynamics of ocs at 248 nm: The s(^{1}d$_2$) atomic angular momentum polarization," *The Journal of chemical physics*, vol. 127, no. 8, p. 084 304, 2007.

[138] M. L. Lipciuc, T. P. Rakitzis, W. L. Meerts, G. C. Groenenboom, and M. H. Janssen, "Towards the complete experiment: Measurement of s(^{1}d$_2$) polarization in correlation with single rotational states of co(j) from the photodissociation of oriented ocs(ν_2=1—jlm= 111)," *Physical Chemistry Chemical Physics*, vol. 13, no. 18, p. 8549, 2011.

[139] C. Weeraratna, C. Amarasinghe, R. Fernando, V. Tiwari, and A. G. Suits, "Convenient (1+1) probe of s(^{1}d$_2$) and application to photodissociation of carbonyl sulfide at 216.9 nm," *Chemical Physics Letters*, vol. 657, p. 162, 2016.

[140] W. Wei, C. J. Wallace, G. C. McBane, and S. W. North, "Photodissociation dynamics of ocs near 214 nm using ion imaging," *The Journal of chemical physics*, vol. 145, no. 2, p. 024 310, 2016.

[141] X. Bai, H. Liang, Z. Zhou, Z. Hua, B. Jiang, D. Zhao, and Y. Chen, "Photodissociation dynamics of ocs at 210 nm: The role of $c(2^3a'')$ state," *The Journal of Chemical Physics*, vol. 147, no. 1, p. 013 930, 2017.

[142] M. Brouard, F. Quadrini, and C. Vallance, "The photodissociation dynamics of ocs at 248 nm: The s(^{3}p$_j$) atomic angular momentum polarization," *The Journal of chemical physics*, vol. 127, no. 8, p. 084 305, 2007.

[143] J. Kłos, G. Chałasiński, R. V. Krems, A. Buchachenko, V. Aquilanti, F. Pirani, and D. Cappelletti, "Ab initio potentials for the s(^{3}p$_j$)–rare gas dimers: Implementation for elastic and inelastic collisions and comparison with scattering potentials," *The Journal of chemical physics*, vol. 116, no. 21, p. 9269, 2002.

[144] V. Aquilanti, D. Ascenzi, E. Braca, D. Cappelletti, and F. Pirani, "Production, characterization and scattering of a sulfur atom beam: Interatomic potentials for the rare-gas sulfides, rs (r= ne, ar, kr, xe)," *Physical Chemistry Chemical Physics*, vol. 2, no. 18, p. 4081, 2000.

[145] M. Yamanishi, K. Hirao, and K. Yamashita, "Theoretical study of the low-lying electronic states of xeo and xes," *The Journal of chemical physics*, vol. 108, no. 4, p. 1514, 1998.

[146] M. Lara, C. Berteloite, M. Paniagua, F. Dayou, S. D. Le Picard, and J.-M. Launay, "Experimental and theoretical study of the collisional quenching of s(^{1}d) by ar," *Physical Chemistry Chemical Physics*, vol. 19, no. 42, p. 28 555, 2017.

[147] A. Kramida, Yu. Ralchenko, J. Reader, and and NIST ASD Team, NIST Atomic Spectra Database (ver. 5.2), [Online]. Available: `http://physics.nist.gov/asd` [2014, December 16]. National Institute of Standards and Technology, Gaithersburg, MD. 2014.

[148] S. Cova, M. Ghioni, A. Lacaita, C. Samori, and F. Zappa, "Avalanche photodiodes and quenching circuits for single-photon detection," *Applied optics*, vol. 35, no. 12, p. 1956, 1996.

[149] Z. Delalic, P. Erman, and E. Kallne, "Lifetimes of transitions in the visible range in neutral sulphur," *Physica Scripta*, vol. 42, no. 5, p. 540, 1990.

[150] N. Watanabe and A. Kouchi, "Efficient formation of formaldehyde and methanol by the addition of hydrogen atoms to co in h_2o-co ice at 10 k," *The Astrophysical Journal Letters*, vol. 571, no. 2, p. L173, 2002.

[151] F. F. van der Tak, E. F. van Dishoeck, and P. Caselli, "Abundance profiles of ch_3oh and h_3co toward massive young stars as evolutionary tracers," *arXiv preprint astro-ph/0008010*, 2000.

[152] M. A. Requena-Torres, J. Martın-Pintado, A. Rodrıguez-Franco, S. Martın, N. Rodrıguez-Fernández, and P. De Vicente, "Organic molecules in the galactic center-hot core chemistry without hot cores," *Astronomy & Astrophysics*, vol. 455, no. 3, p. 971, 2006.

[153] M. Mumma, N. D. Russo, M. DiSanti, K. Magee-Sauer, R. Novak, S. Brittain, T. Rettig, I. McLean, D. Reuter, and L.-H. Xu, "Organic composition of c/1999 s4 (linear): A comet formed near jupiter?" *Science*, vol. 292, no. 5520, p. 1334, 2001.

[154] B. Boudaffa, P. Cloutier, D. Hunting, M. A. Huels, and L. Sanche, "Resonant formation of dna strand breaks by low-energy (3 to 20 ev) electrons," *Science*, vol. 287, no. 5458, p. 1658, 2000.

[155] M. Khakoo, J. Blumer, K. Keane, C. Campbell, H. Silva, M. Lopes, C. Winstead, V. McKoy, R. Da Costa, L. Ferreira, *et al.*, "Low-energy electron scattering from methanol and ethanol," *Physical Review A*, vol. 77, no. 4, p. 042 705, 2008.

[156] D. Bouchiha, J. Gorfinkiel, L. Caron, and L. Sanche, "Low-energy electron collisions with methanol," *Journal of Physics B: Atomic, Molecular and Optical Physics*, vol. 40, no. 6, p. 1259, 2007.

[157] S. Srivastava, E. Krishnakumar, A. Fucaloro, and T. Note, "Cross sections for the production of cations by electron impact on methanol," *Journal of Geophysical Research: Planets*, vol. 101, no. E11, p. 26 155, 1996.

[158] R. Rejoub, C. Morton, B. Lindsay, and R. Stebbings, "Electron-impact ionization of the simple alcohols," *The Journal of chemical physics*, vol. 118, no. 4, p. 1756, 2003.

[159] A. Zavilopulo, F. Chipev, and L. Kokhtych, "Dissociative ionization of ethanol, methanol and butanol molecules," *Nuclear Instruments and Methods in Physics Research Section B: Beam Interactions with Materials and Atoms*, vol. 233, no. 1-4, p. 302, 2005.

[160] K. M. Douglas and S. D. Price, "Studies of the fragmentation of the monocation and dication of methanol," *The Journal of chemical physics*, vol. 131, no. 22, p. 224 305, 2009.

[161] D. E. Donohue, J. A. Schiavone, and R. S. Freund, "Molecular dissociation by electron impact: Optical emission from fragments of methane, ethylene, and methanol," *The Journal of Chemical Physics*, vol. 67, no. 2, p. 769, 1977.

[162] J. Berkowitz, "Photoionization of ch_3oh, cd_3oh, and ch_3od: Dissociative ionization mechanisms and ionic structures," *The Journal of Chemical Physics*, vol. 69, no. 7, p. 3044, 1978.

[163] G. R. Burton, W. F. Chan, G. Cooper, and C. Biron, "Absolute oscillator strengths for photoabsorption (6–360 ev) and ionic photofragmentation (10–80 ev) of methanol," *Chemical physics*, vol. 167, no. 3, p. 349, 1992.

[164] S. Pilling, R. Neves, A. Santos, and H. Boechat-Roberty, "Photodissociation of organic molecules in star-forming regions-iii. methanol," *Astronomy & Astrophysics*, vol. 464, no. 1, p. 393, 2007.

[165] T. Sato, A. Iwasaki, T. Okino, K. Yamanouchi, A. Yagishita, H. Yazawa, F. Kannari, M. Aoyama, K. Yamakawa, K. Midorikawa, H. Nakano, M. Yabashi, M. Nagasono, A. Higashiya, T. Togashi, and T. Ishikawa, "Multi-photon ionization of atoms and molecules by intense xuv-fel light application to methanol and ethanol molecules," *Reza Kenkyu*, vol. 37, no. 12, p. 905, 2009.

[166] R. Buenker, G. Olbrich, H. Schuchmann, B. Schuermann, and C. Von Sonntag, "Photolysis of methanol at 185 nm. quantum-mechanical calculations and product study," *Journal of the American Chemical Society*, vol. 106, no. 16, p. 4362, 1984.

[167] S. Satyapal, J. Park, R. Bersohn, and B. Katz, "Dissociation of methanol and ethanol activated by a chemical reaction or by light," *The Journal of Chemical Physics*, vol. 91, no. 11, p. 6873, 1989.

[168] Y. Wen, J. Segall, M. Dulligan, and C. Wittig, "Photodissociation of methanol at 193.3 nm: Translational energy release spectra," *The Journal of chemical physics*, vol. 101, no. 7, p. 5665, 1994.

[169] E. Sominska and A. Gedanken, "The absorption spectrum of a supersonically expanded beam of methanol in the vacuum ultraviolet region," *Journal of Molecular Spectroscopy*, vol. 175, no. 2, p. 234, 1996.

[170] S. Harich, J. Lin, Y. Lee, and X. Yang, "Photodissociation dynamics of methanol at 157 nm," *The Journal of Physical Chemistry A*, vol. 103, no. 49, p. 10 324, 1999.

[171] B.-M. Cheng, M. Bahou, W.-C. Chen, C.-h. Yui, Y.-P. Lee, and L. Lee, "Experimental and theoretical studies on vacuum ultraviolet absorption cross sections and photodissociation of ch_3oh, ch_3od, cd_3oh, and cd_3od," *The Journal of chemical physics*, vol. 117, no. 4, p. 1633, 2002.

[172] S.-H. Lee, H.-I. Lee, and Y. T. Lee, "Distributions of angular anisotropy and kinetic energy of products from the photodissociation of methanol at 157 nm," *The Journal of chemical physics*, vol. 121, no. 22, p. 11 053, 2004.

[173] Z. Chen, A. T. Eppink, B. Jiang, G. C. Groenenboom, X. Yang, and D. H. Parker, "Product pair correlation in ch_3oh photodissociation at 157 nm: The oh+ch_3 channel," *Physical Chemistry Chemical Physics*, vol. 13, no. 6, p. 2350, 2011.

[174] M. Lucas, Y. Liu, R. Bryant, J. Minor, and J. Zhang, "Vacuum ultraviolet photodissociation dynamics of methanol at 121.6 nm," *Chemical Physics Letters*, vol. 619, p. 18, 2015.

[175] J. Ajello, D. Shemansky, and G. James, "Cross sections for production of h (2p, 2s, 1s) by electron collisional dissociation of h_2," *The Astrophysical Journal*, vol. 371, p. 422, 1991.

[176] C. Joram, "Transmission curves of plexiglass (pmma) and optical grease," Tech. Rep., 2009.

[177] H. P. K. K. (2007). Photomultiplier tubes: Basics and applications, [Online]. Available: `https://www.hamamatsu.com/resources/pdf/etd/PMT_handbook_v3aE.pdf` (visited on 01/21/2019).

[178] M. Kayanuma, M. Shoji, K. Furuya, Y. Aikawa, M. Umemura, and Y. Shigeta, "Theoretical study of the photodissociation reaction of methanol," *Chemical Physics Letters*, vol. 714, p. 137, 2019.

[179] E. F. van Dishoeck and A. Dalgarno, "Photodissociation processes in the oh molecule," *The Journal of Chemical Physics*, vol. 79, no. 2, p. 873, 1983.

[180] A. Varandas and A. Voronin, "Calculation of the asymptotic interaction and modelling of the potential energy curves of oh and oh^+," *Chemical physics*, vol. 194, no. 1, p. 91, 1995.

[181] P. J. Mohr, D. B. Newell, and B. N. Taylor, "Codata recommended values of the fundamental physical constants: 2014," *Journal of Physical and Chemical Reference Data*, vol. 45, no. 4, p. 043 102, 2016.

Vita Auctoris

NAME:	Jeffery Michael Dech
PLACE OF BIRTH:	Windsor, ON
YEAR OF BIRTH:	1989
EDUCATION:	Riverside Secondary School, Windsor, ON, 2007
	University of Windsor, B.Sc. Hon., Windsor, ON, 2012
	University of Windsor, M.Sc., Windsor, ON, 2015
	University of Windsor, Ph.D., Windsor, ON, 2019